

Preparation of a Precision Spectroscopy Measurement of Metastable Hydrogen and Deuterium with a Modified Lamb-shift Polarimeter

Diploma Thesis in Experimental Physics
at the Faculty of Mathematics and Natural Sciences
of the University of Cologne

—
Realized at the Institute of Nuclear Physics II
at Forschungszentrum Jülich

**Submitted by
Marc Peter Westig**

Jülich 2008

Preparation of a Precision Spectroscopy Measurement of Metastable Hydrogen and Deuterium with a Modified Lamb-shift Polarimeter

Diploma Thesis in Experimental Physics
at the Faculty of Mathematics and Natural Sciences
of the University of Cologne

—
Realized at the Institute of Nuclear Physics II
at Forschungszentrum Jülich

**Submitted by
Marc Peter Westig**

Jülich 2008

First Referee: Prof. Dr. H. Ströher (University of Cologne & Forschungszentrum Jülich)
Second Referee: Prof. Dr. J. Stutzki (University of Cologne)

Vorbereitung einer Präzisionsmessung zur Spektroskopie an metastabilem Wasserstoff und Deuterium mit einem modifizierten Lambshift-Polarimeter

Diplomarbeit in Experimentalphysik
an der mathematisch-naturwissenschaftlichen Fakultät
der Universität zu Köln

—
Durchgeführt im Institut für Kernphysik II
am Forschungszentrum Jülich

**vorgelegt von
Marc Peter Westig**

Jülich 2008

Erster Gutachter: Prof. Dr. H. Ströher (Universität zu Köln & Forschungszentrum Jülich)
Zweiter Gutachter: Prof. Dr. J. Stutzki (Universität zu Köln)

„Zwei Dinge sind zu unserer Arbeit nötig: Unermüdliche Ausdauer und die Bereitschaft, etwas, in das man viel Zeit und Arbeit gesteckt hat, wieder wegzuwerfen.“

Albert Einstein

Abstract

In this diploma thesis, the setup of a Lamb-shift polarimeter is presented which was supplemented by a second spinfilter and a spectroscopy chamber. With this modified Lamb-shift polarimeter, it is possible to determine the $2S_{1/2}$ and $2P_{1/2}$ hyperfine structures (hfs), respectively, and the $2S_{1/2} - 2P_{1/2}$ Lamb shift (classical Lamb shift) of the hydrogen (^1H) and deuterium (^2H) atom. Furthermore, a coil system allows to observe atomic transitions in a magnetic field and, therefore, to determine the Breit-Rabi diagrams of the first excited state. A metastable atomic beam with a definite energy passes a spinfilter, where atoms in the single Zeeman states α_1 and α_2 (^1H) or α_1 , α_2 and α_3 (^2H), respectively, of the hyperfine structure of the $2S_{1/2}$ state are transmitted. In a spectroscopy chamber, atoms in these states undergo a transition into other quantum states. Due to the quantum mechanical selection rules, definite transitions can be observed. In the framework of this thesis the experiment was assembled and commissioned. In the limited time-frame, first measurements with a metastable atomic hydrogen beam were also performed. Electric dipole transitions which occurred inside a TEM waveguide were observed and first spectroscopic data was acquired and analyzed. As a result, which proves the operation principle, preliminary values of the $2P_{1/2}$ hfs and of the classical Lamb shift in ^1H were obtained. In addition it was possible to observe electric dipole transitions in an external magnetic field and to obtain first data of the Breit-Rabi diagrams of the first excited state in ^1H . In the course of the measurements, it became apparent which parts of the modified Lamb-shift polarimeter have to be improved or renewed to be able to perform a high-precision experiment. The first results which have been obtained show the huge potential of this experiment, also as compared to other methods.

Zusammenfassung

In der vorliegenden Diplomarbeit wird der erstmalige Aufbau eines um ein SpinfILTER und eine Spektroskopiekammer erweiterten Lambshift-Polarimeters vorgestellt. Mit dem modifizierten Lambshift-Polarimeter ist es möglich die $2S_{1/2}$ bzw. $2P_{1/2}$ Hyperfeinstrukturaufspaltung (HFS) und die $2S_{1/2} - 2P_{1/2}$ Lambshift (klassische Lambshift) des Wasserstoff- (^1H) und Deuteriumatoms (^2H) zu bestimmen. Weiterhin bietet eine Spulenkonfiguration die Möglichkeit, atomare Übergänge in einem Magnetfeld zu untersuchen und somit die Breit-Rabi Diagramme des ersten angeregten Zustands zu bestimmen. Ein metastabiler Atomstrahl mit einer festen Energie passiert ein sogenanntes SpinfILTER. Hierbei werden die einzelnen Zeeman-Zustände α_1 oder α_2 bei ^1H bzw. α_1 , α_2 oder α_3 bei ^2H der Hyperfeinstruktur des $2S_{1/2}$ Zustands selektiert. In einer Spektroskopiekammer wird von diesen Zuständen aus ein Übergang in einen anderen Quantenzustand induziert. Aufgrund der Auswahlregeln der Quantenmechanik sind nur einige festgelegte Übergänge möglich. Im Rahmen dieser Arbeit konnte das Experiment aufgebaut und in Betrieb genommen werden. Erste Messungen mit einem metastabilen Wasserstoffatomstrahl waren zeitlich ebenfalls noch möglich. Elektrische Dipolübergänge, welche in einer TEM Hochfrequenzzelle induziert wurden, konnten beobachtet und erste spektroskopische Daten gesammelt und ausgewertet werden. Daraus ergaben sich vorläufige Werte der $2P_{1/2}$ HFS und der klassischen Lambshift in ^1H . Zusätzlich war es möglich, elektrische Dipolübergänge in einem externen magnetischen Feld zu beobachten und erste Daten der Breit-Rabi Diagramme des ersten angeregten Zustands in ^1H zu erhalten. Im Verlauf der vorliegenden Diplomarbeit ist deutlich geworden, welche Teile des modifizierten Lambshift-Polarimeters verbessert oder erneuert werden müssen, um damit schließlich ein Präzisionsexperiment durchführen zu können. Die ersten Resultate, die im Rahmen dieser Diplomarbeit erhalten wurden, verdeutlichen aber bereits das große Potential dieses Experiments.

Contents

1	Introduction	1
2	Theory	11
2.1	Quantum Theory of the Hydrogen and Deuterium Atom	11
2.1.1	Non-Relativistic Quantum Theory	11
2.1.2	Relativistic Quantum Theory - Electron Spin, Spin-Orbit Coupling and Fine Structure	16
2.1.3	Quantum Electrodynamical Corrections to the Energy Levels . .	21
2.1.4	Hyperfine Splitting - Explicit Formula versus D_{21} Theory	28
2.2	Precise Breit-Rabi Diagrams	36
2.2.1	The Breit-Rabi Formula for the Hydrogen and Deuterium Atom	39
2.2.2	Breit-Rabi Diagram of the Hydrogen Atom	46
2.2.3	Breit-Rabi Diagram of the Deuterium Atom	47
2.3	Interaction with a Time-Dependent Electromagnetic Field	48
2.4	Atoms in a Static Electric Field - The Stark Effect	53
2.5	Production of Polarized Metastable Atoms	55
3	Experimental Setup	59
3.1	Principle of the Measurement	59
3.1.1	Electric Dipole Transitions	59
3.1.2	Magnetic Dipole Transitions	60
3.2	The modified Lamb-shift Polarimeter	60
3.2.1	Overview	60
3.2.2	Pumping System	65

3.2.3	The Ionizer	65
3.2.4	The Deflector Chamber	67
3.2.5	The Wien Filter	67
3.2.6	The Cesium Cell	68
3.2.7	The Spinfilter	69
3.2.8	The Spectroscopy Chamber	71
3.2.9	The Quench Chamber	90
3.3	Operation Modes of the modified Lamb-shift Polarimeter	91
3.3.1	Measurement of Electric Dipole Transitions	91
3.3.2	Measurement of Magnetic Dipole Transitions	96
4	First Measurements	101
4.1	Uncertainties of Electric Dipole Transition Frequencies	101
4.1.1	Doppler Shift	101
4.1.2	Magnetic Field Inhomogeneities and Residual Magnetic Fields	103
4.1.3	Power Fluctuations	103
4.1.4	Electric Fields	104
4.1.5	Motional Stark Effect	104
4.1.6	Resume	105
4.2	Measurement of the Classical Lamb shift	105
4.2.1	Measurements without Shielding	106
4.2.2	Measurements with Shielding	108
4.2.3	Results	111
4.2.4	First Determination of the $2P_{1/2}$ HFS	113
4.2.5	Determination of the Classical Lamb shift	113
4.3	Electric Dipole Transitions in an External Magnetic Field	115
5	Conclusion & Outlook	119
A	Breit-Rabi Formula Coefficients	123

CHAPTER 1

INTRODUCTION

The interpretation of the atomic spectrum of hydrogen (^1H), the most fundamental atom, has advanced physics in an incomparable manner and inspired physicists to further and new considerations. As the date of birth of atomic spectroscopy, the years of 1885 and 1890 are surely the most obvious. For the first time Balmer and Rydberg, respectively, tried to explain the atomic spectrum of hydrogen in these years. Further milestones to a better understanding of atomic physics, especially of the hydrogen atom, are the year 1913, in which a new atomic model was developed by the Danish physicist Niels Bohr and the year 1926, when Erwin Schrödinger found the famous equation named after him. Further on the year 1928 is important when Paul Dirac developed a relativistic theory including the electron spin, could explain the fine structure and even made the hyperfine structure (hyperfine splitting, abbr. hfs) understandable. Finally the year 1949 should be mentioned in which quantum electrodynamics (abbr. QED), a special quantum field theory (abbr. QFT) which describes the interaction of light¹ with matter, was improved in a very important way by the three excellent physicists Feynman [Fey49a, Fey49b], Schwinger and Tomonaga, allowing for example to calculate the Lamb shift. The energy shift between the states $2S_{1/2}$ and $2P_{1/2}$ was experimentally found by Lamb and Retherford [Lam47] in the year 1947 and bears since this moment the name of its discoverers. Because this was the first measurement of the Lamb shift, it is often denoted as the classical Lamb shift. With this special name it is well differentiable from the Lamb shifts of other atomic states. For sure it is not accidental that the microwave technique Lamb and Retherford used for their experiment, was a well-known technique after the Second World War. Microwaves are also used for radar and radio. The result of Lamb and Retherford caused a sensation in the physical community, because the Dirac theory had to be renewed, which was well accepted until this

¹The term “light” has to be understood in a very general way as will be seen in this thesis. For example in chapter 2 the electron is described as a particle interacting with the Coulomb field of the nucleus. The Coulomb field, with the nucleus as its source, can be regarded as a “light field” which interacts with matter, i.e. with the electron. This point of view is justifiable, because light, in the proper meaning of the word, as well as the Coulomb field of the nucleus, consist of the same elementary building blocks, of the photons.

moment. Dirac's theory predicts energy degenerate states $2S_{1/2}$ and $2P_{1/2}$, which is not correct according to the ground-breaking measurement of Lamb and Retherford. However, in the framework of QED the atomic spectrum of hydrogen was well predictable and QED arose to the most precise theory in physics we know to the present date. Since then, this theory was further developed. Even approaches to calculate energy states in bound two-particle systems interacting by a quantized field were elaborated [Gel51]. Physical systems of this type are for example the hydrogen and the deuterium atom (^2H). The QFT which is used to make precise calculations in these atoms and in general in bound systems, like e.g. muonic hydrogen, is called bound-state quantum electrodynamics (abbr. BSQED). In the framework of BSQED bound-particle systems, where the particles interact only electromagnetically with each other, are describable. Moreover, the bound-state theory in QED is closely linked with the bound-state theory in quantum chromodynamics (abbr. QCD), the modern theory of the strong interaction. The advantage of QED calculations in comparison with calculations in QCD is the non-self-interacting character of the photons in contrast to the gluons which are self-interacting particles. So, BSQED can be considered as a laboratory to explore and to understand the properties of bound-state physics free from complications like the non-perturbative character of QCD. BSQED is an extension of QED because in the proper meaning in the framework of QED only unbound systems which interact electromagnetically with each other are calculable. Anyway, the term "quantum electrodynamical calculations", both in unbound and bound systems, is often embraced by the term "QED calculations". The term "BSQED" can then be used to point out additionally the bound-state character of the calculation. As the perhaps most famous example of QED tests, the $(g - 2)$ -experiment has to be mentioned. This experiment is exclusively predictable with QED and with it the discrepancy of the free electron g factor from the Dirac value $g = 2$ can be determined. Also by this example - for the first time a deviation from $g = 2$ was measured in the year 1947, in the same year like the experimental discovery of the classical Lamb shift - it becomes clear how intense the scientific work in this physical field was and still is. The latest published measurement of $(g - 2)$ is the famous experiment of Van Dyck [Van87] with a precision of $4 \cdot 10^{-9}$ for the free electron, the most precise value ever measured for this quantity until now. At the same moment it is also a possibility to test the \mathcal{CPT} theorem², because Van Dyck measured also the g factor of the free positron, the antiparticle of the electron, and discovered that both values, the g factor of the electron and the positron, are the same

²The \mathcal{CPT} theorem, a short form for the term "charge conjugation, parity and time reversal theorem", is a fundamental symmetry principle in physics and states that for example the g factor of the free electron and the free positron should be the same. The electron and the positron are ideal probes to test this theorem, because they have identical, but opposite charges and both can be looked at as their antiparticle moving backwards in time.

on a scale of 10^{-12} . Until the present day, equally QED and BSQED are an up-to-date scientific field in physics with highest reputation. Especially BSQED is continuously challenged by high-precision spectroscopy experiments of the hydrogen and deuterium atom. Both disciplines together, i.e. the theoretical part with the BSQED and the experimental part with the spectroscopy experiments, can test physics on a very high and precise level, i.e. latest BSQED results can be tested and checked for their validity. In addition to the Lamb shift, BSQED provides calculations of the hyperfine splitting, but also of the g factors of bound electrons, one of the most precise quantities presently known in physics. Although in general a very precise theory, BSQED is limited in its precision by a crucial quantity which is used in the theory as a free parameter, i.e. cannot be calculated from theory itself. This quantity is the proton charge radius [Kar99] and the deuteron charge radius [Pac96], respectively, the least precise value which is used in quantum electrodynamical calculations. Experimental tests of BSQED of the hydrogen or the deuterium atom include automatically the influence of the proton and deuteron charge radius, respectively. In spectroscopy experiments the influence of the charge radii can be observed in the shift of the energy levels in the hydrogen or the deuterium atom. On one hand precision measurements in these atoms are, therefore, a good possibility to determine a new value of the charge radii in both atoms and in general to learn something about the structure of the proton and the deuteron. On the other hand precision measurements can also provide a test of, in first order, pure BSQED effects, i.e. effects with vanishing influence of the nucleus. Experiments of this kind are the test of the D_{21} theory³ in hydrogen and deuterium, respectively, where the $2S_{1/2}$ hyperfine splitting is measured precisely and after this multiplied by a factor of eight to finally subtract this result from the well-known value of the $1S_{1/2}$ hyperfine splitting [Win72, Ram93]. Therefore, leading order nuclear structure effects cancel out [Kar02b, Kar02a, Kar03]. Simultaneously to the experiment, the quantity D_{21} is well calculable. Due to the influence of the proton and the deuteron, precise absolute calculations of the hyperfine splitting are difficult, but the D_{21} theory provides an established possibility to calculate a difference quantity. However, the comparison of the experimental with the theoretical value of D_{21} shows a discrepancy, which is due to higher order contributions of the nucleus which do not cancel in D_{21} . It is not the main aim of the D_{21} theory to include higher order nuclear contributions to the theory, but to compare theory and experiment on the pure BSQED side, to learn something about the nuclear structure which shows up as a difference between experimental and theoretical values.

A precise measurement of the $2S_{1/2}$ hyperfine splitting in ^1H was performed in the year 2000 by Rothery and Hessels [Rot00]. They used radio-frequency (abbr. rf)

³ $D_{21} = 8f_{hfs}(2S_{1/2}) - 1f_{hfs}(1S_{1/2})$, where f_{hfs} is the hyperfine separation in terms of a frequency.

methods and got the most precise value of the $2S_{1/2}$ hyperfine splitting until 2004 when Kolachevsky et al. [Kol04b] measured the same quantity with an optical method. The result of the experiment of Kolachevsky et al. is $f_{hf_s}^{1H}(2S_{1/2}) = 177\,556\,860(16)$ Hz and is up to now the most accurate value of this quantity. In total the $2S_{1/2}$ hyperfine splitting was measured only three times in the last fifty years. The first measurement was realized by Heberle et al. [Heb56]. The current theoretical accuracy of D_{21} is one order of magnitude higher compared to the experimental accuracy. In ^1H the measurement of the $2S_{1/2}$ hyperfine splitting from Heberle et al. in combination with the value of the $1S_{1/2}$ hyperfine splitting of Ramsey allows to calculate an experimental value of $D_{21}^{exp,1H} = 49.13(40)$ kHz. On the other hand from the measurement of Rothery and Hessels a value of $D_{21}^{exp,1H} = 48.53(23)$ kHz can be obtained. The latest result of Kolachevsky et al. leads to a value of $D_{21}^{exp,1H} = 49.13(12)$ kHz. Compared with the experimental values, the theoretical value of $D_{21}^{theo,1H} = 48.953(3)$ kHz [Kar02b, Kar02a, Kar03] was not yet exceeded in accuracy by an experimentalist.

In the case of ^2H , the measurement of the $2S_{1/2}$ hyperfine splitting of Reich et al. [Rei56] in combination with the $1S_{1/2}$ hyperfine splitting [Win72] results in an experimental value of $D_{21}^{exp,2H} = 11.16(16)$ kHz, in comparison to the more accurate theoretical value of $D_{21}^{theo,2H} = 11.3125(5)$ kHz [Kar02b, Kar02a, Kar03]. The most recent measurement of [Kol04a] results in $D_{21}^{exp,2H} = 11.280(56)$ kHz which is in good agreement with the theoretical prediction.

Something similar to test experiment and theory does not exist for the $2P_{1/2}$ hyperfine splitting. Nevertheless, for theory the measurement of this energy splitting is of importance. This can be explained as follows. Values which have been measured with a comparable accuracy like for the $2S_{1/2}$ hyperfine splitting, are not known for the $2P_{1/2}$ hyperfine splitting. It could be stated that up to now no serious efforts to measure the $2P_{1/2}$ hyperfine splitting have been undertaken. Calculations of the $2P_{1/2}$ hyperfine splitting are still rather imprecise and uncompleted which makes the specification of a calculation error impossible. For example the one-electron radiative correction $x_{rad}^{(2P_{1/2})}$, which contributes to the formula of the hyperfine splitting, is not completely calculated up to now. The corrections which have to be considered due to the electric and magnetic properties of the extended nucleus, called Breit-Rosenthal-Crawford-Schawlow and Bohr-Weisskopf corrections and denoted by the symbols $\delta^{(2P_{1/2})}$ and $\epsilon^{(2P_{1/2})}$, are neglected in today's calculations of the $2P_{1/2}$ hyperfine splitting, because of their small influence. Compared to the same effects in the $2S_{1/2}$ state, these effects are up to four orders of magnitude smaller in the $2P_{1/2}$ state, but nevertheless, to determine a theoretical error of a precise calculation of the $2P_{1/2}$ hyperfine splitting, they have to be considered. It really seems that there is no accurate result available for this fundamental quantity in the hydrogen and deuterium atom, neither on the part of the

experimentalists nor on the part of the theoreticians. In the $2P_{1/2}$ state with orbital angular momentum quantum number $l = 1$, the electron has a vanishing probability to be at the position of the nucleus, so a theoretical determination of the $2P_{1/2}$ hyperfine splitting includes less influence of the nucleus than in the $2S_{1/2}$ state. Interest on the measurement of the $2P_{1/2}$ hyperfine splitting exist on the part of the theoreticians.

Similar to the hyperfine structure of an atom, nuclear structure effects⁴ have also an effect on the Lamb shift of an atom. Again, the lack of precise data of the proton and deuteron charge radii, respectively, limits the accuracy of state-of-the-art calculations of the Lamb shift in general, thus of the classical Lamb shift, too. The influence of the charge radii on the classical Lamb shift in hydrogen and deuterium can be expressed with following formulas⁵ [Mil04]

$$\Delta E_{FNS}^{(nS_{1/2})} = \frac{2}{3n^3\hbar^2}(Z\alpha)^4 m_e^3 c^4 \langle r^2 \rangle \quad ,$$

$$\Delta E_{FNS}^{(nP_{1/2})} = \frac{n^2 - 1}{6n^5\hbar^2}(Z\alpha)^6 m_e^3 c^4 \langle r^2 \rangle \quad .$$

A comparison between experimental data and the theoretical prediction of the Lamb shift, therefore, allows to make an estimate of the charge radii in both atoms. To get a precise formula of the classical Lamb shift with the up-to-date coefficients and the charge radius as free parameter, a contact to Ulrich Jentschura from the Max-Planck-Institute for Nuclear Physics in Heidelberg exists. Due to the complexity of such calculations, a finishing date of the calculations is not specified at the moment. When it will be finished, with the help of this formula it is possible to calculate a value of the charge radius of the hydrogen and deuterium atom from our measurement of the classical Lamb shift.

The latest⁶ and today's most precise values of the classical Lamb shift are from indirect optical measurements with the method of Doppler-free 2-photon laser spectroscopy [Bou96, Sch99], but also direct measurements with rf techniques [Lun81, Hag94] still belong to the current dataset. Indirect optical measurements are the only method to determine the $1S_{1/2}$ Lamb shift. An innovative method of this kind of measurement is based on a comparison of the $1S_{1/2} - 2S_{1/2}$ resonance with resonances of higher energy levels, e.g. with the $2S_{1/2} - 4P_{1/2}$ resonance. In accordance with the Dirac theory, the

⁴Effects due to the influence of the nucleus on the hyperfine structure or on the Lamb shift are often called in the literature "finite nuclear size effects" (abbr. FNS effects).

⁵Here $r_p = \sqrt{\langle r^2 \rangle}$ is the charge radius. The quantity $\langle r^2 \rangle$ is the root-mean-square radius and is defined as the squared charge radius, multiplied by the charge distribution of the nucleus, integrated over the whole \mathbb{R}^3 and finally divided by the integral over the whole \mathbb{R}^3 of the charge distribution of the nucleus.

⁶The values of the first measurements of Lamb and Retherford are not cited in this thesis, because since this point in time the experimental techniques to measure the Lamb shift of different levels and even of the classical Lamb shift were continuously improved, so that only the most recent values are summarized.

frequency interval of the $2S_{1/2} - 4P_{1/2}$ resonance is four times smaller than the interval of the $1S_{1/2} - 2S_{1/2}$ resonance⁷. The Dirac theory does not include the Lamb shift, i.e. no QED (BSQED) effects in general, so a comparison between the two frequency intervals provides a value for the $1S_{1/2}$ Lamb shift, because of the negligible $4P_{1/2}$ Lamb shift. The quantity measured in such experiments is a frequency difference Δf . In the special case of a comparison of the $1S_{1/2} - 2S_{1/2}$ with the $2S_{1/2} - 4P_{1/2}$ resonance, it is

$$\Delta f = -\Delta E_L(1S_{1/2}) + 5\Delta E_L(2S_{1/2}) \quad ,$$

where $\Delta E_L(nS_{1/2})$ is the Lamb shift of the level with principal quantum number n and orbital angular momentum quantum number $l = 0$. If the Lamb shift now is calculated with methods of BSQED, then, in the case of ^1H , by using the often cited charge radius of the proton with the value $r_p = 0.862(12)$ fm [Sim80], the theory can be tested by comparing it with the measurement. On the other hand a new value of the proton charge radius can be determined as far as the precision of the measurement allows to do this. The same applies to the deuterium atom. Due to the uncertainty of the proton charge radius, the resulting error in the calculated $1S_{1/2}$ Lamb shift in ^1H is about 32 kHz and in the calculated classical Lamb shift about 4 kHz [Pac01]. The measurements of the $1S_{1/2}$ Lamb shift of Bourzeix et al. [Bou96] and Schwob et al. [Sch99] illustrate the high requirement for an experiment of this type to determine a more precise value for the proton charge radius than presently known. Both measurements rank among the best of this type and provide compared to [Sim80] some less precise values for the proton charge radius of $r_p = 0.861(20)$ fm [Bou96] and $r_p = 0.900(16)$ fm [Sch99], respectively. Bourzeix's measurement of the $1S_{1/2}$ Lamb shift has an error of 46 kHz, anyhow, the measurement of the same quantity of Schwob has an uncertainty of only 22 kHz. Additionally, Schwob et al. measured optically the classical Lamb shift in ^1H and attained a very precise value of 1057.8446(29) MHz.

Hagley and Pipkin [Hag94] managed to measure with rf methods the classical Lamb shift in ^1H with an uncertainty of 12 kHz, five years before the experiment of Schwob. The value they extracted from their measurement was 1057.839(12) MHz, which agrees with the measurement of Schwob. At this time a comparison of their result with Lamb shift calculations yielded the best agreement for the old proton charge radius of $r_p = 0.805(11)$ fm. The theoretical value for the classical Lamb shift at this stage was 1057.866(5) MHz, in contrast to the value 1057.884(5) MHz, which results from the more recent charge radius of $r_p = 0.862(12)$ fm. A new Lamb shift calculation [Pac01] yields a value of 1057.842(4) MHz for $r_p = 0.862(12)$ fm, which is in agreement with the measurement of Hagley and Pipkin.

⁷In 2005, among other things, Theodor Hänsch got the Nobel Prize for the precise determination of this frequency interval.

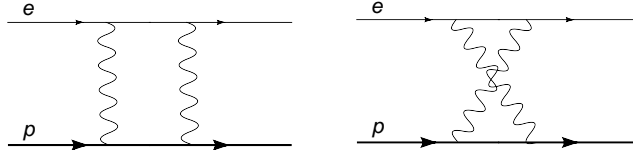


Figure 1.1: Two-photon exchange diagrams of the order $(Z\alpha)^5 m_e$ for the nuclear polarizability correction in hydrogen.

Another experimental value also registered in the present database of the classical Lamb shift in ^1H , obtained by a rf measurement, is known from the early eighties. In 1981, Lundeen and Pipkin [Lun81] determined a value of 1057.845(9) MHz. This value coincides with recent theoretical calculations, but did not agree with theoretical predictions performed by Erickson and Mohr (see references in [Lun81]) in the seventies, which Lundeen and Pipkin took as a basis for a comparison with their experimental value.

In 1984, in a very special experiment, Palchikov et al. [Pal85] measured with an atomic interferometer the classical Lamb shift in ^1H very precisely and obtained a value of 1057.8514(19) MHz. The uncertainty of this value is competitive with present optical measurements. Unfortunately, the experiment was stopped, but on the part of the leading theoreticians there is the wish to rebuild this experiment and reproduce the values of Palchikov et al. like mentioned in [Kar05].

In the case of ^2H , the list of recent measurements and calculations of the Lamb shift is much shorter than for ^1H . The reason behind the lack of theoretical efforts to perform Lamb shift calculations in this sort of atom, is the still incomplete knowledge of the deuteron structure and its influence on the atomic energy levels. Especially for absolute Lamb shift calculations the effect of nuclear polarizability in deuterium has to be understood much better. Because the deuteron is a weakly bound nucleus with a big mean distance of the proton to the neutron, the S electron is not only influenced by the deuteron as a whole, but senses its constituents separately. Furthermore, like in hydrogen, the S electron polarizes the nucleus and an additional attraction between the electron and the induced dipole emerges, which shifts the energy levels down, i.e. leads to a stronger binding energy of the electron. This effect can be described by a two-photon exchange between the electron and the nucleus in BSQED. The contributing diagrams of order $(Z\alpha)^5 m_e$ are shown in fig. 1.1 for the case of ^1H . Similar calculations for deuterium are also possible, but more complicated. Experimental determinations of the hydrogen-deuterium isotope shift and the theoretical interpretation in the framework of BSQED show that the nuclear polarizability effect in deuterium approximately coincides with the sum over the polarizabilities of

the nucleons. In the special case of the deuteron this can be understood classically, because the deuteron is composed of two nucleons which can be considered as quasi free due to the weak bond. In this chapter the deuteron charge radius was mentioned several times, which is another big unknown quantity in Lamb shift calculations of deuterium. How can it be defined? Based on the comparison between the calculated and the measured hydrogen-deuterium isotope shift of the $1S_{1/2} - 2S_{1/2}$ resonance, which results in a difference of 5235(22) kHz [Pac96], and substituting this difference into the nuclear size formula for S states, the following formula can be derived

$$r_d^2 - r_p^2 = 3.822(16) \text{ fm}^2 \quad ,$$

where the error of the value on the right hand side of the equation is composed of the experimental error of the measured $1S_{1/2} - 2S_{1/2}$ resonance and the error of the calculation, where generally the uncertainty in the electron-proton mass ratio and in recoil corrections contribute. Furthermore, r_p and r_d are the proton and deuteron charge radii. On the left hand side of the equation above the proton charge radius contributes. This means if the understanding of the hydrogen atom cannot be improved, especially if it is not possible to determine a more precise value for the proton charge radius, it is also impossible to reach similar accuracies for the deuteron charge radius from deuterium spectroscopy like for the proton charge radius from hydrogen spectroscopy. But nevertheless, the Lamb shift in deuterium can be taken to perform pure BSQED tests. This means as in the case of D_{21} , that leading FNS effects can be neglected by building a difference quantity

$$\Delta(n) = \Delta E_L(1S_{1/2}) - n^3 \Delta E_L(nS_{1/2}) \quad ,$$

where n is the principal quantum number. Compared to the absolute Lamb shift, the above difference can be calculated precisely, also for the hydrogen atom. The general expression and theoretical results can be looked up in [Kar97]. A precise measurement of the deuterium $1S_{1/2}$ and the classical Lamb shift was performed by Schwob et al. [Sch99] with an optical measurement. There exists no recent rf measurement of the classical deuterium Lamb shift. By comparing the experimental difference quantity $\Delta(n)_{exp}$ with the theoretical prediction, BSQED can also be tested by Lamb shift measurements in deuterium.

So far, only experiments with “electronic” atoms, like the hydrogen atom, were mentioned. Especially the great difficulty to obtain a more precise proton charge radius led to the serious consideration to perform a precise spectroscopy experiment of the Lamb shift in muonic atoms, i.e. atoms where the electron is replaced with a muon [Poh01]. Why do spectroscopy experiments in this sort of exotic atoms allow

approximately a twenty times more precise determination of the proton charge radius? First of all, the muon is about 206 times heavier than the electron, so its Bohr radius is much smaller, i.e. the highest density of the position probability of the muon is closer to the proton than in the case of the electron. This causes a stronger shift of the energy levels in muonic hydrogen due to the bigger influence of the proton in comparison to the hydrogen case. In hydrogen the FNS effect is about 0.01 % of the whole classical Lamb shift, i.e. about 145 kHz. In muonic hydrogen the same effect is about 2 % of the whole classical Lamb shift! Furthermore, the main contribution to the Lamb shift in muonic hydrogen is the polarization of the QED vacuum while in the hydrogen case this is the self energy of the electron in the Coulomb field of the nucleus (for further explanations of these effects contributing to the Lamb shift, see subsec. 2.1.3). Vacuum polarization calculations in muonic hydrogen were continuously improved over the past years and are now available at a precision level of 10^{-6} . So, muonic hydrogen is a sufficiently understood physical system to perform high-precision experiments and the results of the experiment of [Poh01] can be a big step forward to a more precise charge radius of the proton than known presently.

Until this point of the introduction, only measurements were presented, which were carried out in well shielded experiments to minimize the influence of electromagnetic fields on the transition frequencies. In the year 1940, in contrast to these experiments, Kusch, Millman and Rabi experimented with atoms in an external magnetic field. They were able to observe and to measure the ground state Zeeman effect of the hyperfine structure levels of ${}^6\text{Li}$, ${}^7\text{Li}$, ${}^{39}\text{K}$ and ${}^{41}\text{K}$ [Kus40]. Today's atomic physics experiments of this kind, like [Wer01], also carried out in external magnetic fields, intend to measure the ground state g factor of the electron bound in hydrogenlike ions, like for example in ${}^{12}\text{C}^{5+}$. They also provide a test of BSQED, because bound-state g factor calculations can be compared with the experimental values. Such experiments and all new ideas connected with them enjoy a big support, like for example from the Helmholtz Society within the scope of the HITRAP facility, which is a planned ion trap facility at GSI⁸. In addition to the measurement of the ground state bound-electron g factor, also many electron ions can be studied and precise experiments to measure nuclear magnetic moments can also be carried out [Qui01]. The well-known Breit-Rabi formula, which describes the energy dependence of the Zeeman sublevels in an external magnetic field, can be taken as a reference for the experimentalists. Nevertheless, for a good description of today's high-precision experiments in external magnetic fields, the Breit-Rabi formula had to be improved. This was done by Moskovkin and Shabaev [Mos06] for the ground-state Zeeman effect in 2006. They developed a fully relativistic theory of the Zeeman splitting of the ground-state hyperfine structure in hydrogenlike

⁸Gesellschaft für Schwerionenforschung, member of the Helmholtz Society

ions (subsec. 2.2.1). Because in such ions the Zeeman splitting is comparable to the hyperfine structure, this requires the construction of a perturbation theory of quasidegenerate states. The theory developed by Moskovkin and Shabaev holds for external fields up to 10 T for ground state ions. Above this field strength the Zeeman splitting is no longer comparable with the hyperfine splitting, but larger, so the constructed perturbation theory for quasidegenerate states is no longer valid. Although many experiments to perform atomic physics experiments in an external magnetic field are planned as mentioned above, there is no experiment planned to study excited atomic states in an external magnetic field. Twelve years after the publication of [Kus40], it was Rabi who published a short letter [Rab52] with the title “Atomic Beam Resonance Method for Excited States” where he states that the same method as used for the study of the ground state Zeeman effect should, even though connected with some difficulties, also be applicable for excited states.

The experiment which is described in this thesis will allow to study excited atomic states of hydrogen and deuterium atoms (with principal quantum number $n = 2$), also in an external magnetic field. In particular this means, that the $2S_{1/2}$ and $2P_{1/2}$ hfs can be measured. Additionally the classical Lamb shift can also be measured, as well as the Breit-Rabi diagrams of the first excited state. To have a theoretical basis as a reference for the results, for the first time the Breit-Rabi diagrams of the $2S_{1/2}$ and $2P_{1/2}$ states of hydrogen and deuterium were improved with methods of BSQED by Moskovkin and Glazov [Mos07a] and embedded in their relativistic theory in 2007. Because the hyperfine splitting of these states is just a fraction of the ground state hyperfine splitting, the theory holds only for small fields compared to the ground state case. A more detailed description can be found in sec. 2.2.

Chapter 2 summarizes the basics of quantum mechanics of the hydrogen and the deuterium atom and introduces the recent theory of these atoms. Furthermore, the theoretical background to understand the experiment is presented.

In chapter 3 the experimental setup is shown. The components of the experiment are explained and the concept of the measurement is summarized.

First measurements and results, respectively, are presented in chapter 4 and uncertainties of the transition frequencies are specified.

The thesis is finished with a conclusion and an outlook in chapter 5.

CHAPTER 2

THEORY

2.1 Quantum Theory of the Hydrogen and Deuterium Atom

2.1.1 Non-Relativistic Quantum Theory

In the following subsection, $|\psi\rangle \in \mathcal{E}_{\mathbf{r}} \subset \mathcal{H}$ denotes an element of the orbital state space $\mathcal{E}_{\mathbf{r}}$, subspace of the Hilbert space \mathcal{H} . In the framework of non-relativistic quantum theory, the “ket” $|\psi\rangle$ describes the state of a spinless particle, in the following text the state of the electron¹ in the hydrogen and the deuterium atom, respectively. The stationary Schrödinger equation² can be written in Dirac notation as follows

$$\hat{H}_S |\psi\rangle = E |\psi\rangle \quad , \quad (2.1)$$

where \hat{H}_S is the Hamilton operator of the spinless electron and E its energy eigenvalue. In the $|\mathbf{r}\rangle$ representation, eq. 2.1 can be written as

$$\left[-\frac{\hbar^2}{2\mu} \Delta + V(r) \right] \psi(\mathbf{r}) = E\psi(\mathbf{r}) \quad , \quad (2.2)$$

with the reduced mass³ μ , \hbar is the Planck constant divided by 2π and Δ is the Laplace operator. The potential $V(r)$ depends only on the variable r , because of the radial symmetry of the nuclear potential. Hence, eq. 2.2 can be transformed into spherical coordinates to obtain following equation

$$\hat{H}_S \psi(r, \theta, \phi) = E\psi(r, \theta, \phi) \quad , \quad (2.3)$$

¹The electron is characterized in non-relativistic quantum theory as a particle without spin. Only in the Dirac equation this additional quantum number will be added to the theory.

²Because the stationary Schrödinger equation is an eigenvalue equation, this allows a straightforward solution strategy.

³With the introduction of the reduced mass, the finite mass of the nucleon is taken into account and eq. 2.2 is reduced to an one-body problem in a central field. It has to be stressed that this is only a simplification. In the Dirac equation (subsec. 2.1.2), it is possible to introduce recoil corrections, which show that the hydrogen and the deuterium atom, respectively, are of course real two-body problems.

with the transformed Hamilton operator

$$\hat{H}_S = -\frac{\hbar^2}{2\mu} \frac{1}{r} \frac{\partial^2}{\partial r^2} r + \frac{1}{2\mu r^2} \hat{\mathbf{L}}^2 + V(r) \quad . \quad (2.4)$$

The properties of angular momenta in quantum mechanics, which are useful for the transformation of eq. 2.2, will not be summarized. For reference, [Coh77a] should be mentioned.

In the following, without performing any calculations, the general idea how to solve the eigenvalue equation eq. 2.3 is presented. First of all the potential $V(r)$ is left as a placeholder for an expression to be substituted later. In spherical coordinates the three components of the orbital angular momentum operator $\hat{\mathbf{L}}$ act only on the variables θ and ϕ . Therefore, $\hat{\mathbf{L}}$ commutes with all operators which only depend on the variable r . In addition, $\hat{\mathbf{L}}$ commutes with the Casimir operator $\hat{\mathbf{L}}^2$, so $[\hat{H}_S, \hat{\mathbf{L}}] = \mathbf{0}$ and $[\hat{H}_S, \hat{\mathbf{L}}^2] = 0$. Furthermore, the z component \hat{L}_z of the orbital angular momentum operator commutes with \hat{H}_S and $\hat{\mathbf{L}}^2$. Hence, it exists a basis in \mathcal{E}_r composed of common eigenfunctions of \hat{H}_S , $\hat{\mathbf{L}}^2$ and \hat{L}_z . Without restricting the generality of the problem, the functions $\psi(r, \theta, \phi)$ can be required to be these eigenfunctions. In particular it is, therefore, easy to solve the system of differential equations 2.5a-c shown below, because the eigenfunctions of the eqs. 2.5b and 2.5c are known [Coh77a]. These functions are the spherical harmonics $Y_l^{m_l}(\theta, \phi)$.

$$\hat{H}_S \psi(r, \theta, \phi) = E \psi(r, \theta, \phi) \quad (2.5a)$$

$$\hat{\mathbf{L}}^2 \psi(r, \theta, \phi) = \hbar^2 l(l+1) \psi(r, \theta, \phi) \quad (2.5b)$$

$$\hat{L}_z \psi(r, \theta, \phi) = m_l \hbar \psi(r, \theta, \phi) \quad (2.5c)$$

Here, l is the orbital angular momentum quantum number and m_l is the magnetic quantum number of the orbital angular momentum⁴. The common eigenfunctions which solve eqs. 2.5 can be written as a product of two functions, one depending only on the variable r and the second are the spherical harmonics, i.e. $\psi(r, \theta, \phi) = R(r)Y_l^{m_l}(\theta, \phi)$. $R(r)$, the radial wave functions, are only factors on both sides of the eqs. 2.5b and 2.5c, which cancel since $\hat{\mathbf{L}}^2$ and \hat{L}_z do not affect $R(r)$. The solutions of the eqs. 2.5b and 2.5c are already known and the remaining problem to be solved is finding a solution of eq. 2.5a. The radial wave functions have to be properly chosen so that $\psi(r, \theta, \phi) = R(r)Y_l^{m_l}(\theta, \phi)$ is also an eigenfunction of \hat{H}_S . Substituting the wave

⁴In this thesis, quantum numbers are written in small letters, except the quantum number of the nuclear spin and the total angular momentum quantum number of the atom which both will be introduced later.

function $\psi(r, \theta, \phi) = R(r)Y_l^{m_l}(\theta, \phi)$ in eq. 2.5a, the radial wave equation is obtained

$$\left[-\frac{\hbar^2}{2\mu} \frac{1}{r} \frac{\partial^2}{\partial r^2} r + \frac{\hbar^2 l(l+1)}{2\mu r^2} + V(r) \right] R(r) = ER(r) \quad . \quad (2.6)$$

With the substitution $R(r) \rightarrow \frac{1}{r}u(r)$ the simplified radial wave equation arises

$$\left[-\frac{\hbar^2}{2\mu} \frac{\partial^2}{\partial r^2} + \frac{\hbar^2 l(l+1)}{2\mu r^2} + V(r) \right] u(r) = Eu(r) \quad , \quad (2.7)$$

where the term in the square brackets is the l -dependent Hamilton operator $\hat{H}_{S,l}$. It is easily noticed, that the eqs. 2.6 and 2.7, respectively, diverge at $r = 0$ and solutions at this point do not exist. These divergencies cancel by modifying the radial wave equation. This can be done with suitable boundary conditions like e.g. $u(0) \stackrel{!}{=} 0$. Furthermore, it will be useful to subscript the radial wave functions and eigenvalues of the eqs. 2.6 and 2.7, respectively, with indices k and l . Here, k is the radial quantum number and denotes the different eigenfunctions and eigenvalues for fixed l .

In the framework of non-relativistic quantum theory, altogether the total wave function of a particle in the state $|k, l, m_l\rangle$ in a central potential $V(r)$ depends on three quantum numbers. The total wave function can be written in the $|\mathbf{r}\rangle$ representation as $\psi_{k,l,m_l}(r, \theta, \phi) = R_{k,l}(r)Y_l^{m_l}(\theta, \phi)$. The eigenvalues $E_{k,l}$ and the radial wave functions $R_{k,l}(r)$ are independent of the magnetic quantum number m_l of the orbital angular momentum, because \hat{L}_z does not appear in $\hat{H}_{S,l}$. Because of the mathematical structure of the spherical harmonics, for fixed l there are $2l+1$ possible values for m_l belonging to the same eigenvalue $E_{k,l}$. This is a basic property of every potential $V(r)$ of spherical symmetry and is called essential degeneracy. If now for $V(r)$ an expression for the potential energy of the electron situated in the Coulomb field of the proton and the deuteron, respectively, is substituted, i.e. $V(r) = -\frac{e^2}{4\pi\epsilon_0 r}$, so in particular $V(r) \propto r^{-1}$, then an additional energy degeneracy appears which is characteristic for the non-relativistic spectrum of the hydrogen (deuterium) atom. This additional degeneracy is called accidental degeneracy and is due to the Coulomb field of the nucleus. It leads to the effect, that for a given eigenvalue $E_{k,l}$ of the radial wave equation with fixed l , there exists another eigenvalue⁵ $E_{\tilde{k},\tilde{l}}$ which belongs to a radial wave equation with $\tilde{l} \neq l$.

Finally, only the solutions of eq. 2.7 and in the same moment of the equivalent eqs. 2.6 and 2.2 for $V(r) = -\frac{e^2}{4\pi\epsilon_0 r}$ are stated. Briefly spoken, a usual solution strategy consists of transforming eq. 2.7 into a dimensionless equation by changing variables and then by expanding $u_{k,l}(r)$ in a power series. By comparing the coefficients of this

⁵Fig. 2.2 exemplifies this effect by means of the degeneracy of the $2S$ and $2P$ level.

Table 2.1: Energy eigenvalues, radial wave functions and spherical harmonics up to $n = 2$ for hydrogen. E_I^H and a_0^H are the ground-state ionization energy and the Bohr radius.

$E_I^H = 13.59829 \text{ eV}, a_0^H = 0.53 \text{ \AA}$		
Energy [eV]	Radial Wave Function [$\text{\AA}^{-\frac{3}{2}}$]	Spherical Harmonics []
-13.59829	$n = 1, l = 0$ $2(a_0^H)^{-\frac{3}{2}} \exp\left(-\frac{r}{a_0^H}\right)$	$l = 0, m_l = 0$ $\frac{1}{\sqrt{4\pi}}$
-3.39957	$n = 2, l = 0$ $2(2a_0^H)^{-\frac{3}{2}} \left(1 - \frac{r}{2a_0^H}\right) \exp\left(-\frac{r}{2a_0^H}\right)$	$l = 0, m_l = 0$ $\frac{1}{\sqrt{4\pi}}$
-3.39957	$n = 2, l = 1$ $(2a_0^H)^{-\frac{3}{2}} \frac{1}{\sqrt{3}} \frac{r}{a_0^H} \exp\left(-\frac{r}{2a_0^H}\right)$	$l = 1, m_l = 0$ $\sqrt{\frac{3}{4\pi}} \cos \theta$ $l = 1, m_l = \pm 1$ $\mp \sqrt{\frac{3}{8\pi}} \sin \theta \exp(\pm i\phi)$

expansion and by applying well suited conditions to the radial wave function, a solution can be found and divergences can be excluded from the solution. By introducing the quantities $E_I = \frac{1}{2}\alpha^2\mu c^2$, the ground-state ionization energy, and $a_0 = \frac{1}{\alpha}\lambda_C$, the Bohr radius, energy eigenvalues and radial wave functions can be expressed in a compact way. Here, $\alpha = \frac{e^2}{4\pi\epsilon_0\hbar c} \approx \frac{1}{137}$ is the fine structure constant⁶, which is very important in physics, $\lambda_C = \frac{\hbar}{\mu c}$ is practically equal to the Compton wavelength of the electron and c is the speed of light. Because of the accidental degeneracy, the energy eigenvalues do not depend on k and l separately, but only on the sum $n = k + l$. Therefore, $E_{k,l} = -\frac{E_I}{(k+l)^2}$, valid for $k \geq 1$ and $l \geq 0$, can be replaced by $E_n = -\frac{E_I}{n^2}$, where n is the principal quantum number and l is in the range of $0 \dots n - 1$. The total degeneracy of one energy level n is then n^2 . The results for the hydrogen atom are summarized in table 2.1. For the deuterium atom, because of the slightly larger reduced mass ($\approx 0.03\%$), a smaller Bohr radius and a larger ionization energy is obtained, compared to the hydrogen atom. Substituting these values in the formulas shown in table 2.1, a similar table for the deuterium atom, not shown here, can be obtained. In fig. 2.1 the position probability density for the electron in the hydrogen atom is shown as a

⁶In physics all natural forces can be reduced down to four fundamental interactions. Characteristic for all these interactions is the range and the strength of the force. Physically spoken, the four fundamental interactions in nature can be distinguished by the related dimensionless coupling constants. The value of the coupling constant of the electromagnetic interaction, the second strongest force in nature, is $\alpha \approx 1/137$. Atomic processes are based on the electromagnetic interaction.

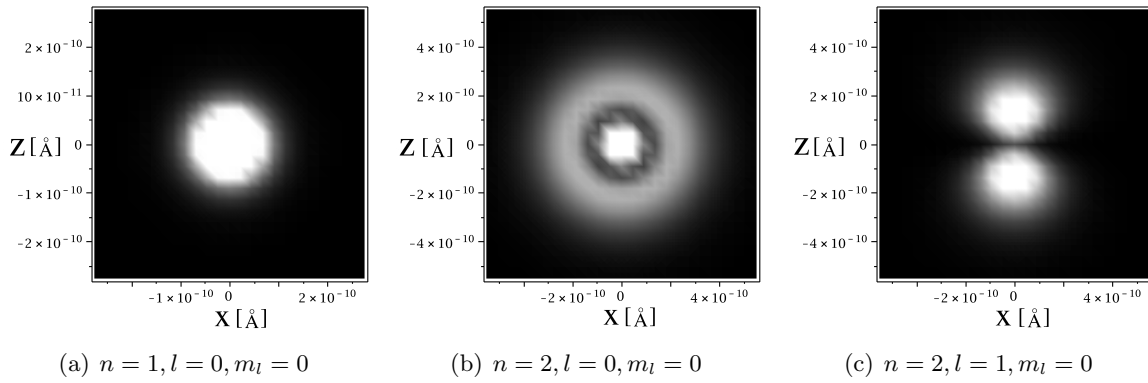


Figure 2.1: Position probability density $|\psi_{n,l,m}(r, \theta, \phi)|^2$ of the electron in the hydrogen atom shown as a density plot for different quantum states.

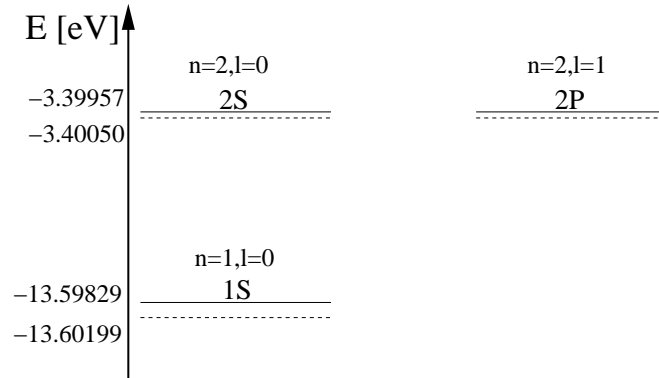


Figure 2.2: Level scheme of the hydrogen (solid line) and the deuterium atom (dashed line) up to $n = 2$. The spectroscopic notation allows a simplified designation of the particular state of the electron, e.g. $1S \hat{=} |n = 1, l = 0\rangle$. As a rule, the spectroscopic notation is composed of the value of the principal quantum number followed by a letter connected to the value of the orbital angular momentum quantum number l starting with the letter S for $l = 0$. For increasing l values the letters have to be increased alphabetically.

density plot for different quantum states. In fig. 2.2 the energy levels of the hydrogen and the deuterium atom are shown up to $n = 2$ as a result of the non-relativistic and, therefore, incomplete quantum theory. In the following subsections these energy levels will be adjusted by introducing more recent theoretical approaches like relativistic and quantum field theoretical effects as well as the hyperfine structure. As a result of this, finally, an energy spectrum which coincides very well with the experimental results can be obtained, which is the basis of modern atomic physics spectroscopy experiments.

2.1.2 Relativistic Quantum Theory - Electron Spin, Spin-Orbit Coupling and Fine Structure

In the last chapter the non-relativistic quantum theory of the hydrogen and the deuterium atom, respectively, was briefly presented. The spectrum of the energy levels, following from this non-relativistic approach, already describes the physical processes in these two atoms very well. Nevertheless, there are small relativistic corrections leading to the fine structure, which can be resolved by precision experiments. Furthermore, because of the success of special relativity, it is consequential to restate a relativistic quantum theory. In 1928, such a theory was established by Paul Dirac and the equation, connected to this relativistic theory, is called the Dirac equation

$$\hat{H}_D \Psi(\mathbf{r}) = E \Psi(\mathbf{r}) \quad , \quad (2.8)$$

with the Dirac Hamiltonian \hat{H}_D for the hydrogen and deuterium atom, respectively,

$$\hat{H}_D = \alpha_i \cdot p_i c + \beta \mu c^2 + \gamma^0 V(r) \quad , \quad (2.9)$$

and the energy eigenvalue (Dirac energy eigenvalue) E . Here $\alpha_i \cdot p_i$ is the short notation⁷ of the 3-dimensional scalar product in the euclidian space. α_i, β are 4×4 matrices defined as follows

$$\alpha_i = \begin{pmatrix} 0_{2 \times 2} & \sigma_i \\ \sigma_i & 0_{2 \times 2} \end{pmatrix} \quad \beta = \begin{pmatrix} \mathbb{1}_{2 \times 2} & 0_{2 \times 2} \\ 0_{2 \times 2} & -\mathbb{1}_{2 \times 2} \end{pmatrix} \quad , \quad (2.10)$$

where σ_i are the three Pauli matrices and $\gamma^0 = \beta$. Since α_i, β are matrices, $\Psi(\mathbf{r})$ cannot be a simple scalar wavefunction but has to be a spinor. The exact mathematical structure of the Dirac equation will not be explained in this chapter (see [Bjo90]). Nevertheless, a short motivation of the form of eq. 2.8 can be given. A first approach to determine a relativistic equation describing quantum mechanics is the Klein-Gordon equation

$$\left[\square + \left(\frac{m_e c}{\hbar} \right)^2 \right] \psi = 0 \quad , \quad (2.11)$$

with the d'Alembert operator \square and the electron mass m_e . This equation, important for today's description of spin-0 particles like the π mesons with their bosonic character, does not have exclusively positive definite energy solutions, but also negative energies. Furthermore, analogous to the Schrödinger equation, it is possible to determine a continuity equation for the Klein-Gordon equation, too. But for the latter one, the probability density is also not positive definite. Therefore, Dirac tried to

⁷Einstein summation convention, repeated indices are summed.

find a relativistic equation, which allows to determine a positive definite probability density like in the case of the Schrödinger equation. With this in mind, he started to linearize the Klein-Gordon equation. To gain the right energy-momentum equation, every spinor component of the Dirac equation has to fulfill the Klein-Gordon equation, so the matrices α_i and β have to fulfill the following algebra

$$\alpha_i \alpha_k + \alpha_k \alpha_i = 2\delta_{ik} \quad , \quad (2.12a)$$

$$\alpha_i \beta + \beta \alpha_i = 0_{4 \times 4} \quad , \quad (2.12b)$$

$$\alpha_i^2 = \beta^2 = \mathbb{1}_{4 \times 4} \quad . \quad (2.12c)$$

Starting from this algebra and the hermiticity of the Dirac Hamiltonian 2.9, i.e. \hat{H}_D has real eigenvalues, the matrices 2.10 can be determined. Dirac's equation could not solve the probability problem completely. From a modern point of view it is not possible to get such a relativistic equation describing just one particle. Naturally, negative energy solutions are included in such a theory which could not be interpreted with an exclusive positive definite probability density. The problems Dirac was facing in the development of his equation were the birth of the mathematical description of antiparticles. Negative energy states can be linked with antiparticles, so both the Dirac and the Klein-Gordon equation can be finally kept. The further development of relativistic quantum theory shows that a relativistic theory is a many particle theory including virtual particles which can be produced and annihilated due to vacuum fluctuations. In contrast to the Klein-Gordon equation, the Dirac equation describes particles with spin 1/2, so it is a theory of fermions. This becomes clear by transforming the Dirac Hamiltonian $\hat{H}_{EM} = \alpha_i \cdot (\mathbf{p} - \frac{e}{c}\mathbf{A}) + \beta\mu c^2 + e\phi$ of an electron in an external electromagnetic field to the corresponding Foldy-Wouthuysen Hamiltonian⁸. By combination of three canonical Foldy-Wouthuysen transformations, which are given for \hat{H}_{EM} in particular by the equation

$$U = \exp \left(-i\beta \frac{\alpha_i \cdot (\mathbf{p} - \frac{e}{c}\mathbf{A})}{2\mu} \right) \quad , \quad (2.13)$$

a reduced Hamiltonian can be obtained which includes a term of the form

$$\beta \frac{e}{2\mu} \sigma_i \cdot B_i \quad , \quad (2.14)$$

⁸The Hamiltonian \hat{H}_{EM} allows to study the Dirac equation near the non-relativistic limit in an electromagnetic field, where \mathbf{A} denotes the vector potential and ϕ is the electrostatic potential. In this limit an expression can be obtained which allows to interpret the electron as a particle with an additional angular momentum (spin) with values $\pm 1/2\hbar$. The Foldy-Wouthuysen transformation decouples the Dirac equation and allows to neglect negative energies.

where B_i is the i -th component of the magnetic field. In quantum mechanics it can be shown that the Pauli matrices can be obtained starting with a dimensionless operator $\hat{\sigma}$ represented in the $\{|\uparrow\rangle, |\downarrow\rangle\}$ basis, i.e. in a space consisting of only two states which can be assigned to an additional angular momentum of the electron called spin. Hence, electron spin and Pauli matrices are connected by the relation $\hat{\mathbf{S}} = \frac{\hbar}{2}\hat{\sigma}$. Substituting this relation into eq. 2.14, in contrast to the magnetic moment $\hat{\boldsymbol{\mu}}_l = -\mu_B\hat{\mathbf{L}}/\hbar$ connected with the orbital angular momentum at which μ_B denotes the Bohr magneton, the magnetic moment connected with the spin of the electron is twice as large. The ratio of the magnetic moment to the angular momentum, i.e. orbital angular momentum and spin, respectively, is expressed by the g factor which is $g_l = 1$ for $\hat{\boldsymbol{\mu}}_l$ and, according to the Dirac theory without binding (bound state) corrections,⁹ $g_s = 2$ for the magnetic moment $\hat{\boldsymbol{\mu}}_s$ of the electron spin. In the framework of BSQED, g_s will be modified by radiative corrections.

Transforming \hat{H}_D to a Foldy-Wouthuysen Hamiltonian by two canonical transformations given by

$$U = \exp\left(-i\beta\frac{\boldsymbol{\alpha}\cdot\mathbf{p}}{2\mu}\right) ,$$

all relativistic corrections to the Schrödinger theory can be obtained. One term in the transformed Hamiltonian is proportional to the product of spin and orbital angular momentum of the electron.

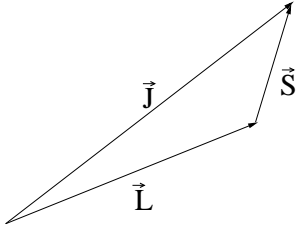


Figure 2.3: Spin orbit coupling in the vector picture.

Due to this product the spin-orbit coupling energy is added to the energy levels. In a pictorial way the mechanism of spin-orbit coupling can be described in the following way. The orbiting electron is a moving charge, so a magnetic field is produced due to the movement. In this magnetic field the electron spin can take on two values according to a spin up or a spin down state. Orbital angular momentum and spin couple to the total angular momentum of the atomic shell $\hat{\mathbf{J}} = \hat{\mathbf{L}} + \hat{\mathbf{S}}$ (fig. 2.3). Dependent on the spin direction, the energy differs which leads to a fine structure (fig. 2.4). To the total angular momentum $\hat{\mathbf{J}}$, a magnetic moment $\hat{\boldsymbol{\mu}}_j$ is connected similarly to the orbital angular momentum and the spin of the electron. In the vector

⁹In the year 1928, the same year Dirac found his equation, Breit described how the electron g factor, obtainable from the Dirac theory, has to be recalculated to include binding corrections. With these corrections the Dirac electron g factor differs from the value 2 as described in [Bre28] and later in sec. 2.2. It should be kept in mind, that although the g factor is recalculated in the framework of BSQED, even in the Dirac theory, taking the binding corrections of Breit into account, a g factor of a bound electron can be obtained.

picture¹⁰, the electron spin precesses in the magnetic field produced by the orbiting motion of the electron, so $\vec{\mu}_j$ precesses around the fixed position of \vec{J} . To state a similar equation for $\hat{\mu}_j$ like for $\hat{\mu}_l$ and $\hat{\mu}_s$, the mean value of $\hat{\mu}_j$ has to be taken, finally $\langle \vec{\mu}_j \rangle = -g_j \mu_B \cdot |\vec{J}|/\hbar$ can be determined in the vector picture with the g_j factor defined as

$$g_j = 1 + \frac{j(j+1) + s(s+1) - l(l+1)}{2j(j+1)}, \quad (2.15)$$

with the quantum numbers j of the total angular momentum of the atomic shell, l of the orbital angular momentum and s of the spin. Because of radiative corrections, g_j also has to be modified in the framework of BSQED. The other terms in the Foldy-Wouthuysen Hamiltonian besides the spin-orbit term is a term describing the relativistic variation of the mass with the velocity of the electron which leads to an energy correction of the order of α^2 and the Darwin term which considers the non-local interaction between an S electron and the Coulomb field of the nucleus leading to a correction of the same order. The effect leading to the Darwin term can be understood considering that the electron charge is spread over a domain equal to the Compton wavelength of the electron. Because of this, the “extended” electron is affected by all values of the Coulomb field in this domain. As will be seen later in subsec. 2.1.3 the electron emits and absorbs virtual photons which also spread the electron charge. Especially for S electrons this effect, leading to weaker binding of the electron, is the main contribution to the Lamb shift and can be determined from self-energy calculations¹¹.

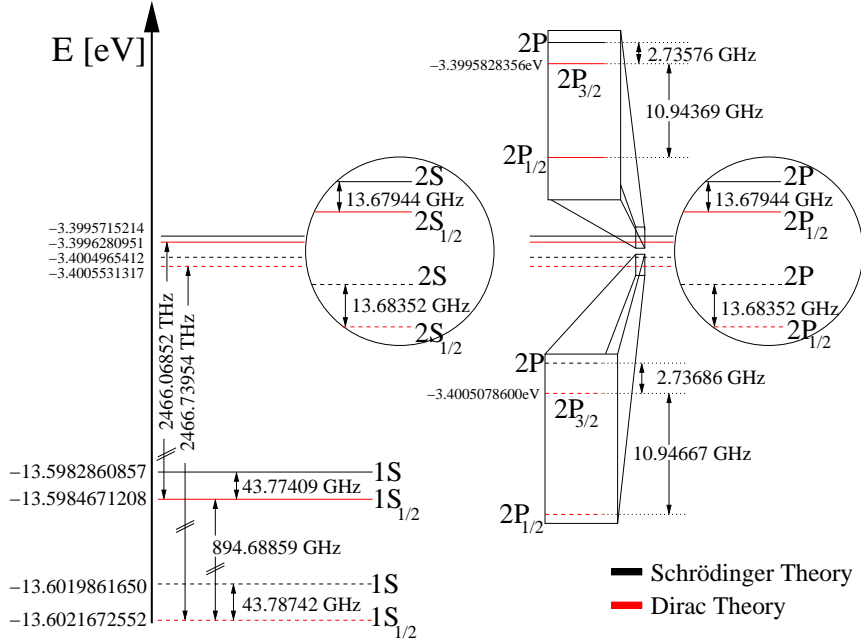
Solving the Dirac equation 2.8 relativistically leads to following energy eigenvalues

$$\begin{aligned} \tilde{E}_{n,j} &= \mu c^2 \cdot \left\{ \left[1 + \left(\frac{Z\alpha}{n - j - 1/2 + ((j + 1/2)^2 - Z^2\alpha^2)^{1/2}} \right)^2 \right]^{-1/2} - 1 \right\} \\ &\approx -\frac{\mu c^2 (Z\alpha)^2}{2n^2} + \mathcal{O}(\alpha^4) \end{aligned} \quad (2.16)$$

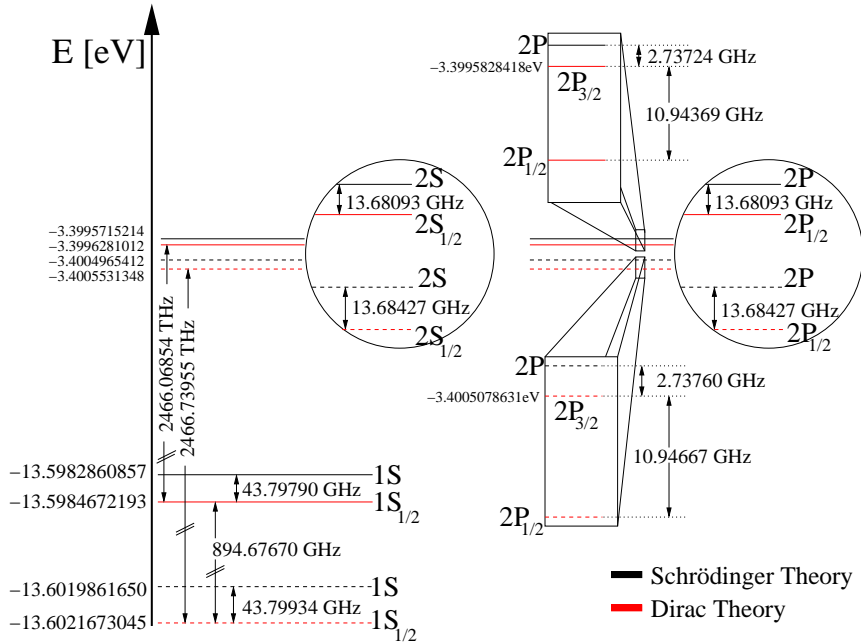
shown in fig. 2.4 (a), where the “ -1 ” in the first equation was introduced to get the right energy sign, Z is the nuclear charge number and the zero point of the energy was chosen in such a way that the rest mass of the electron can be excluded from the formula. The new quantum number j , the quantum number of the total angular momentum of

¹⁰For reasons of clarity, in the vector picture operators may be considered as vectors. In the notation the operator “hat” is then exchanged against a vector “arrow”. Furthermore, the bold notation is dropped in this case.

¹¹Consider an electron (bound or free). The presence of an electron implies that an electromagnetic field accompanies the electron. The interaction energy between the electron and the electromagnetic field (classical or quantized) due to the electron itself is called the self energy of the electron. Energy shifts in atomic levels due to the self energy of bound electrons are, to make a long story short, a residual effect obtained after subtraction of two large quantities, the self interaction of the bound electron with its own radiation field minus the same effect for the free electron. This is the concept of the self-energy renormalization procedure in BSQED.



(a) Dirac energy levels without recoil corrections.



(b) Dirac energy levels with recoil corrections.

Figure 2.4: Level scheme of the hydrogen (solid lines) and the deuterium atom (dashed lines) up to $n = 2$. Corrections from the Dirac theory to the energy levels are presented as red lines. In the two circular and rectangular areas, energy levels are magnified where the rectangular areas have the strongest magnification allowing to observe the fine structure. To obtain an unambiguous notation for the particular electron state connected with a Dirac energy eigenvalue, the spectroscopic notation has to be modified by writing j as a subscript like e.g. in the case for quantum numbers $n = 2, l = 1$ and $s = 1/2$. In this case l and s can couple to a total angular momentum of $j = 1/2$ or $j = 3/2$, so the modified spectroscopic notation reads as $2P_{1/2}$ and $2P_{3/2}$, respectively.

the atomic shell¹², appears in the eigenvalue equation 2.16. Energy values with the same j are still degenerate. The fine structure splitting in hydrogen and deuterium, respectively, is exemplified in fig. 2.4. Furthermore, eq. 2.16 was expanded up to fourth order in the fine structure constant. In this expansion the energy values of the Schrödinger theory can be obtained again. Expansion terms of higher order contribute only in even powers of $Z\alpha$, therefore, these terms are called relativistic corrections.

At the beginning of subsec. 2.1.1 it was mentioned in a footnote that introducing a reduced mass takes the finite mass of the nucleon into account and simplifies the non-relativistic quantum theory to an one-body problem in a central field. Even the Dirac theory could be simplified in this way. Of course, the full description of the hydrogen or the deuterium atom has to be done within a two-body problem. The Breit Hamiltonian¹³ describes this two-body problem and allows the determination of the following energy eigenvalues including recoil corrections to the energy levels [Sap90]

$$E_{n,j} = \mu c^2 [f(n,j) - 1] - \frac{\mu^2 c^4}{2(m_e + M)c^2} [f(n,j) - 1]^2 + \frac{(Z\alpha)^4 \mu^3 c^6}{2n^3 M^2 c^4} \left(\frac{1}{j + (1/2)} - \frac{1}{l + (1/2)} \right) (1 - \delta_{l0}) \quad , \quad (2.17)$$

where $f(n,j)$ is a function equal to the inverse root term in eq. 2.16 and M is the nucleon mass. The correction to the energy levels including recoil corrections are presented in fig. 2.4 (b) where the last term of eq. 2.17 was excluded from the calculation. Formally this term already belongs to the recoil corrections of order $(Z\alpha)^4$ of the Lamb shift explained in the next subsection. Comparing the energy levels in fig. 2.4 with and without recoil corrections, it can be noticed that the electron is bound slightly more strongly when recoil corrections are included in the calculation.

2.1.3 Quantum Electrodynamical Corrections to the Energy Levels

This chapter will introduce the last sort of corrections to the energy spectrum of the hydrogen and the deuterium atom, respectively, before taking the influence of the properties of the nuclear spin on the energy levels into account. In eq. 2.17 of the preceding subsection, the sum of all contributions to the energy levels of hydrogen or deuterium beyond the first two terms is called the Lamb shift, excluding hyperfine splitting contributions which are due to the nuclear spin and will be the topic of the next subsection. The theory of the Lamb shift is very complicated and cannot be discussed in all de-

¹²The theoretical basis of the mathematics of angular momentum coupling is the Racah formalism which can be looked up in nearly every advanced book of quantum mechanics.

¹³The derivation of this Hamiltonian is quite difficult. A very good description of the procedure can be found in the book of Berestetskii [Ber82].

tail in this thesis. In contrast to the theoretical concepts presented in the preceding subsections of this chapter, the Lamb shift has to be described within a complete new theoretical approach in the framework of quantum electrodynamics of bound atomic states. BSQED is a quantum field theory which describes the electromagnetic interaction of matter in bound systems such as atoms. For the fermion propagator¹⁴, in contrast to the free and unbound particle the free particle fermion propagator has to be replaced with a propagator describing bound atomic states. In Feynman diagrams¹⁵, propagators of this kind are characterized by double solid lines, describing the propagation of a bound particle in a Coulomb field while the free particle propagator is just one solid line.

In the classical theory, the electron is treated as a pointlike particle. Solving the non-relativistic Schrödinger equation for hydrogenlike atoms, the energies of the bound pointlike electron situated in the Coulomb potential of the nucleus can be obtained. In the last chapter, in the framework of the relativistic Dirac theory, the Darwin term was interpreted as a non-local interaction of the electron with the Coulomb field, leading to the interpretation of an extended electron charge distributed over a range comparable to the Compton wavelength of the electron which is in the order of 10^{-13} m. Although very small, in principle the Darwin term removes the degeneracy between the $2S_{1/2}$ and the $2P_{1/2}$ state in the Dirac theory, because this term acts only on S electrons. For the hydrogen case, in a very rough estimate in the framework of ordinary quantum mechanics, a shift of the $2S_{1/2}$ energy level of 2.4 Hz upwards can be obtained, originating from the Darwin term. For deuterium the shift is slightly larger, because of the smaller Bohr radius. So, estimates about the electron radius in the Dirac theory lead to the picture of an extended electron. However, the non-local character of the electron in the Dirac theory was only obtainable by looking at the relativistic corrections to the Schrödinger theory, i.e. so to say by looking at an approximation of the Dirac Hamiltonian which could be derived by the Foldy-Wouthuysen transformation of \hat{H}_D . In a fully relativistic language, even in the Dirac

¹⁴In QFT in general, the propagator describes the propagation of a particle. In a relativistic theory, particles can be produced and annihilated due to vacuum fluctuations. This processes are formally described with fermion and photon propagators in BSQED. For this quantum field theoretical conception there exists an classical analogy, the principle of Huygens. The evolution of a given wavefunction $\psi(\mathbf{x}, t)$, which can also be connected with a particle state, can be determined for later points in time by treating every point \mathbf{x} at a given time t as the source of a spherical wave propagating away from \mathbf{x} . Let $\psi(\mathbf{x}', t')$ be the wavefunction at a later point in time t' . The wavefunction $\psi(\mathbf{x}', t')$ will be proportional to the unprimed wavefunction where the constant of proportionality has the structure of a Green's function which is the building block of the propagators in QFT. This means, being aware of the propagator, the evolution of a particle state is also known.

¹⁵Feynman diagrams are a diagrammatic method to perform calculations in QFT, also in BSQED. These diagrams follow special rules, where each symbol included in one diagram stands for a mathematical expression. The rules are defined in each QFT separately because of the different interactions in different theories. For example, to determine the cross section for lepton-pair production in (e^+e^-) collisions, the Feynman amplitude for this process has to be calculated by evaluating the contributing Feynman diagrams to this process.

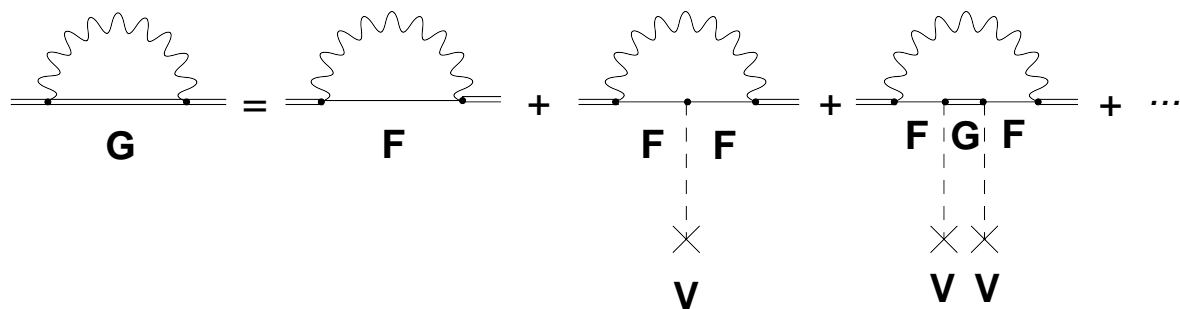


Figure 2.5: Exact expansion of the bound-electron propagator in powers of the binding Coulomb field [Jen04]. Double solid lines denote the bound-electron propagator, single solid lines the free-electron propagator, wavy lines are the virtual-photon propagator, dashed lines denote Coulomb photons and the cross is the interaction with the binding field. The letters G, F and V are abbreviated denotations for the bound-electron propagator, the free-electron propagator and for the Coulomb field. The time direction is from left to right.

theory, the electron is pointlike, so eqs. 2.16 and 2.17, respectively, without the last term of the sum predict a degeneracy between the $2S_{1/2}$ and the $2P_{1/2}$ states.

In BSQED, the quantization of the radiation field of electrodynamics allows to consider the following effects. The electron emits and absorbs virtual photons in a very short time scale which leads to the self-energy correction, the largest contribution to the Lamb shift in hydrogen and deuterium. As a result the electron charge is spread due to this effect which is exclusively describable in QED (BSQED). Because the Coulomb potential, as it was stated in the Schrödinger and Dirac theory, considers only pointlike electrons, it has to be corrected in BSQED because of the non-pointlike character of the electron obtained in this theory. The correction to the energy levels is proportional to $(Z\alpha) \langle r_e^2 \rangle \delta(\mathbf{r})$ ¹⁶, where $\langle r_e^2 \rangle$ denotes the squared mean value of the electron radius in the sense of QED (BSQED). In this context, the electron radius is two orders of magnitude smaller than the “classical” Compton wavelength of the electron. Actually, high energy electron-proton scattering experiments yield as an upper limit for the electron radius a value which is at least three orders of magnitude smaller than the Compton wavelength of the electron. The correction to the energy levels leads to a weaker binding of the S electron compared to the pointlike case, i.e. energy levels are shifted to higher energies. Since S electrons have a higher probability to penetrate the nucleus, the self-energy correction affects S electrons in the strongest way. The main contribution to the electron radius is described by the middle term of the bound-electron propagator expansion shown in fig. 2.5. The meaning of the terms of the sum will be described below.

¹⁶Because of the proportionality of the energy shift to the factor $(Z\alpha)$, the source of the huge uranium Lamb shift which is subject of current research, can be understood quite easily.

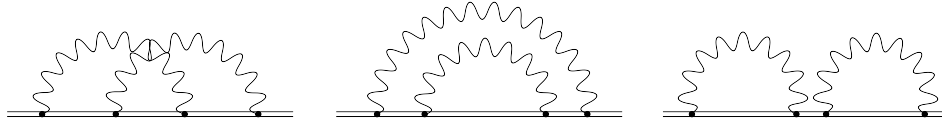


Figure 2.6: Two-photon electron self energy. To consider the interaction with the binding field, nineteen topological different graphs of the kind shown in this figure have to be included into the calculation of the two-loop self energy. Therefore, the Coulomb binding field has to be included [Pac96].

The second-strongest contribution to the Lamb shift in hydrogen and deuterium is the vacuum polarization. The leading order Feynman diagram is shown in fig. 2.7. In the BSQED picture, the electron and the nucleus exchange virtual photons, which can produce a virtual electron-positron pair, indicated by the fermion loop in fig. 2.7, shown as a double solid circle. The polarization of the QED vacuum acts like a dipole, because the virtual positron is repelled in the Coulomb field of the nucleus while the virtual electron is attracted.

Atomic electrons with different angular momenta, i.e. different position probabilities to penetrate the nucleus, see different nuclear charges. Electrons with a high probability to penetrate the nucleus, these are the S electrons, almost sense the full nuclear charge while P electrons sense a screened charge, because of the virtual electron-positron pairs between nucleus and electron. This means, because of vacuum polarization effects, that S electrons are bound more strongly, i.e. the corresponding energies are lowered, while P electrons are bound more weakly and their levels are raised to higher energies.

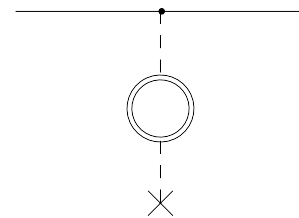


Figure 2.7: Leading order vacuum-polarization diagram.

In this simple concept, for S electrons for example, the self-energy correction is a repulsive effect while vacuum polarization is an attractive effect. Only considering both effects for any atomic state gives the right Lamb shift.

Besides the one-loop calculations as shown in figs. 2.5 and 2.7, respectively, higher order contributions can also be calculated, like exemplified in fig. 2.6 for the self energy.

In addition to the self energy and the vacuum polarization, also non-QED effects contribute to the Lamb shift. This is the recoil correction, the radiative recoil correction and nuclear size effects. The latter is completely neglected in the Schrödinger and the Dirac theory, here in addition to the electron the nucleus is also pointlike.

A few words to the renormalization procedure in QED should be mentioned. First of all, what is renormalization? To answer this question it should be mentioned, that QED is a local quantum field theory. Mathematically this means that the product of

charge conjugation \mathcal{C} , parity \mathcal{P} and time reversion \mathcal{T} is an exact symmetry, i.e. it is invariant under the combined transformation \mathcal{CPT} , for all particles to be described with this theory and for all interactions between the particles. As a result, for example the lifetime and the mass of particles and antiparticles which can be described in the framework of QED have to be the same. Furthermore, if there would exist a process in QED which is not invariant under a single operation \mathcal{C} , \mathcal{P} or \mathcal{T} , then this process would not be invariant with respect to the combined two other operations as well. As a well-known example that this is not the case in QED, the electron and the positron can be taken. The problem of a local quantum field theory such as QED is, that virtual processes have to be taken into account up to any desired energy. This leads naturally to divergences in the theory, for example to divergent integral equations. It is possible in renormalization theory to obtain finite results by renormalizing the theory. Especially in the QED of hydrogenlike atoms this means that divergences are absorbed in a “renormalized” electron charge and mass (counter terms). The results which can be obtained after renormalization of QED are until to the present day the most precise results ever obtained from theory. They are in addition in a nearly perfect agreement with the experimental results. Now, a rough idea will be given how the bound electron propagator is connected to the self-energy correction. First of all, following [Jen04], the free electron propagator F and the bound electron propagator G are

$$F(z) = \frac{1}{\alpha_i \cdot p_i + \beta - z} \quad \text{and} \quad (2.18a)$$

$$G(z) = \frac{1}{\alpha_i \cdot p_i + \beta + \gamma^0 V - z} \quad . \quad (2.18b)$$

The speed of light c and the reduced mass μ are set equal to one in the above equations, the energy variable $z = E_{n,j} - \omega$ where $E_{n,j}$ is the Dirac energy eigenvalue and ω is the complex valued energy of the virtual photon. Furthermore, the short matrix notation is used, because the propagators are 4×4 matrices. The bound electron propagator can be expanded to the following expression

$$G(z) = F(z) - F(z)V F(z) + F(z)V G(z)V F(z) + \dots \quad , \quad (2.19)$$

which is the formal analogon to the diagrammatic expansion shown in fig. 2.5 where the “ $-$ ” in the formula is substituted into the diagram in the corresponding figure. The following equation has to be solved to obtain the self-energy correction [Jen04]

$$\begin{aligned} \Delta E_{SE} &= \lim_{\Lambda \rightarrow \infty} \left\{ i e^2 \Re \int_{C_F} \frac{d\omega}{2\pi} \int \frac{d^3\mathbf{k}}{(2\pi)^3} D_{\mu\nu}(k^2, \Lambda) \langle \bar{\phi} | \gamma^\mu G(z) \gamma^\nu | \phi \rangle \Delta m \right\} \\ &= \frac{\alpha (Z\alpha)^4}{\pi n^3} \tilde{F}(nl_j, Z\alpha) m_e c^2 \quad , \end{aligned} \quad (2.20)$$

where Λ is the ultraviolet cut-off parameter which resolves QED at high energies of the virtual photon, i.e. when the angular wavenumber $k \rightarrow \infty$, $D_{\mu\nu}$ is the photon propagator in covariant notation which describes the evolution of the virtual-photon state denoted by the wavy lines in fig. 2.5, $\bar{\phi}, \phi$ are Dirac fields, $\gamma^i = \beta\alpha_i$ are the γ matrices and Δm is the one-loop mass-counter term which has to be considered because of renormalization of the theory. The integration contour C_F is split into a low-energy and a high-energy part for the ω integration. Performing the integration gives the scaled self-energy function $\tilde{F}(nl_j, Z\alpha)$ which depends for a given atomic state only on the parameter $Z\alpha$. A further insight into the integral equation should be left to the reader ([Jen04]). Substituting the values for $\tilde{F}(nl_j, Z\alpha)$ into eq. 2.20 gives the self-energy contribution for the given state, e.g. for the $2P_{1/2}$ state $\tilde{F}(2P_{1/2}, Z\alpha) = -0.12639637$ while for the $2S_{1/2}$ state $\tilde{F}(2S_{1/2}, Z\alpha) = 10.546825185$. This means, because of the self-energy correction the energy shift of the Dirac energy for the $2P_{1/2}$ state is downwards and for the $2S_{1/2}$ state upwards. Although the sign of the energy shift due to self-energy correction for S states can be obtained without calculation as described at the beginning of this subsection, the energy shift due to the same effect for P states is not accessible to such a simple explanation and has to be calculated. For the very reason the $2P_{3/2}$ self-energy correction shifts the level in the same direction as for the S states which can be seen in table 2.2.

Before presenting the values of the Lamb shift of the particular atomic states, the formula to calculate the Lamb shift as a correction to the Dirac energy levels is shown. In this formula the F -function appears [Pac01]

$$\begin{aligned}
F(nl_j, Z\alpha) = & A_{40}(nl_j) + A_{41}(nl_j)L + (Z\alpha)A_{50}(nl_j) \\
& + (Z\alpha)^2 [A_{62}(nl_j)L^2 + A_{61}(nl_j)L + A_{60}(nl_j, Z\alpha)] + \frac{\alpha}{\pi} [B_{40}(nl_j) + (Z\alpha)B_{50}(nl_j) \\
& + (Z\alpha)^2 \{B_{63}(nl_j)L^3 + B_{62}(nl_j)L^2 + B_{61}(nl_j)L + B_{60}(nl_j, Z\alpha)\}] + \left(\frac{\alpha}{\pi}\right)^2 C_{40}(nl_j) \quad , \\
\end{aligned} \tag{2.21}$$

where the coefficients A_{xy} are due to one-loop calculations such as shown in figs. 2.5 and 2.7, respectively, the subscript $x = Z\alpha$ is the order of the expansion and y is the order of $L = \ln(m_e/[\mu(Z\alpha)^2])$. The B_{xy} coefficients originate from two-loop calculations such as shown in fig. 2.6. A recent subject in theoretical atomic physics is the term C_{40} . The contribution of this term to the Lamb shift can be determined by evaluating three-loop Feynman diagrams. Such calculations yield also contributions due to hadronic and muonic vacuum-polarization effects, i.e. the fermion loop in the leading order vacuum-polarization diagram shown in fig. 2.7 contains also $\mu^+\mu^-$ pairs and arbitrary hadronic states which are created and subsequently annihilated. Because of these effects, for

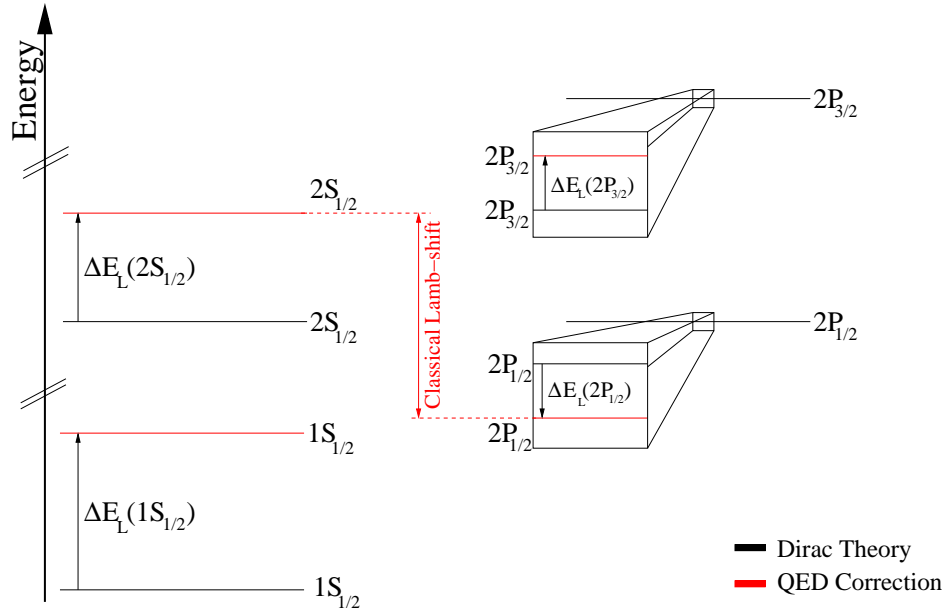


Figure 2.8: Quantum electrodynamical corrections to the energy levels of fig. 2.4 (b). The values for the Lamb shift of hydrogen and deuterium, respectively, are shown in the table below.

Table 2.2: Most recent values of the Lamb shift for different atomic states, the unit is MHz. The lack of theoretical values for deuterium should not be misunderstood. As mentioned in the introduction of this thesis only absolute values for this sort of atom are difficult to calculate. As a basic rule, the n^{-3} scaling of the Lamb shift should be mentioned which has its origin in eq. 2.20.

Lamb shift	Hydrogen		Deuterium	
	Experiment	Theory	Experiment	Theory
$\Delta E_L(1S_{1/2})$	8172.837(22) [Sch99]	8172.816(32) [Pac01]	8183.966(22) [Sch99]	—
$\Delta E_L(2S_{1/2} - 2P_{1/2})$	1057.844 6(29) [Sch99]	1057.842(4) [Pac01]	1059.233 7(29) [Sch99]	—
$\Delta E_L(2P_{1/2})$	—	-12.836 0(3) [Jen03]	—	—
$\Delta E_L(2P_{3/2})$	—	12.517 5(3) [Jen03]	—	—

the $1S_{1/2}$ Lamb shift a contribution of -8.5 kHz can be determined and for the $2S_{1/2}$ Lamb shift a contribution of about -1.1 kHz, respectively. In comparison to the $\mu^+\mu^-$ pairs, vacuum-polarization effects with the heavier $\tau^+\tau^-$ leptons in the fermion loop contribute only with -0.02 kHz to the $1S_{1/2}$ Lamb shift and with only -2.5 Hz to the $2S_{1/2}$ Lamb shift [Kar95, Fri99, Mel00]. To calculate the Lamb shift ΔE_L for all atomic states, the whole formula is divided in several contributions to the Lamb shift. The contribution due to the quantization of the radiation field which does not vanish in the limit $M \rightarrow \infty$, i.e. in the non-recoil limit, is

$$\Delta E_{QRF}(nl_j, Z\alpha) = m_e c^2 \frac{\alpha(Z\alpha)^4}{\pi n^3} \left(\frac{\mu}{m_e} \right)^3 F(nl_j, Z\alpha) \quad , \quad (2.22)$$

where the subscript ‘‘QRF’’ stands for ‘‘quantized radiation field’’. In addition there exists the recoil correction ΔE_R . Up to order $(Z\alpha)^4$ this correction has the form of the last term of the sum of eq. 2.17. Higher order recoil corrections can be looked up in [Pac01] and should not be given explicitly at this point. As a last contribution to the Lamb shift, the finite size of the nucleus has to be included. In the introduction, the corrections for S and P states were mentioned. From the quantum electrodynamical point of view without including the nuclear spin, the energy levels can be calculated from following formula

$$E_{n,l,j} = E_{n,j} + \Delta E_L(nl_j) \quad , \quad (2.23)$$

with the Dirac energy eigenvalue $E_{n,j}$ with recoil corrections included which depends on the quantum numbers n, j and the Lamb shift $\Delta E_L(nl_j)$ depending additionally on the quantum number l .

2.1.4 Hyperfine Splitting - Explicit Formula versus D_{21} Theory

As mentioned in the previous chapter, to obtain the last contribution to the energy levels of hydrogen and deuterium, nuclear properties have to be taken into account. These lead to the hfs which can for the first moment, unlike the Lamb shift, be understood in the framework of non-relativistic quantum mechanics. The hfs originates from the interaction of the magnetic moment of the electron with the magnetic moment of the nucleus. In a very simple point of view, the magnetization distribution inside the nucleus leading to a magnetic moment $\vec{\mu}_I$ which is proportional to the nuclear spin, is considered to be pointlike, producing a ‘‘pointlike’’ magnetic dipole. Similar to the magnetic moment of the electron, the magnetic moment of the nucleus can be expressed by replacing the electron g factor, the total angular momentum of the atomic shell and the Bohr magneton against the nuclear g factor, the nuclear spin and the nuclear magneton. In the case of the fine structure, the electron spin could take on two values in

the magnetic field produced by the motion of the electron itself resulting in an energy separation, the fine structure. Analogously, the hfs arises from the interaction of the nuclear magnetic moment and its spin, respectively, with the magnetic field produced by the electron.

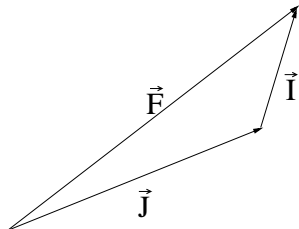


Figure 2.9: Coupling of the total angular momentum of the atomic shell with the nuclear spin to the total angular momentum of the atom.

Because of this, there is a coupling between the total angular momentum of the atomic shell and the spin of the nucleus (fig. 2.9), leading to the total angular momentum of the atom $\hat{\mathbf{F}} = \hat{\mathbf{J}} + \hat{\mathbf{I}}$, very similar to the spin-orbit coupling resulting in the fine structure. In this simple approach to the hfs, no assumptions about the dimension or the structure of the nucleus have to be taken into account, so mathematically the nucleus is treated as a pointlike particle. According to this, the hyperfine interaction can simply be written as

$\tilde{V}_{hfs} = -\vec{\mu}_I \mathbf{B}_J$ where \mathbf{B}_J is the magnetic field around the nucleus produced by the electron motion and \tilde{V}_{hfs} is labeled with a “tilde” to distinguish it from V_{hfs} introduced later in subsec. 2.2.1. In total, the energy correction which has to be added to eq. 2.23 due to the hfs can be written as

$$\Delta E_{hfs}^{(nl_j)}(F) = \frac{a_{pt}^{(nl_j)}}{2} \left[F(F+1) - I(I+1) - j(j+1) \right] , \quad (2.24)$$

where F, I, j are the quantum numbers of the total atomic angular momentum $\hat{\mathbf{F}}$, of the nuclear spin $\hat{\mathbf{I}}$ and of the total angular momentum of the atomic shell $\hat{\mathbf{J}}$. With $a_{pt}^{(nl_j)}$ the hyperfine constant is denoted which is state dependent, also known as the interval constant where the subscript should imply that a simplified pointlike magnetization distribution is assumed. Referring to the formula of Fermi-Segrè, for an S electron, $a_{pt}^{(nS_{1/2})}$ is proportional to $|\psi(0)|^2$. For electrons with $l \neq 0$, $|\psi(0)|^2$ is zero. In this case the dipole-dipole interaction between electron and nucleus has to be calculated to determine the hfs which results in a smaller hfs as for electrons with $l = 0$. Therefore, for hydrogen and deuterium a rough calculation for the different hfs yields a simple rule. The ground-state hfs, which is also known as the Fermi energy E_F , has to be multiplied by a factor of 1/8 to determine the $2S_{1/2}$ hfs, by a factor of 1/24 to determine the $2P_{1/2}$ hfs and by a factor of 1/60 to determine the $2P_{3/2}$ hfs. Only in the case of the hydrogen atom, the hfs calculated in this way is equal to the interval constant which can be substituted into eq. 2.24 to calculate the energy correction to eq. 2.23 for, in principle, any atomic state. As an example, substituting the values for the hydrogen $2S_{1/2}$ state into eq. 2.24, the interval rule can be obtained which is exemplified in

fig. 2.10. In this example, the 3-fold degenerate state with $F = 1$ is weighted with a factor of $1/4$ while the non-degenerate state belonging to $F = 0$ is weighted with a factor of $-3/4$. For the deuterium ground state, $F = 3/2$ and $F = 1/2$. Applying the formula of Fermi-Segrè for the deuterium ground state, the interval constant is $2/3$ times the ground-state hfs of deuterium. According to the interval rule, the weighting of the hyperfine levels, i.e. the number the hyperfine constant is multiplied with, is, therefore, $1/2$ and -1 belonging to $F = 3/2$ and $F = 1/2$. The spacing of this doublet is then $3/2$ times the interval constant and the result is equal to the ground-state hfs of deuterium. Multiplying the ground-state interval constant of deuterium by $1/8$ and applying again the interval rule, yields the energy correction for the $2S_{1/2}$ state in deuterium which can be easily carried forward to the example shown in fig. 2.10 as mentioned in the caption of the figure. For the case of deuterium in the first excited state, in this thesis only the states with $F = 3/2$ and $F = 1/2$ are important.

As described in the last subsection, the extension of the nucleus has influences on the Lamb shift, i.e. influences on the atomic spectrum. The same applies to the hfs. Until this point only a very simple method to calculate the hfs of the atomic states of hydrogen and deuterium was briefly presented. For a more precise determination of the hfs of a given atomic state, nuclear contributions to the hfs have to be included. Like mentioned in the introduction, these are the Breit-Rosenthal-Crawford-Schawlow and the Bohr-Weisskopf corrections taking the charge and magnetization distribution of the extended nucleus into account. So, in contrast to the preceding simple approach, considering only a pointlike nucleus, now the charge and magnetization distribution is finite extended like exemplified in fig. 2.11 for the magnetization distribution. An extended charge distribution of the nucleus modifies the electron wave function, the extended magnetization distribution changes the hyperfine interaction, i.e. the magnetic moment itself. The hyperfine constant, therefore, can be written as [Boh50]

$$a^{(nl_j)} = a_{pt}^{(nl_j)} (1 + \delta^{(nl_j)}) (1 + \epsilon^{(nl_j)}) \quad , \quad (2.25)$$

where $\delta^{(nl_j)}$ is the charge distribution correction to the hfs for an atomic state $|n, l, j\rangle$ and $\epsilon^{(nl_j)}$ is the magnetization distribution correction. Especially in the non-relativistic approximation (i.e. $Z\alpha \ll 1$ which is valid for hydrogen and deuterium) for the orbital angular momentum quantum number $l = \{0, 1\}$, $\delta^{(nl_j)} \propto \sqrt{5/3} \langle r^2 \rangle$. Calculations of the magnetization distribution correction are more challenging and can be looked up in [Sha94].

Two different approaches for a theoretical description of the hfs will be discussed, where also QED is considered which has an influence on the hfs.

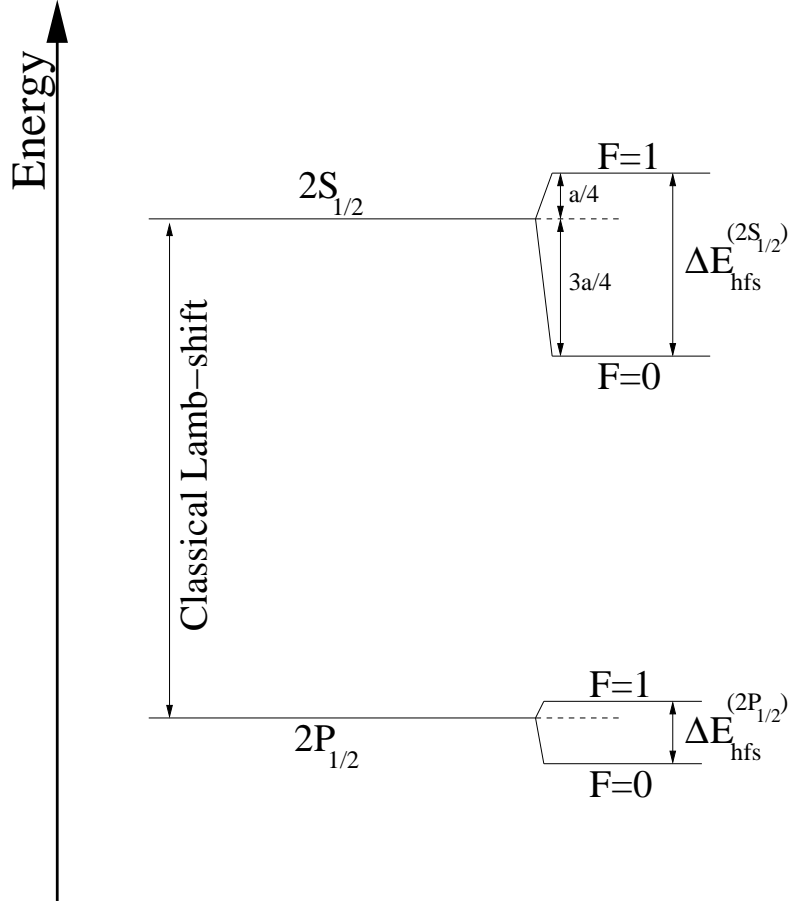


Figure 2.10: Scheme of the hyperfine splitting (not to scale!) in hydrogen as last contribution to the $2S_{1/2}$, $2P_{1/2}$ energy levels. The states with $F \neq 0$ are $(2F + 1)$ -fold degenerate. Other energy levels are hidden, because the $2S_{1/2}$, $2P_{1/2}$ levels are the important part of the hydrogen and deuterium spectrum in this thesis. For the case of deuterium, the $F = 1$ and $F = 0$ states of hydrogen in this figure have to be replaced against the $F = 3/2$ and $F = 1/2$ states of deuterium. Applying the interval rule as described previously in this subsection, gives the hfs correction for the $2S_{1/2}$ and $2P_{1/2}$ states in deuterium.

Table 2.3: Hyperfine splitting values for the $2S_{1/2}$ and $2P_{1/2}$ states used for the Breit-Rabi diagram calculations of sec. 2.2, all values in MHz.

Hyperfine Splitting	Hydrogen		Deuterium	
	Experiment	Theory	Experiment	Theory
$\Delta E_{hfs}^{(2S_{1/2})}$	177.556 860(16) [Kol04b]	—	40.924 454(7) [Kol04a]	—
$\Delta E_{hfs}^{(2P_{1/2})}$	—	59.221 2 [Mos07b]	—	13.636 2 [Mos07b]

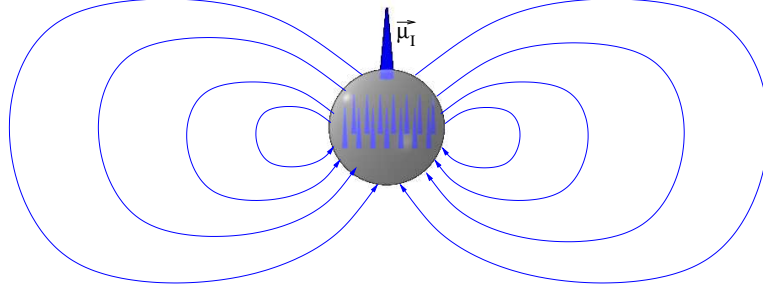


Figure 2.11: Study of the extended proton with the uniform non-pointlike magnetization distribution inside the nuclear volume (little blue arrows) resulting in the magnetic moment $\vec{\mu}_I$ (big blue arrow) and an extended dipole field (blue lines) at a distant point outside the nucleus. In practice, the interaction which leads to the hfs can be reduced to a magnetic dipole interaction and an electric quadrupole interaction. The latter interaction appears for nucleons with spin $I \geq 1$ and is also important for a precise treatment of the Breit-Rabi formula calculation for deuterium, explained in subsec. 2.2.1.

The most intuitive strategy would be to state an equation of the hfs where the mentioned corrections are taken into account. To determine the hfs for a given state in order to describe the experiments in an accurate way (say spectroscopy experiments to determine the hfs), “only” the distributions $\delta^{(nl_j)}$ and $\epsilon^{(nl_j)}$ have to be determined. Following [Mos07b, Sha94], for the $2S_{1/2}$ and the $2P_{1/2}$ state, which are the important states for this thesis, these equations are

$$\Delta E_{hfs,theo}^{(2S_{1/2})} = \left(1 + \frac{m_e}{M}\right)^{-3} \frac{1}{6} \alpha(\alpha Z)^3 \frac{\mu_I}{\mu_N} \frac{m_e}{m_p} \frac{2I+1}{2I} m_e c^2 \cdot \left[A^{(2S_{1/2})}(\alpha Z) (1 - \delta^{(2S_{1/2})}) (1 - \epsilon^{(2S_{1/2})}) + x_{rad}^{(2S_{1/2})} \right] \quad , \quad (2.26a)$$

$$\Delta E_{hfs,theo}^{(2P_{1/2})} = \frac{1}{18} \alpha(\alpha Z)^3 \frac{\mu_I}{\mu_N} \frac{m_e}{m_p} \frac{2I+1}{2I} m_e c^2 \cdot \left[A^{(2P_{1/2})}(\alpha Z) (1 - \delta^{(2P_{1/2})}) (1 - \epsilon^{(2P_{1/2})}) + x_{rad}^{(2P_{1/2})} \right] \quad , \quad (2.26b)$$

where μ_N is the nuclear magneton, m_p is the proton mass, M is the nuclear mass, $x_{rad}^{(nl_j)}$ are the QED corrections [Bro66] and $A^{(nl_j)}(\alpha Z)$ are the relativistic factors which are in the $2S_{1/2}$ and the $2P_{1/2}$ state

$$A^{(2S_{1/2})}(\alpha Z) = \frac{2 \left[2(1 + \gamma) + \sqrt{2(1 + \gamma)} \right]}{(1 + \gamma)^2 \gamma (4\gamma^2 - 1)} \quad \text{and} \quad (2.27a)$$

$$A^{(2P_{1/2})}(\alpha Z) = \frac{6 \left[2(1 + \gamma) - \sqrt{2(1 + \gamma)} \right]}{(1 + \gamma)^2 \gamma (4\gamma^2 - 1)}, \quad (2.27b)$$

with the parameter $\gamma = \sqrt{((-1)^{j+l+1/2}(j+1/2))^2 - (\alpha Z)^2}$. With eqs. 2.26 an absolute value for the hfs can be determined which is an important parameter for the Breit-Rabi diagrams to be described in the next section. If the hfs values, determined with the equations above, are included into eq. 2.23, the interval rule has to be applied, as described previously. Although in eqs. 2.26 the crucial corrections are included, the lack of knowledge about the proton charge radius which affects the charge distribution correction causes the largest error in the calculation of the $2S_{1/2}$ hfs. In addition, another uncertainty is the structure of the magnetization distribution. As an example, the ground-state hfs of hydrogen is one of the most precise measured values in physics [Ram93] (precision level of about $63 \cdot 10^{-12}$). This result cannot be obtained with the same precision in theory because of the lack of knowledge of the nuclear structure. Pure QED corrections to the hfs are known up to a precision of 0.12 ppm, which can be further improved in precision, while nuclear structure effects contribute with an amount of approximately 40 ppm to the energy levels and an error which is bigger than the uncertainty of the pure QED contribution! Nevertheless, for the precise Breit-Rabi diagrams of the first excited state of hydrogen and deuterium described in sec. 2.2, for the first time calculated with methods of BSQED in a relativistic approach by [Mos06, Mos07a] for this thesis, also precise values of the hfs with an accurate description of nuclear properties are needed. Because of these problems to take nuclear effects accurately into account, for the $2S_{1/2}$ hfs an experimental value was chosen while the $2P_{1/2}$ hfs value was calculated by [Mos07b]. The calculation of the $2P_{1/2}$ hfs is not so much influenced by nuclear structure properties, so a pure theoretical approach should describe the experiment sufficiently. As can be seen in [Sha94], in addition to the $\sqrt{5/3} \langle r^2 \rangle$ proportionality, valid for $S_{1/2}$ and $P_{1/2}$ states, $P_{1/2}$ states are also proportional to $\frac{n^2-1}{n^2} (\alpha Z)^3$. This leads to the approximation $\delta^{(2P_{1/2})} \approx \delta^{(2S_{1/2})} \cdot 10^{-4}$. Because of that, at the moment $\delta^{(2P_{1/2})}$ is neglected in eq. 2.26b, as well as the magnetization distribution correction. Furthermore, since the QED correction $x_{rad}^{(2P_{1/2})}$ is not calculated carefully so far, it is also neglected. Thus, the uncertainty of $\Delta E_{hfs,theo}^{(2P_{1/2})}$ cannot be determined from the theoretical side at the moment. Therefore, it is clear that an experiment is necessary to provide precision measurements in the $2P_{1/2}$ state. Among other measurements, like the determination of the $2S_{1/2}$ hfs and the Breit-Rabi diagrams for the $2S_{1/2}$ and $2P_{1/2}$ states, this is the aim of the experiment presented in this thesis for the first time. The results of the hfs, used to calculate the Breit-Rabi diagrams of sec. 2.2, are shown in table 2.3.

The second approach to theoretically handle the hfs is the D_{21} theory which is described in detail in [Kar02b, Kar02a, Kar03]. The D_{21} theory is a precise theory of the specific difference $D_{21} = 8f_{hfs}(2S_{1/2}) - 1f_{hfs}(1S_{1/2})$ as already mentioned in the introduction. It is not the aim of this theory to calculate absolute values for the hfs but rather to test BSQED in calculating this difference precisely and compare it with recent measurements. As already described above in the first approach to hfs calculations, nuclear structure effects influence the hfs values. Measured values of the hfs automatically include the influence of the nucleus, i.e. this influence cannot be switched off during the experiment to compare it with pure BSQED calculations which do not contain nuclear structure contributions, because they are simply not known precisely enough. By building the difference D_{21} , leading order nuclear structure effects vanish which can be understood as follows. In the non-relativistic approximation, the hfs of a $nS_{1/2}$ state reads as

$$\begin{aligned} \Delta E_{hfs}^{(nS_{1/2})} &= \frac{E_F}{n^3} \quad \text{with} \\ \frac{E_F}{h} &= \frac{8}{3} Z^3 \alpha^2 c \text{Ry} \frac{\mu_I}{\mu_B} \frac{2I+1}{2I} \left(\frac{M}{m_e + M} \right)^3, \end{aligned} \quad (2.28)$$

where E_F denotes the Fermi energy, Ry is the Rydberg constant and h is the Planck constant. The result of QED calculations to determine the $nS_{1/2}$ hfs is now written as

$$\Delta E_{hfs,QED}^{(nS_{1/2})} = \frac{E_F}{n^3} (1 + Q_{QED}(nS_{1/2})) \quad , \quad (2.29)$$

where $Q_{QED}(nS_{1/2})$ is the QED correction to the hfs for a $nS_{1/2}$ state [Kar02b]. Furthermore, as already described, nuclear structure effects have an influence on the atomic energy levels and, therefore, to eq. 2.29 an energy correction has to be added. In this second approach to the hfs, this correction (in leading order) is written in another way as described previously [Kar02b, Kar02a]:

$$\begin{aligned} \Delta E_{hfs,Nucl} &= A_{Nucl} |\psi_{nl}(\mathbf{r} = 0)|^2 \quad \text{with} \\ |\psi_{nl}(\mathbf{r} = 0)|^2 &= \frac{(Z\alpha)^3 \mu^3 c^3}{\pi n^3 \hbar^3} \delta_{0l} \quad , \end{aligned} \quad (2.30)$$

where $\psi_{nl}(\mathbf{r} = 0)$ is proportional to the Schrödinger wave function at the origin. The n^{-3} scaling can already be seen by looking at the radial wave functions presented in table 2.1 of subsec. 2.1.1. A_{Nucl} is a nuclear parameter which does not depend on the atomic state $|n, l\rangle$ and contains the nuclear effect to the energy levels. An easy way to determine this nuclear parameter is a comparison between the measured $1S_{1/2}$ hfs and the pure QED calculation of the same quantity. In table 2.4, experimental values

Table 2.4: $nS_{1/2}$ hyperfine structure up to $n = 2$ in hydrogen and deuterium. Comparison between recent experimental data and pure QED calculations to determine the nuclear contribution $\Delta E_{hfs,Nucl}$ to the hyperfine structure. The attention should be directed to the n^{-3} scaling of $\Delta E_{hfs,Nucl}$ which is the experimental proof of the atomic-state independence of the nuclear parameter A_{Nucl} .

Atom	$\Delta E_{hfs,exp}^{(nS_{1/2})}$ [kHz]	$\Delta E_{hfs,QED}^{(nS_{1/2})}$ [kHz]	$\Delta E_{hfs,Nucl}$ [kHz]
$^1H, n = 1$	1420 405.751 7667(9) [Ram93]	1420 452 [Kar02b, Kar02a, Kar03]	-46
$^2H, n = 1$	327 384.352 5222(17) [Win72]	327 339 [Kar02b, Kar02a, Kar03]	45
$^1H, n = 2$	177 556.860(16) [Kol04b]	177 562.7 [Kar02b, Kar02a, Kar03]	-5.8
$^2H, n = 2$	40 924.454(7) [Kol04a]	40 918.81 [Kar02b, Kar02a, Kar03]	5.6

Table 2.5: Most recent theoretical and experimental values for the specific difference D_{21} in hydrogen and deuterium.

Atom	D_{21}^{exp} [kHz]	D_{21}^{theo} [kHz]	D_{21}^{QED} [kHz]	D_{21}^{Nucl} [kHz]
1H	49.13(12) [Kol04b, Ram93]	48.953(3) [Kar02b, Kar02a, Kar03]	48.955(3)	-0.002
2H	11.280(56) [Kol04a, Win72]	11.312 5(5) [Kar02b, Kar02a, Kar03]	11.309 9(5)	0.002 6(2)

of the $1S_{1/2}$ and the $2S_{1/2}$ hfs are compared with pure QED calculations obtained from eq. 2.29. The difference between the experimental and the QED value is the nuclear contribution to the hfs (eq. 2.30). It is obvious, that the energy correction $\Delta E_{hfs,Nucl}$ vanishes in the difference D_{21} which can easily be checked by calculating D_{21} only for $\psi_{nl}(\mathbf{r} = 0)$, i.e. $8\psi_{20}(\mathbf{r} = 0) - 1\psi_{10}(\mathbf{r} = 0)$. This means, as already stated, leading order nuclear effects do not appear in the specific difference D_{21} . However, there are residual higher-order nuclear effects which have to be taken into account to obtain a reliable value for D_{21} . The pure QED approach to D_{21} yields the value D_{21}^{QED} which is shown

in table 2.5 for hydrogen and deuterium. Including nuclear effects, another value can be obtained shown in the same table and denoted with the symbol D_{21}^{Nucl} . Adding this value to D_{21}^{QED} gives the theoretical value of D_{21} , denoted with the symbol D_{21}^{theo} . The important formulas for the calculation can be reviewed in [Kar02b, Kar02a, Kar03]. Although nuclear structure effects are a big unknown in QED calculations, with the assumptions of the proton and the deuteron properties contributing to the difference D_{21} , precise values can be obtained which coincide very well with the experimental results as can be seen in table 2.5. For the hydrogen and the deuterium atom there are two different effects, dominating the nuclear structure correction for D_{21} . In leading order, for the hydrogen atom this is the FNS effect of the proton, while for the deuterium atom the nuclear polarizability effect, as described in the introduction of this thesis, is the dominating nuclear effect to the D_{21} theory. As already mentioned in the first approach to hfs calculations in this subsection, the deviation of the pointlike hyperfine constant to a hyperfine constant belonging to an extended nucleus can be described by including a charge and a magnetization distribution correction to the calculation. In higher-order considerations, nuclear effects contribute to the D_{21} theory and with the charge and magnetization distribution correction a nuclear charge and a magnetic radius can be assigned which has to be considered to obtain a reliable result for the theoretical value of D_{21} . In the specific difference D_{21} , this two radii do not contribute as strong as in absolute calculations of the hfs, nonetheless they do. The D_{21} theory is a very complex theory which cannot be described in detail in this subsection, however a rough idea what this theory is about was given.

2.2 Zeeman Effect of the Hyperfine Structure in ^1H and ^2H in the First Excited State - Precise Breit-Rabi Diagrams as a Result of QED Calculations

In the preceding section, the quantum theory of the hydrogen and the deuterium atom, respectively, was presented, excluding the influence of external electromagnetic fields on the energy levels of the atoms. The correction to the energy levels in these two atoms due to the influence of an external static homogeneous magnetic field \mathbf{B}_0 is presented in this section.

First of all, what happens generally to the hydrogen or deuterium energy levels when placing these two atoms in a magnetic field? For a full description, it has to be distinguished between a weak and a strong field. The external magnetic field is weak, if the potential energy of the atom in the field is small compared to the hfs for a given state, otherwise the field is strong.

A weak magnetic field, pointing in z direction, is considered. As shown in fig. 2.9, the total angular momentum of the atomic shell $\hat{\mathbf{J}}$ couples with the nuclear spin $\hat{\mathbf{I}}$ to the total angular momentum of the atom $\hat{\mathbf{F}}$.

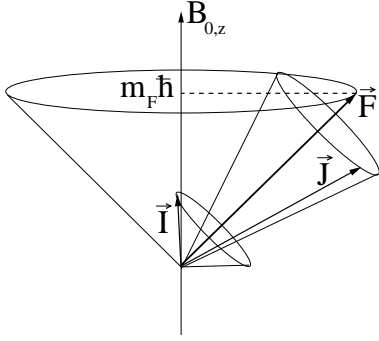


Figure 2.12: Vector diagram to illustrate the Zeeman effect of the hfs in a weak magnetic field.

In a weak magnetic field this coupling is preserved, i.e. F is a valid quantum number. The total angular momentum vector of the atom \vec{F} precesses around the magnetic-field direction $B_{0,z}$. \vec{J} and \vec{I} , respectively, precess around \vec{F} (fig. 2.12). The precession frequency of \vec{F} is slow while the motion of \vec{J} and \vec{I} around the total angular momentum of the atom is fast. The magnetic moment of \vec{F} is $\vec{\mu}_F = \vec{\mu}_j + \vec{\mu}_I$, which is the sum of the magnetic moment of the atomic shell $\vec{\mu}_j$ and the magnetic moment of the nuclear spin $\vec{\mu}_I$. With the quantization axis z , $\vec{\mu}_F$ is

$$(\vec{\mu}_F)_z = -g_F \mu_B m_F \quad \text{and} \quad g_F = g_j \frac{F(F+1) - I(I+1) + j(j+1)}{2F(F+1)} - g_I \frac{\mu_N}{\mu_B} \frac{F(F+1) + I(I+1) - j(j+1)}{2F(F+1)}. \quad (2.31)$$

Here, g_F is the g factor of the total angular momentum of the atom, g_I is the g factor of the nuclear spin and m_F is the magnetic quantum number of the total angular momentum of the atom $\hat{\mathbf{F}}$, where $m_F = F, F-1, \dots, -F$ can have $2F+1$ values. These are the possible orientations of \vec{F} relative to $B_{0,z}$ as shown in fig. 2.12. A magnetic field, therefore, removes the degeneracy of hyperfine structure levels with $F > 0$. This is the Zeeman effect of the hfs. In a weak magnetic field the energy correction to the hfs is

$$\delta E_{hfs,mag} = -(\vec{\mu}_F)_z \cdot B_{0,z} = g_F \mu_B B_{0,z} m_F, \quad (2.32)$$

where the δ is used to express a correction to the hyperfine energy levels with different magnetic quantum number m_F , i.e. to the single Zeeman components of the hfs, due to an external magnetic field. The meaning of eq. 2.32 is, that in a weak magnetic field the energy correction is linear. Hydrogen atomic levels with $m_F = 0$ (mixed states), i.e. states with antiparallel nuclear spin and electron spin, have not to be corrected in a weak magnetic field, because $\delta E_{hfs,mag}$ is zero in this case.

In a strong magnetic field, there is no coupling of the angular momenta \vec{J} and \vec{I} to the total angular momentum of the atom \vec{F} , i.e. the F quantum number is no longer defined (Paschen-Back effect). Spin-orbit coupling, which is due to the huge electron

magnetic moment compared to the 1836-times weaker nuclear magnetic moment a much more stronger coupling than the coupling of \vec{J} and \vec{I} to \vec{F} , is preserved as long as the strength of the external magnetic field does not exceed the magnetic-field strength produced by the electron motion leading to a coupling of \vec{L} and \vec{S} to \vec{J} . Decoupling of \vec{L} and \vec{S} is only possible in a very strong magnetic field in the order of a few Tesla, but in this case the same apply to \vec{L} and \vec{S} like now described for \vec{J} and \vec{I} .

If, in a strong magnetic field, there is no coupling between \vec{J} and \vec{I} , \vec{J} precesses around the external magnetic field in z direction like illustrated in fig. 2.13. The nuclear spin and its magnetic moment, respectively, senses mainly the magnetic field \mathbf{B}_J produced by the electron motion because in general it is stronger (10 – 100 T) than the external magnetic field. Therefore, \vec{I} precesses around \vec{J} . Meanwhile, \vec{J} precesses with a high angular frequency around the magnetic-field direction $B_{0,z}$, so \vec{I} senses a constant mean field $B_{J,z}$ pointing in the direction of $B_{0,z}$ and causing \vec{I} to also point in direction of $B_{0,z}$ (fig. 2.13).

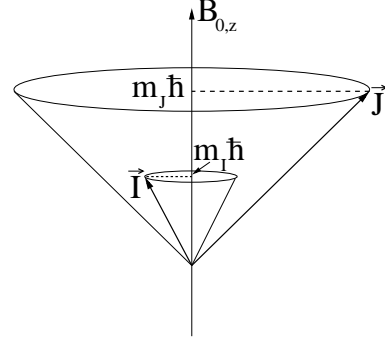


Figure 2.13: Vector diagram to illustrate the Paschen-Back effect of the hfs. The F quantum number is no longer defined.

The z component of the total angular momentum of the atomic shell and the nuclear spin can have values $m_J \hbar$ and $m_I \hbar$ where m_J is $J, J - 1 \dots - J$ and m_I is $I, I - 1 \dots - I$. In the strong field case, the energy correction to the hfs due to the external magnetic field depends on three terms and the correction is

$$\delta E_{hfs,mag} = g_j \mu_B m_j B_{0,z} + a_{pt}^{(nl_j)} m_I m_j - g_I \mu_N m_I B_{0,z} \quad , \quad (2.33)$$

where the first term is the contribution of the atomic shell to the energy correction, i.e. the Zeeman effect of the fine structure. The second term is the hyperfine-interaction energy between electron and nucleus, i.e. the nuclear spin is considered, so the Zeeman effect of the fine structure splits up in $2I + 1$ hyperfine levels according to the possible values of m_I . The last term is the Zeeman energy of the nucleus which cannot be neglected in increasing magnetic fields. For a first approximation how the conceptual idea of the energy correction to the hyperfine levels looks like, the pointlike hyperfine constant was chosen.

In general, the transition from the weak field to the strong field case in an atom is very difficult to calculate and in the most cases only an approximate solution for the correction of the atomic binding energy in intermediate magnetic fields can be obtained.

Compared with this, in atoms with $F = I \pm 1/2$, the Breit-Rabi formula allows to obtain an overall solution for the dependence of the atomic binding energy on an external magnetic field. This means, that there exists a formula which describes the dependence of the atomic binding energy in an external magnetic field of up to a certain field strength. The Breit-Rabi formula is applicable to the hydrogen and the deuterium atom for states with $j = 1/2$ and the most recent formula for the first excited state is presented in the next subsection and compared to the conventional Breit-Rabi formula [Bre31]. As a main difference to the conventional theory, the recent Breit-Rabi formula was developed by [Mos06] in a fully relativistic framework. Furthermore, the g_j factor of the bound electron was calculated with modern methods of BSQED. In contrast to that, Breit and Rabi [Bre31] suggested to choose a value of 2 for the electron g factor, i.e. a value calculable with eq. 2.15, which can be obtained from the Dirac theory without binding corrections. This seems to be a little bit strange, because Breit knew already 3 years before, when he published the paper “The Magnetic Moment of the Electron” [Bre28], that the g factor of the electron bound in a hydrogenlike atom differs from the value of 2 because of binding corrections to the Dirac theory. However, besides the Breit-Rabi formulas and the Breit-Rabi diagrams, respectively, to be presented for hydrogen and deuterium, the whole contribution to the g_j factor is also summarized below.

2.2.1 The Breit-Rabi Formula for the Hydrogen and Deuterium Atom

As described in the preceding section, the Breit-Rabi formula covers the description of the atomic binding energy both as function of a weak magnetic field and as function of a strong magnetic field, including the intermediate magnetic-field region. As a basis for this subsection [Mos06, Mos07a] is taken. For the first excited state in hydrogen and deuterium, the conventional Breit-Rabi formula [Bre31] is

$$\delta E_{hfs, mag}(x) = \Delta E_{hfs}^{(2l_{1/2})} \left[a_1 m_F x \pm \frac{1}{2} \sqrt{1 + \frac{4m_F}{2I+1} c_1 x + c_2 x^2} \right] - \frac{\Delta E_{hfs}^{(2l_{1/2})}}{2(2I+1)} \quad , \quad (2.34)$$

where $x = \mu_B B_{0,z} / \Delta E_{hfs}^{(2l_{1/2})}$ and the energy $\delta E_{hfs, mag}(x)$ is counted from the hyperfine centroid which is taken into consideration by the last term. Compared to the formula in the original paper [Bre31], the coefficients in eq. 2.34 were modified as preparation for the modern handling of the Breit-Rabi formula. They are

$$a_1 = -g'_I \quad , \quad (2.35a)$$

$$c_1 = g_j + g'_I \quad , \quad (2.35b)$$

$$c_2 = (g_j + g'_I)^2 \quad . \quad (2.35c)$$

Here g_j is the bound electron g factor

$$g_j = g_D + \Delta g_{QED} + \Delta g_{rec}^{(e)} + \Delta g_{NS} + \Delta g_{NP} \quad . \quad (2.36)$$

In this equation g_D is the bound electron g factor derived from the Dirac equation with binding corrections [Bre28]

$$g_D = \frac{\kappa}{j(j+1)} \left(\kappa \frac{E_{n\kappa}}{m_e c^2} - \frac{1}{2} \right) \quad \text{with} \quad (2.37)$$

$$E_{n\kappa} = \frac{\gamma + n_r}{N} m_e c^2 \quad ,$$

where $E_{n\kappa}$ is another notation for the Dirac energy, n is the principal quantum number, $\kappa = (-1)^{j+l+1/2}(j+1/2)$, $n_r = n - |\kappa|$ is the radial quantum number, $\gamma = \sqrt{\kappa^2 - (\alpha Z)^2}$ and $N = \sqrt{n_r^2 + 2n_r\gamma + \kappa^2}$. Furthermore, Δg_{QED} is the QED correction to the bound electron g factor, $\Delta g_{rec}^{(e)}$ is the nuclear recoil correction, Δg_{NS} is the nuclear size correction and Δg_{NP} is the nuclear polarizability correction. For further information on the various contributions to the g_j factor, [Sha91, Bei00, Sha01, Gla02, Nef02, Sha02, Yer02, Mos04, Lee05, Pac05] should be taken as references. The primed g factor of the nucleon is an abbreviated term for the following expression

$$g'_I = \frac{m_e}{m_p} (g_I + \Delta g_{rec}^{(n)}) \quad , \quad (2.38)$$

where $\Delta g_{rec}^{(n)} \approx 10^{-11}$ denotes the recoil correction to the bound nucleus g factor which can be neglected due to its small influence.

Applying the Breit-Rabi formula 2.34 to the hydrogen and the deuterium atom, special cases of this formula can be obtained. For $j = 1/2$, there are only two hfs levels $F = I - 1/2$ and $F' = I + 1/2$ with the same $m_F = -I + 1/2 \dots I - 1/2$ which simplifies the theoretical treatment of the Breit-Rabi formula for hydrogen and deuterium.

For $F' = I + 1/2$ and $m_F = \pm (I + 1/2)$ the splitting of the Zeeman components in hydrogen and deuterium is linear in a magnetic field with arbitrary strength

$$\delta E_{hfs,mag}(x) = \Delta E_{hfs}^{(2l_1/2)} \left[\frac{1}{2} \pm d_1 x \right] - \frac{\Delta E_{hfs}^{(2l_1/2)}}{2(2I + 1)} \quad , \quad (2.39)$$

where $d_1 = 1/2g_j - Ig'_I$ and the “ \pm ” sign refers to $m_F = \pm (I + 1/2)$ respectively. Especially for the hydrogen atom $F = 0$ and $F' = 1$ and for the two mixed Zeeman

components with $m_F = 0$ the Breit-Rabi formula can be written as

$$\delta E_{mag,hfs}(x) = \pm \frac{\Delta E_{hfs}^{(2l_{1/2})}}{2} \sqrt{1 + c_2 x^2} - \frac{\Delta E_{hfs}^{(2l_{1/2})}}{2(2I + 1)} \quad , \quad (2.40)$$

where the “−” sign refers to $F = 0$ and the “+” sign refers to $F' = 1$. The dependence of the mixed states in deuterium on the external magnetic field can be described by eq. 2.34. Although the Breit-Rabi formula as presented above holds for every sort of atom in a state with $j = 1/2$, it is obvious that corrections for different nuclei are missing. Eq. 2.34 can be taken to plot the Breit-Rabi diagrams for hydrogen and deuterium by substituting the associated coefficients, but higher order corrections are missing. To include these, the matrix elements of an operator have to be calculated which includes a magnetic dipole and an electric quadrupole operator, and an operator which describes the interaction of the atom with an external magnetic field. By considering an electric quadrupole operator, electric quadrupole moments of nuclei with $I \geq 1$, such as the deuteron, are taken into account and this is added to the energy levels in an external magnetic field, described by the Breit-Rabi formula. For nuclei with $I = 1/2$, such as the proton, the influence of the electric quadrupole operator has to vanish. The operator \hat{V} which includes the just mentioned operators to calculate an individual Breit-Rabi formula for a certain atom can be written as $\hat{V} = \hat{V}_{hfs} + \hat{V}_{\mathbf{B}}$. Here $\hat{V}_{hfs} = \hat{V}_{hfs}^{(\mu)} + \hat{V}_{hfs}^{(Q)}$ is the hyperfine interaction operator consisting of $\hat{V}_{hfs}^{(\mu)}$, the magnetic dipole hyperfine interaction operator, and $\hat{V}_{hfs}^{(Q)}$, the electric quadrupole hyperfine interaction operator. The second term $\hat{V}_{\mathbf{B}} = \hat{V}_{\mathbf{B}}^{(e)} + \hat{V}_{\mathbf{B}}^{(n)}$ describes the interaction of the atom with the external magnetic field and consists of the interaction of the electron $\hat{V}_{\mathbf{B}}^{(e)}$ and the nucleon $\hat{V}_{\mathbf{B}}^{(n)}$ with the external magnetic field. In the vector picture, in particular, the operators are:

$$\vec{V}_{hfs}^{(\mu)} = \frac{|e|}{4\pi} \frac{(\vec{\alpha} \cdot [\vec{\mu}_I \times \mathbf{r}])}{r^3} \quad , \quad (2.41a)$$

$$V_{hfs}^{(Q)} = -\alpha \sum_{m=-2}^2 Q_{2m} \eta_{2m}(\mathbf{n}) \quad , \quad (2.41b)$$

$$\vec{V}_{\mathbf{B}}^{(e)} = -e (\vec{\alpha} \cdot \mathbf{A}) = \frac{|e|}{2} (\vec{\alpha} \cdot [\mathbf{B} \times \mathbf{r}]) \quad \text{and} \quad (2.41c)$$

$$V_{\mathbf{B}}^{(n)} = -\vec{\mu}_I \cdot \mathbf{B} \quad , \quad (2.41d)$$

where $\vec{\alpha}$ is a vector¹⁷ consisting of the Dirac matrices, \mathbf{A} is the vector potential,

¹⁷As already mentioned, operators in the vector picture are tagged with a “vector arrow”. However, vectors are written as bold symbols like usual.

$Q_{2m} = \sum_{i=1}^Z \mathbf{r}_i^2 C_{2m}(\mathbf{n}_i)$ is the electric quadrupole moment of the nucleus and $\mathbf{n}_i = \mathbf{r}_i/r_i$ is a normalized vector where \mathbf{r}_i is the position vector of the i th proton of the nucleus. $\eta_{2m} = C_{2m}(\mathbf{n})/r^3$ acts only on electron variables where $\mathbf{n} = \mathbf{r}/r$, with the position vector of the electron \mathbf{r} and $C_{lm} = \sqrt{4\pi/(2l+1)}Y_l^m$ where Y_l^m is a spherical harmonic.

The unperturbed atomic eigenstates $|n, l, j, I, F, m_F\rangle$ of the $2S_{1/2}$ and $2P_{1/2}$ state, respectively, in hydrogen and deuterium form a two-dimensional subspace according to states with $F = I - 1/2$ and $F' = I + 1/2$. Expanding the unperturbed atomic eigenstates into the $\{|n, l, j, m_j\rangle |I, m_I\rangle\}$ basis

$$|n, l, j, I, F, m_F\rangle = \sum_{m_j, m_I} C_{jm_jIm_I}^{Fm_F} |n, l, j, m_j\rangle |I, m_I\rangle \quad ,$$

the perturbation of single Zeeman components of the hfs due to the external magnetic field can be calculated and a closed solution can be obtained appropriate for weak magnetic fields, an intermediate field region and for strong magnetic fields. Here $|n, l, j, m_j\rangle$ are unperturbed electron eigenstates which are in a certain basis four-component eigenvectors of the Dirac equation in a Coulomb field, $|I, m_I\rangle$ are nuclear eigenstates and $C_{jm_jIm_I}^{Fm_F}$ are the Clebsch-Gordan coefficients. Following this strategy, a very precise Breit-Rabi formula can be obtained [Mos06]

$$\begin{aligned} \delta E_{hfs, mag}(x) = \Delta E_{hfs}^{(2l_{1/2})} & \left[a_1(1 + \epsilon_1)m_F x + \epsilon_2 \frac{\Delta E_{hfs}^{(2l_{1/2})}}{m_e c^2} x^2 \right. \\ & \left. \pm \frac{1}{2} \sqrt{1 + \frac{4m_F}{2I+1} c_1(1 + \delta_1)x + c_2(1 + \delta_2 + m_F^2 \delta_3)x^2} \right] - \frac{\Delta E_{hfs}^{(2l_{1/2})}}{2(2I+1)} \quad , \quad (2.42) \end{aligned}$$

in contrast to eq. 2.34. Eqs. 2.39 and 2.40 change into following equations

$$\delta E_{hfs, mag}(x) = \Delta E_{hfs}^{(2l_{1/2})} \left[\frac{1}{2} \pm d_1(1 + \eta_1)x + \eta_2 \frac{\Delta E_{hfs}^{(2l_{1/2})}}{m_e c^2} x^2 \right] - \frac{\Delta E_{hfs}^{(2l_{1/2})}}{2(2I+1)} \quad , \quad (2.43a)$$

$$\delta E_{hfs, mag}(x) = \Delta E_{hfs}^{2l_{1/2}} \left[\epsilon_2 \frac{\Delta E_{hfs}^{(2l_{1/2})}}{m_e c^2} x^2 \pm \frac{1}{2} \sqrt{1 + c_2(1 + \delta_2)x^2} \right] - \frac{\Delta E_{hfs}^{(2l_{1/2})}}{2(2I+1)} \quad . \quad (2.43b)$$

The coefficients for the Breit-Rabi formulas 2.42, 2.43a and 2.43b for the $2S_{1/2}$ and the $2P_{1/2}$ state in hydrogen and deuterium were calculated by Dmitriy Moskovkin (calculation of the Breit-Rabi formula and the coefficients [Mos06, Mos07a]) and Dmitry Glazov (calculation of the coefficients and the bound electron g factor [Mos07a]) from the group of Vladimir Shabaev, Division of Quantum Mechanics, Department of Physics, Saint-Petersburg State University. This is the presently most recent Breit-Rabi formula. All

Table 2.6: Critical magnetic-field strength for hydrogen and deuterium in the first excited state with $j = \frac{1}{2}$.

Atom	B_C [G]	
	$2S_{1/2}$	$2P_{1/2}$
Hydrogen	63.42	21.15
Deuterium	14.62	4.87

coefficients can be looked up in table A.1 of app. A. The meaning of the particular coefficients cannot be discussed in all detail and further informations should be gained from [Mos06]. Comparing the conventional Breit-Rabi formula with the most recent one, it can be noticed that the basic mathematical structure is conserved and the recent formula is complemented by several coefficients. The δ_3 coefficient for example is a single term which depends on the electric quadrupole moment of the nucleus. As can be seen, for hydrogen this coefficient vanishes which is due to the vanishing electric quadrupole moment for a spin 1/2 nucleus as already mentioned. The same is valid for ϵ_1 , too. Although in figs. 2.14 and 2.15, respectively, only the recent Breit-Rabi diagrams for hydrogen and deuterium are presented (plotted with eqs. 2.42, 2.43a and 2.43b using the coefficients from table A.1), the most obvious difference to diagrams obtained with the conventional eqs. 2.34, 2.39 and 2.40 should be emphasized below. The Zeeman components of the hfs in the Breit-Rabi diagrams are characterized with a special notation which should be briefly introduced. In the hydrogen case for the $2S_{1/2}$ state, the Zeeman components are labeled with the letters α_1 , α_2 , β_3 and β_4 and for the $2P_{1/2}$ state with the letters e_1 , e_2 , f_3 and f_4 . Using the example of the $2S_{1/2}$ state, in particular the letters represent the following quantum mechanical states

$$\begin{aligned}
\alpha_1 &\hat{=} |F = 1, m_F = 1\rangle = |m_j = 1/2, m_I = 1/2\rangle \quad , \\
\alpha_2 &\hat{=} |1, 0\rangle = 1/\sqrt{2} \left[\sqrt{1 + a(B_{0,z})} |1/2, -1/2\rangle + \sqrt{1 - a(B_{0,z})} |-1/2, 1/2\rangle \right] \quad , \\
\beta_3 &\hat{=} |1, -1\rangle = |-1/2, -1/2\rangle \quad , \\
\beta_4 &\hat{=} |0, 0\rangle = 1/\sqrt{2} \left[\sqrt{1 - a(B_{0,z})} |1/2, -1/2\rangle - \sqrt{1 + a(B_{0,z})} |-1/2, 1/2\rangle \right] \quad .
\end{aligned} \tag{2.44}$$

The same is applicable for the $2P_{1/2}$ state by replacing α_1 , α_2 , β_3 and β_4 with e_1 , e_2 , f_3 and f_4 and by substituting the corresponding critical field parameter $a(B_{0,z})$ which

is given by

$$a(B_{0,z}) = \frac{\frac{B_{0,z}}{B_C}}{\sqrt{1 + \left(\frac{B_{0,z}}{B_C}\right)^2}} \quad . \quad (2.45)$$

The critical magnetic-field strength B_C can be calculated for every state, i.e. $2S_{1/2}$ or $2P_{1/2}$, by the relation $B_C = \Delta E_{hfs}^{(2l_{1/2})}/2\mu_B$. This relation can be derived by setting the term xc_1 , which was introduced in this subsection, equal to “1” and solve for $B_{0,z}$. With the assumption that g_I' is small, the critical field strength for the $2S_{1/2}$ and the $2P_{1/2}$ state can be obtained (table 2.6). If $B_{0,z} \ll B_C$, then $B_{0,z}$ is defined as a weak magnetic field, if $B_{0,z} \gg B_C$, then $B_{0,z}$ is defined as a strong magnetic field. In the case of the deuterium $2S_{1/2}$ state, following relations are valid for α_1 , α_2 , α_3 , β_4 , β_5 and β_6

$$\begin{aligned} \alpha_1 &\hat{=} |F = 3/2, m_F = 3/2\rangle = |m_j = 1/2, m_I = 1\rangle \quad , \\ \alpha_2 &\hat{=} |3/2, 1/2\rangle = 1/\sqrt{2} \left[\sqrt{1 + a(B_{0,z})} |1/2, 0\rangle + \sqrt{1 - a(B_{0,z})} |-1/2, 1\rangle \right] \quad , \\ \alpha_3 &\hat{=} |3/2, -1/2\rangle = 1/\sqrt{2} \left[\sqrt{1 - b(B_{0,z})} |-1/2, 0\rangle + \sqrt{1 + b(B_{0,z})} |1/2, -1\rangle \right] \quad , \\ \beta_4 &\hat{=} |3/2, -3/2\rangle = |-1/2, -1\rangle \quad , \\ \beta_5 &\hat{=} |1/2, -1/2\rangle = 1/\sqrt{2} \left[\sqrt{1 + b(B_{0,z})} |-1/2, 0\rangle - \sqrt{1 - b(B_{0,z})} |1/2, -1\rangle \right] \quad , \\ \beta_6 &\hat{=} |1/2, 1/2\rangle = 1/\sqrt{2} \left[\sqrt{1 + a(B_{0,z})} |-1/2, 1\rangle - \sqrt{1 - a(B_{0,z})} |1/2, 0\rangle \right] \quad , \end{aligned} \quad (2.46)$$

with the critical field parameters

$$a(B_{0,z}) = \frac{\frac{B_{0,z}}{B_C} + \frac{1}{3}}{\sqrt{1 + \frac{2}{3} \frac{B_{0,z}}{B_C} + \left(\frac{B_{0,z}}{B_C}\right)^2}} \quad \text{and} \quad b(B_{0,z}) = \frac{\frac{B_{0,z}}{B_C} - \frac{1}{3}}{\sqrt{1 - \frac{2}{3} \frac{B_{0,z}}{B_C} + \left(\frac{B_{0,z}}{B_C}\right)^2}} \quad . \quad (2.47)$$

Like in the case of the hydrogen atom, the same relations hold for the deuterium $2P_{1/2}$ state with proper substitutions. As described in [Lam51] and in the corresponding paper series of Lamb and Retherford, the intersection of the Zeeman components of the $2S_{1/2}$ state with the components of the $2P_{1/2}$ state in hydrogen and deuterium is well-known. Following Lamb, in hydrogen the intersection of β_3 with e_2 is approximately at $B = 605$ G while the intersection of β_4 with e_1 is at $B = 538$ G. Furthermore, for deuterium the intersection of β_4 with e_3 can be found approximately at $B = 585$ G while the intersection of β_5 with e_2 is at $B = 575$ G and the intersection of β_6 with

Table 2.7: Intersection points of the Zeeman components of hydrogen and deuterium obtained from the recent Breit-Rabi formulas compared to intersection points obtained from the conventional Breit-Rabi formulas. As a reference, the experiment of Lamb is taken [Lam51].

Hydrogen			
Intersection	Recent Formula	Conventional Formula	Lamb's Experiment
β_3 with e_2	605.41 G	597.49 G	≈ 605 G
β_4 with e_1	538.21 G	532.10 G	≈ 538 G
Deuterium			
Intersection	Recent Formula	Conventional Formula	Lamb's experiment
β_4 with e_3	584.29 G	576.99 G	≈ 585 G
β_5 with e_2	574.14 G	567.12 G	≈ 575 G
β_6 with e_1	564.17 G	557.42 G	≈ 565 G

e_1 can be found at $B = 565$ G. In table 2.7 the differences of the intersection points in diagrams obtained from the eqs. 2.34, 2.39 and 2.40 to diagrams obtained with the most recent Breit-Rabi formulas are compared. The recent theory is much closer to the experimental results than the conventional Breit-Rabi formulas. This is an obvious difference, so the recent theory of the Zeeman effect should be taken as a basis for the spectroscopy experiment presented in this thesis and the conventional Breit-Rabi formulas should not be used.

2.2.2 Breit-Rabi Diagram of the Hydrogen Atom

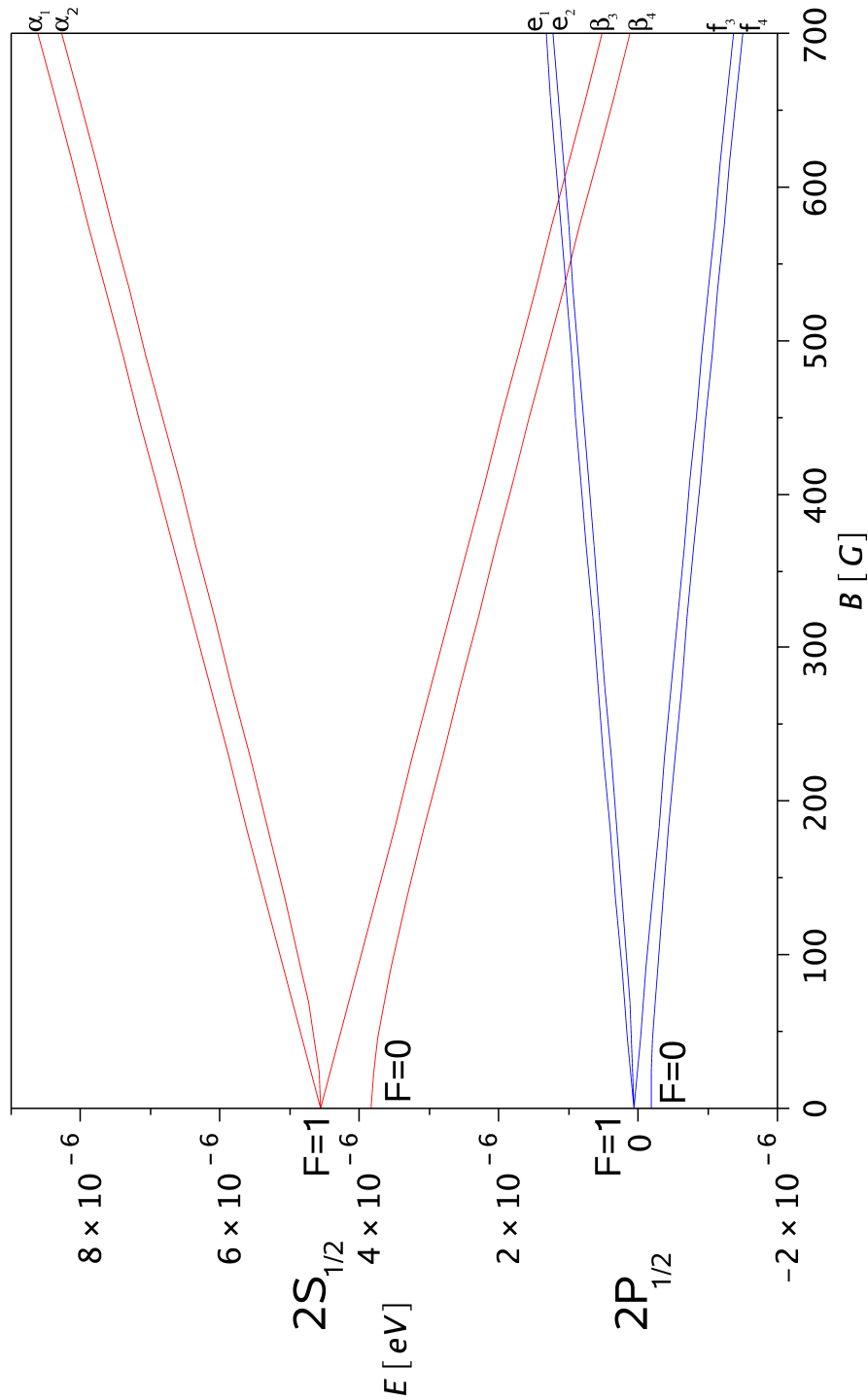


Figure 2.14: Breit-Rabi diagram of the hydrogen atom in the first excited state with $j = \frac{1}{2}$. At $B = 0$, the spacing between the centroid of the $2S_{1/2}$ state and the $2P_{1/2}$ state is the classical Lamb shift as exemplified in fig. 2.10. The zero point of the energy was chosen to be equal to the $2P_{1/2}$ centroid.

2.2.3 Breit-Rabi Diagram of the Deuterium Atom

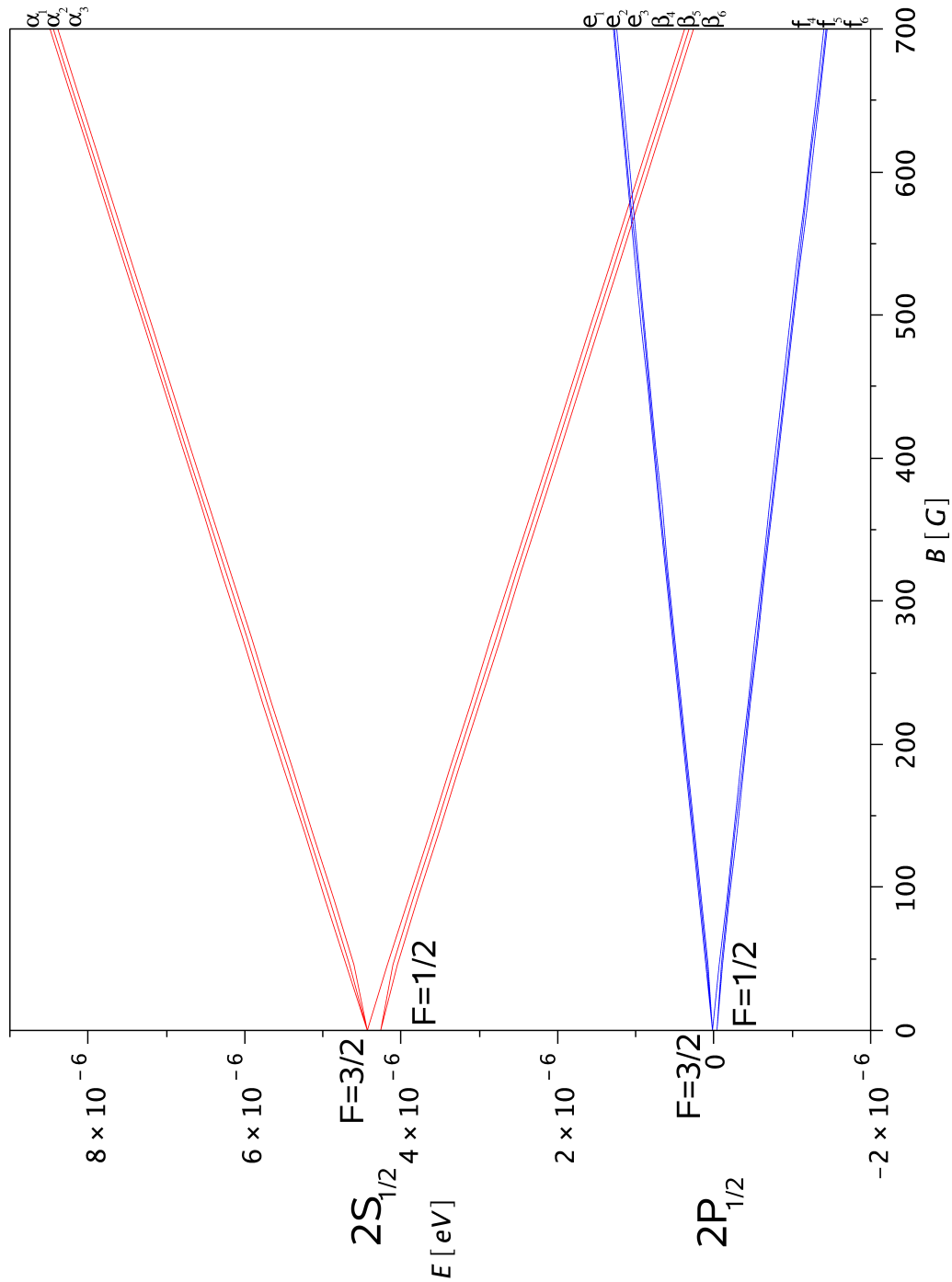


Figure 2.15: Breit-Rabi diagram of the deuterium atom in the first excited state with $j = \frac{1}{2}$. Due to the weaker nuclear magnetic moment of the deuteron compared to the proton, the hfs splitting in deuterium is smaller than in hydrogen and in order to that the crossing points of the hfs components are closer to each other than in the hydrogen case shown in fig. 2.14.

2.3 Interaction of an Atom with a Time-Dependent Electromagnetic Field

In this section, a brief determination of the selection rules of quantum mechanics for electric and magnetic dipole transitions between hyperfine structure states in hydrogen and deuterium are presented. They are the basis for the understanding of the measurements to be presented in the course of this thesis.

Placing an atom in a time-dependent electromagnetic field with a frequency f , atomic electrons in a state $|\iota\rangle$ can be excited to higher atomic states $|\zeta\rangle$ by absorption of a characteristic energy quantum hf of the radiation field which is equal to the energy separation of the two states $|\iota\rangle$ and $|\zeta\rangle$. Furthermore, excited atoms, i.e. with electrons in excited states $|\zeta'\rangle$, can be forced to do a transition into lower energy levels $|\iota'\rangle$ by emitting electromagnetic radiation with an energy hf' equal to the energy separation of the two states $|\zeta'\rangle$ and $|\iota'\rangle$. In addition to this, in absence of a time-dependent electromagnetic field, excited atoms can spontaneously undergo a transition into lower energy levels. Atomic processes of this kind are described with the Einstein coefficients of absorption and induced or spontaneous emission, respectively. From a naive point of view, arguing only with the energy conservation law, atomic transitions are completely described. Obviously, from experimental observations of atomic spectra, not every atomic transition fulfilling the energy conservation law occurs. This leads to the assumption that atomic transitions are subject to a selective mechanism in the atom itself, obeying the “selection rules”.

The selection rules can be determined by calculation of the non-vanishing terms of the matrix element $\langle \gamma, j, I, F, m_F | Q_{1q} | \gamma', j', I, F', m_{F'} \rangle$ where γ is a quantum number which contains all quantum numbers not important for the calculation of the matrix element. Non-vanishing matrix elements have to fulfill specific rules, the selection rules. Here, Q_{1q} is a placeholder for the electric and the magnetic dipole operator of the atom, respectively. Performing the calculation of the matrix element, the $3j$ symbol $\begin{pmatrix} F & 1 & F' \\ -m_F & q & m_{F'} \end{pmatrix}$ can be determined which provides a direct access to the selection rules. For a transition between the levels γj and $\gamma' j'$, the $3j$ symbol is only non-vanishing if $\Delta F = 0, \pm 1$ for $F + F' \geq 1$ and $\Delta m_F = 0, \pm 1$. Furthermore, the parity selection rule has to be considered. The electric dipole operator for an one-electron atom can be written as $-\mathbf{er}$. The vector \mathbf{r} , like every polar vector, changes its sign in an inversion transformation and, therefore, electric dipole transitions only occur between states with different parity. Therefore, the parity selection rule for electric dipole transitions reads as $(-1)^\kappa$ where $\kappa = 1$ for a dipole operator. For the magnetic dipole operator, the same selection rules can be obtained, while the parity selection

rule can be written as $-(-1)^\kappa$, where again $\kappa = 1$ for the dipole operator. So, magnetic dipole transitions occur between states with the same parity. In a strong magnetic field, the F quantum number is not preserved. For an electric dipole transition, the selection rules change into $\Delta m_I = 0$ and $\Delta m_j = 0, \pm 1$ while for magnetic dipole transitions in the strong field case the selection rules are $\Delta m_I = 0$ and $\Delta m_j = \pm 1$ or $\Delta m_I = \pm 1$ and $\Delta m_j = 0$.

If the atom is placed in an external magnetic field \mathbf{B}_0 , the m degeneracy (neglecting the subscript F and I or j , respectively, because the consideration is valid for both a weak and a strong field) of the atom is removed. Perpendicular to the external magnetic field, different linear polarized Zeeman components can be observed. For electric and magnetic dipole transitions on one hand these are components belonging to transitions with $\Delta m = 0$ which can be assigned to electric and magnetic dipole radiation, respectively, with the electric or magnetic field vector parallel to the external magnetic field. On the other hand transitions can be observed belonging to $\Delta m = \pm 1$ which can be assigned to dipole radiation with the corresponding field vector perpendicular to the external magnetic field. According to [Kus40], the following convention should be introduced. In the case of electric dipole radiation, transitions corresponding to $\Delta m = 0$ are called π transitions while transitions corresponding to $\Delta m = \pm 1$ are called σ transitions. Although it would be consequential to characterize magnetic dipole transitions with the same nomenclature, they are characterized with the nomenclature opposite to the usual assignment like mentioned in [Kus40]. I.e. in the case of magnetic dipole transitions, transitions corresponding to $\Delta m = 0$ are called σ transitions while transitions corresponding to $\Delta m = \pm 1$ are called π transitions. Due to the symmetry of the Einstein coefficients and according to the selection rules presented above, placing an atom in an electromagnetic field with frequency f (with dominating electric¹⁸ and magnetic components, respectively) which is surrounded by a well defined external magnetic field, selected atomic transitions can be induced dependent on the direction of the electromagnetic-field vector relative to the external magnetic field (figs. 2.16 - 2.17). Although in a vanishing magnetic field, transitions between hyperfine structure components differ in the strength according to the sum rules of atomic hyperfine structure transitions¹⁹, something similar is not expected for transitions between Zeeman components. However, placing an atom in a homogeneous magnetic field, the magnetic-field strength itself has an influence on the line strength of a transi-

¹⁸Induced transitions in an electric field with frequency f are also due to the Stark effect explained in sec. 2.4.

¹⁹The sum rule of atomic hyperfine structure transitions states that the sum of the intensities of all lines of the transition $\gamma j \rightarrow \gamma' j'$ originating from the component F of the level γj is proportional to the statistical weight of this component and, therefore, proportional to $2F + 1$. Furthermore, it states that the sum of the intensities of all lines from a transition $\gamma j \rightarrow \gamma' j'$ ending in the component F' of the level $\gamma' j'$ is proportional to the statistical weight of this component.

tion as can be seen from eqs. 2.44 and 2.46, respectively. For increasing magnetic-field strength, the critical field parameter gets continuously larger until reaching the value “1”. As a consequence, transitions which can be observed in very small magnetic fields decrease in their intensity until they vanish completely while the line strength of other transitions is unaffected by increasing magnetic fields. A more detailed discussion of this can be found in sec. 3.3.

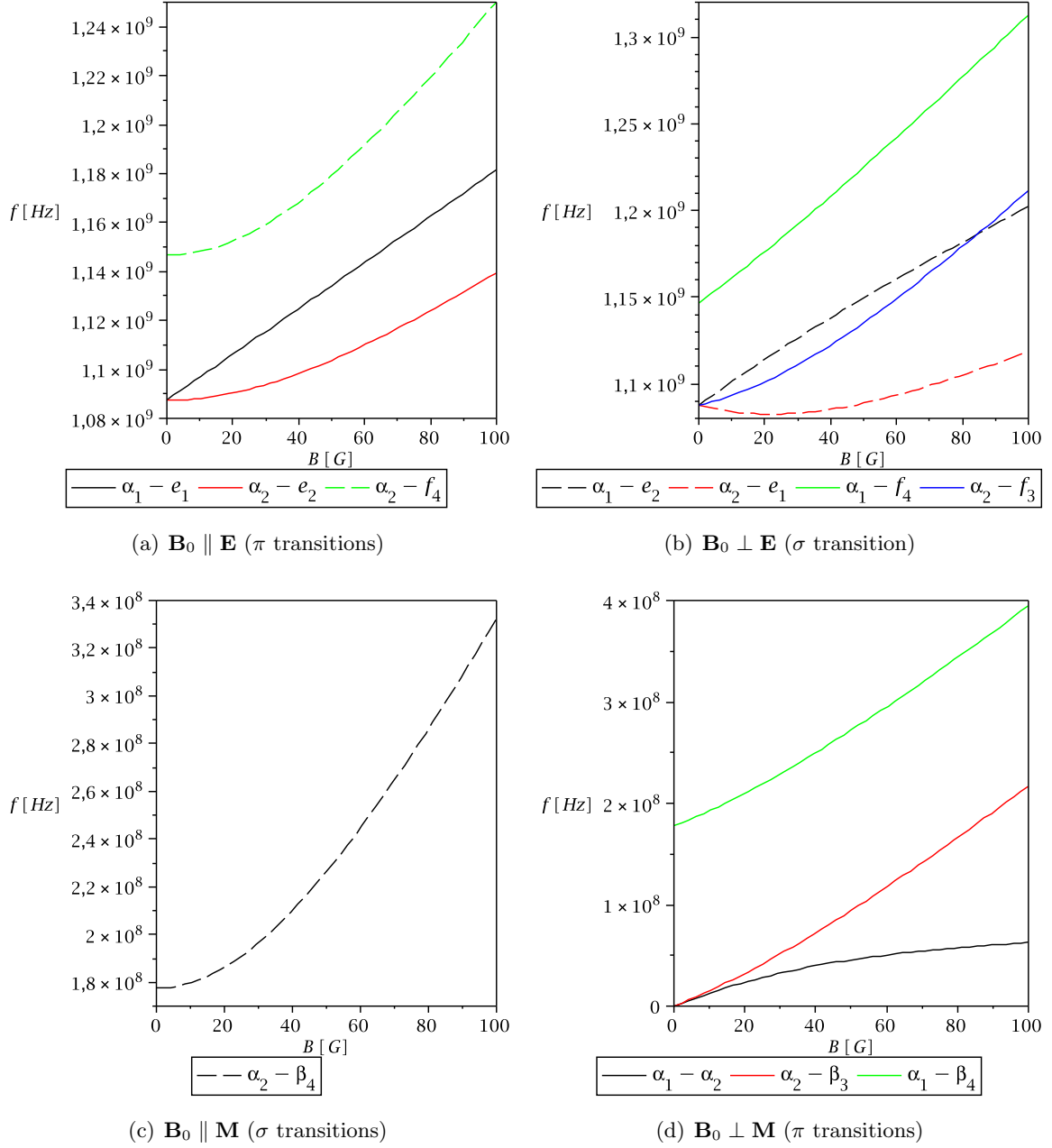


Figure 2.16: Electric and magnetic dipole transitions which can be observed with the modified LSP in hydrogen as function of the magnetic field calculated with the recent Breit-Rabi formulas. Here \mathbf{E} and \mathbf{M} are the electric and magnetic field vectors of the time-dependent field. The dashed lines correspond to transitions which vanish for magnetic fields larger than the critical magnetic-field strength.

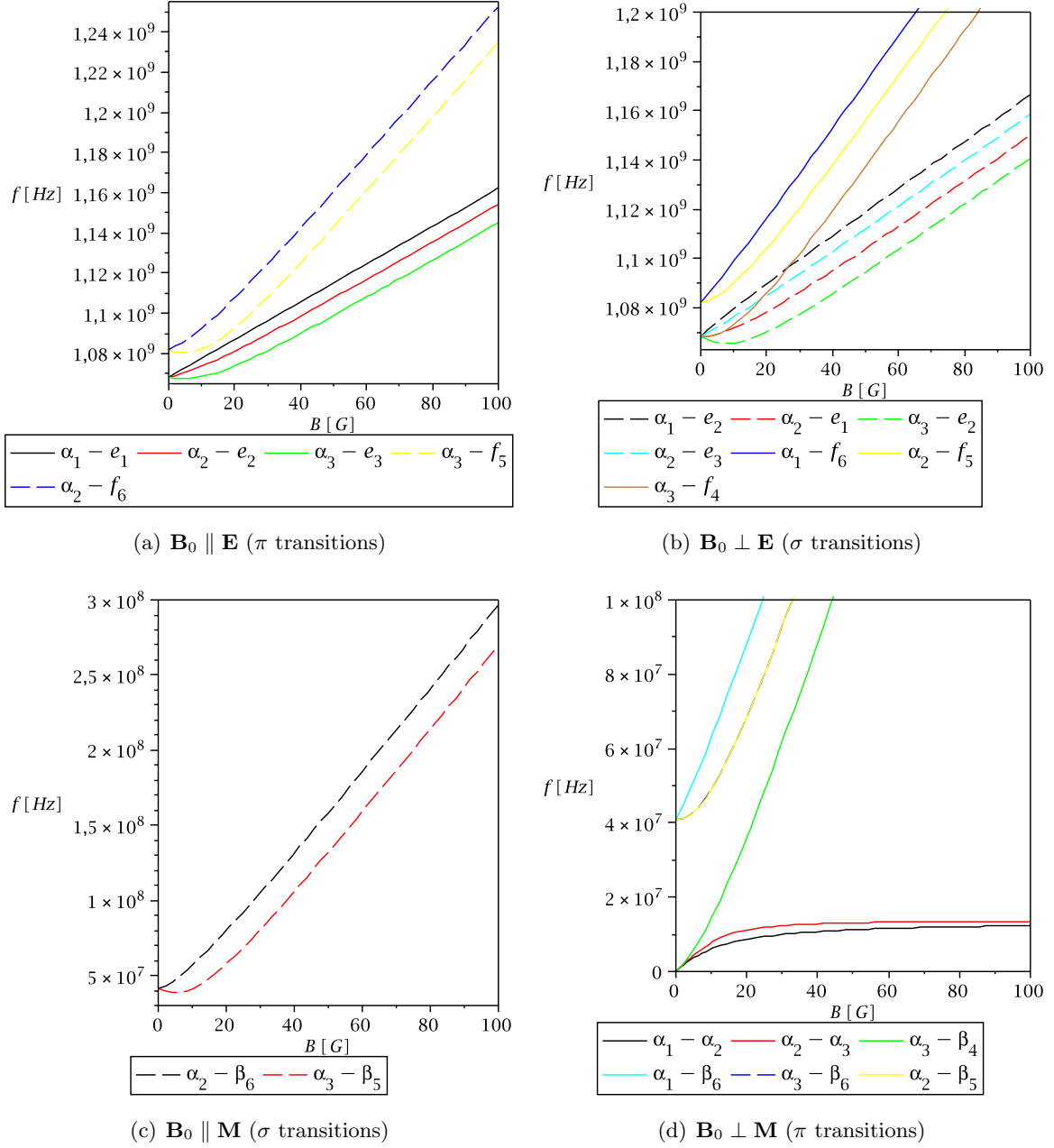
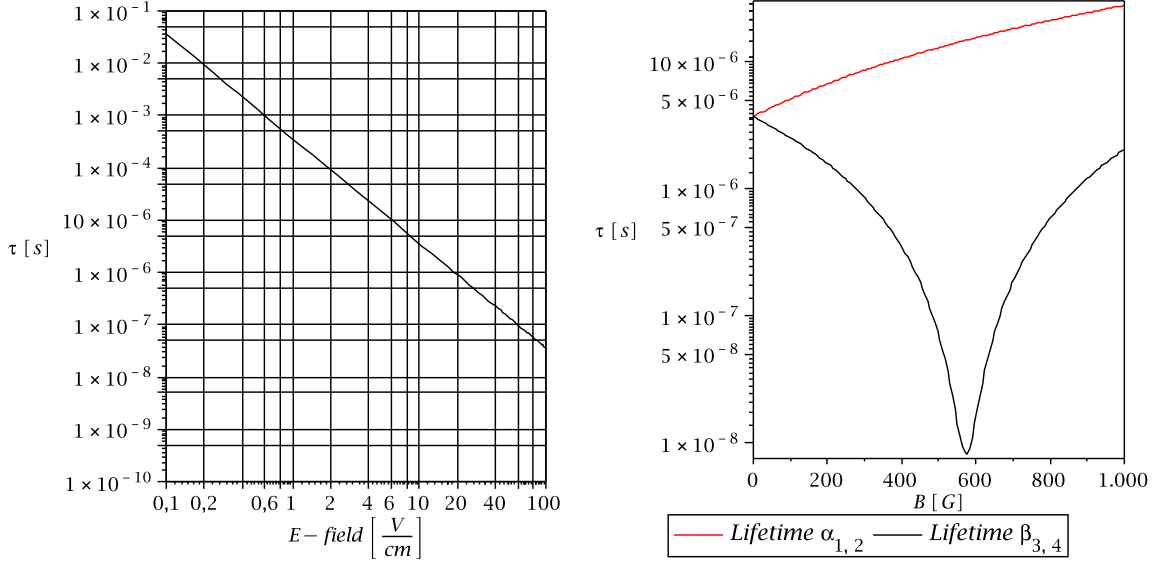


Figure 2.17: Electric and magnetic dipole transitions in deuterium as function of the magnetic field calculated with the recent Breit-Rabi formulas. The $\alpha_3 \rightarrow \beta_6$ transition is very similar to the $\alpha_2 \rightarrow \beta_5$ transition and cannot be resolved in (d).

2.4 Atoms in a Static Electric Field - The Stark Effect

Speaking about the Stark effect in the hydrogen and the deuterium atom, respectively, means dealing with the influence of a static electric field \mathcal{E} on the properties of these atoms. A static electric field has an influence on the atomic binding energy very similar to the situation of an atom in an external magnetic field (Zeeman effect). In contrast to the Zeeman effect, an electric field does not remove the degeneracy of an atomic level. Atomic states with the same absolute value of the magnetic quantum number are still degenerate. Although this feature is not mentioned in the most textbooks, the Stark effect is a very useful effect in experimental atomic physics because with the help of an electric field the lifetime of atomic states can be manipulated (fig. 2.18). This is a very important application which was used in the experiment performed in the framework of this thesis. One has to distinguish between two kinds of the Stark effect, the quadratic and the linear Stark effect, i.e. the modification of the atomic levels due to an external electric field is proportional to \mathcal{E}^2 or to \mathcal{E} . Starting by characterizing the atomic states of hydrogen and deuterium, respectively, with the three quantum numbers n, l and m_l only, it is simple to derive analytically that the modification of the ground-state energy levels is proportional to \mathcal{E}^2 while for the first excited state it is proportional to \mathcal{E} . According to the stationary perturbation theory, this can be done by calculating the matrix elements $\langle n, l, m_l | \hat{H}_{Stark} | n', l', m'_l \rangle$ of the Stark Hamiltonian which reads in the position space $\hat{H}_{Stark} = -e\mathcal{E}z$. Defining z as quantization axis, the \mathcal{E}^2 proportionality of the ground-state energy correction originates from the first non-vanishing contribution of the perturbation series expansion which are second order terms proportional to $\sum_{n \neq 1, l', m'_l} |\langle 1, 0, 0 | -e\mathcal{E}z | n', l', m'_l \rangle|^2$ and in order to that proportional to \mathcal{E}_z^2 . The quadratic Stark effect can be observed in every atom, especially in multi-electron atoms (e.g. alkali atoms) because there is no l degeneracy. As mentioned in subsec. 2.1.1, the l degeneracy in the hydrogen and the deuterium spectrum, respectively, is due to the r^{-1} proportionality of the Coulomb potential which is not exact fulfilled in multi-electron atoms. Electrons in higher shells see a weaker nuclear charge than electrons in lower shells, also due to the nuclear charge screening of lower electron states. Exclusively in hydrogenlike atoms in states with principal quantum number $n > 1$ the linear Stark effect can be observed because these states are l degenerate in the non-relativistic theory. As an example the $2S$ and $2P$ levels in the non-relativistic theory of hydrogen and deuterium can be considered. Calculating the matrix elements of the Stark Hamiltonian for the first excited state, the first non-vanishing contribution are first order terms proportional to $\langle 2, l, m_l | -e\mathcal{E}z | 2, l', m'_l \rangle$ and, therefore, the energy correction is proportional to \mathcal{E}_z . Furthermore, since there exist non-vanishing matrix elements between the $2S$ and the $2P$ states any electric field mixes the metastable $2S$



(a) $2S_{1/2}$ lifetime τ as function of an external electric field. (b) Lifetime of the $2S_{1/2}$ Zeeman components in an electric field of $10 \frac{\text{V}}{\text{cm}}$ as function of the magnetic field. The β components have a lifetime minimum in the vicinity of the crossing points with the e components of the unstable $2P_{1/2}$ state (compare with fig. 2.14).

Figure 2.18: Manipulation of the lifetime of the metastable $2S_{1/2}$ state with electric and magnetic fields in the hydrogen atom. Similar plots can be obtained for the deuterium atom.

state ($\tau \approx 0.14$ s) with the unstable $2P$ state ($\tau = 1.6 \cdot 10^{-9}$ s) reducing the lifetime of the $2S$ state (metastability quenching, fig. 2.18). A precise determination of level shifts in an electric field within a fully relativistic framework under consideration of the hyperfine structure was not possible in the time-frame of this thesis. Nevertheless, for a precision experiment as prepared in this thesis a determination of this kind has to be done to be able to estimate level shifts and, therefore, the uncertainty of transition frequencies due to external electric fields. The concept of the calculation is quite simple. To determine level shifts for the first excited state of hydrogen all matrix elements of the Stark Hamiltonian in the $\{|n, l, j, F, m_F\rangle\}$ basis have to be calculated, i.e. for the fine structure terms $2S_{1/2}$, $2P_{1/2}$ and $2P_{3/2}$ including the hfs. The $2S_{1/2}$ state with $l = 0$ in hydrogen is metastable, because, due to the conservation of angular momentum, there is no direct transition, i.e. no one-photon transition, into the ground state possible. A static electric field mixes the $2S_{1/2}$ state with the $2P_{1/2}$ and $2P_{3/2}$ states ($l = 1$) which shifts the energy of the hfs levels of the $2S_{1/2}$ state and, furthermore, of the $2P_{1/2}$ and the $2P_{3/2}$ levels, too. The $2S_{1/2}$ state is closer to the $2P_{1/2}$ state than to the $2P_{3/2}$ state. Furthermore, the $F = 0$ hfs level of the $2S_{1/2}$ state is closer to the $2P_{1/2}$ state than the $F = 1$ hfs level. Vice versa, the $F = 1$ hfs level of the $2S_{1/2}$ state

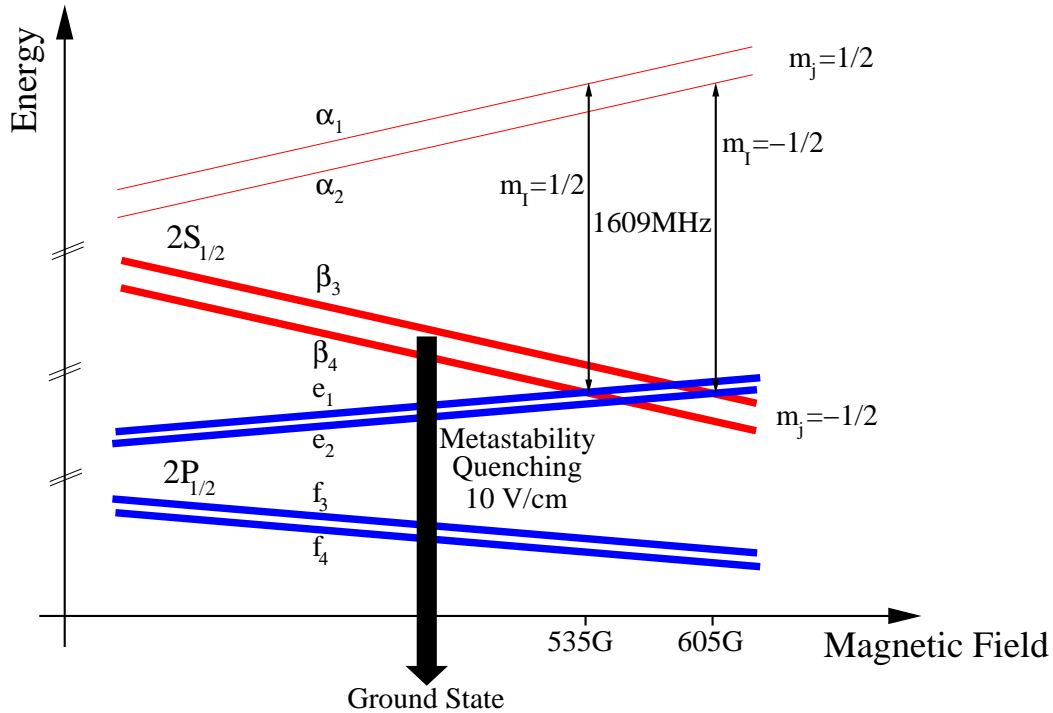
is closer to the $2P_{3/2}$ state than the $F = 0$ hfs level. Because of that, the energy levels are shifted in a complicated manner due to an external electric field. To obtain the energy correction, the Stark Hamiltonian in the $\{|n, l, j, F, m_F\rangle\}$ basis for the three above mentioned states has to be diagonalized. Although the matrix elements are calculable without problems using the Wigner-Eckart theorem, the diagonalization of the Hamiltonian is not easy!

In fig. 2.18 two figures are presented to illustrate the lifetime manipulation of the metastable $2S_{1/2}$ state with an electric field (fig. 2.18(a)) and with a combination of an electric and a magnetic field (fig. 2.18(b)). Especially fig. 2.18(b) is very useful to understand the modified Lamb shift polarimeter to be explained in sec. 3.2.

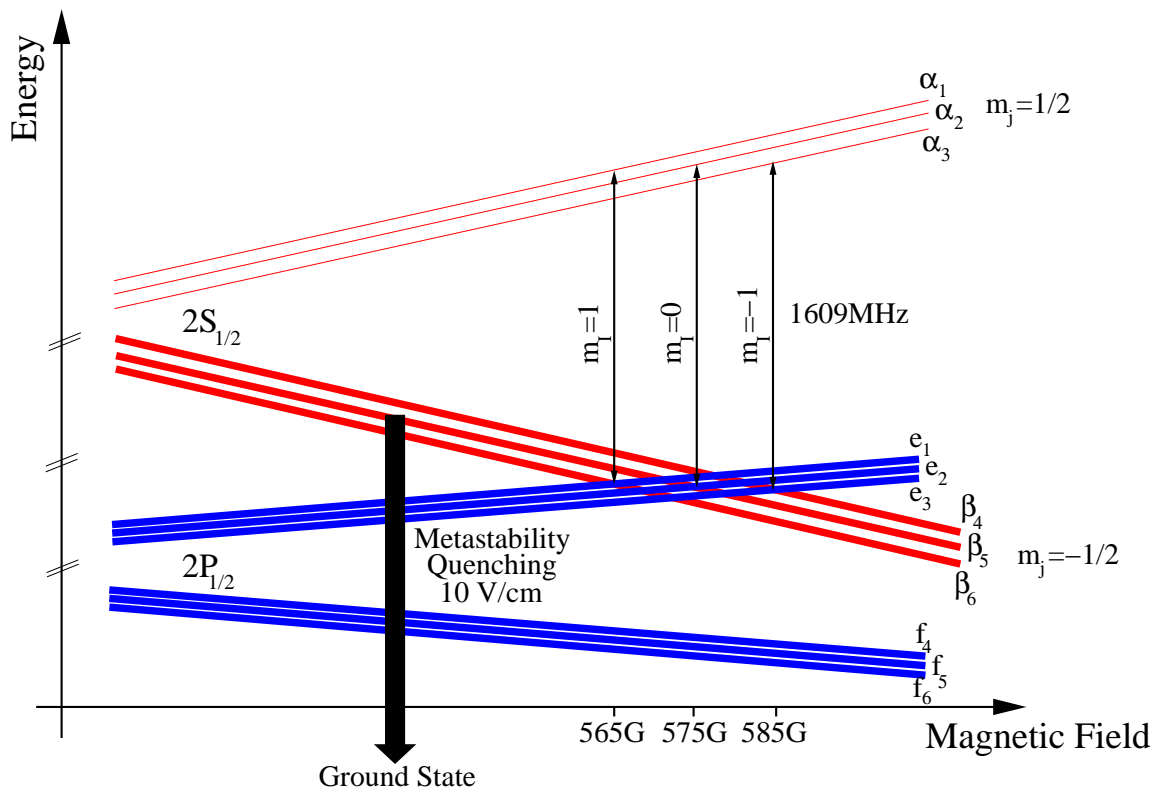
2.5 On the Concept of Producing Polarized Metastable Hydrogen and Deuterium Atoms

Why is it useful to polarize metastable hydrogen and deuterium atoms for a precision measurement as described in this thesis? A polarized atom is in a well defined quantum state. Transitions from this quantum state, say e.g. from α_1 , are well-known according to the selection rules (figs. 2.16 - 2.17). Therefore, the analysis of the transition spectra is simplified because only a few known transitions can be observed. The concept of how to polarize metastable hydrogen and deuterium atoms is illustrated in figure 2.19. A sketch of a portion of the hydrogen and deuterium Breit-Rabi diagrams is presented. Just as before, the red lines belong to the $2S_{1/2}$ state and the blue lines to the $2P_{1/2}$ state. As illustrated in fig. 2.18(b), in a magnetic field where the β states of the $2S_{1/2}$ state cross the e states of the $2P_{1/2}$ state in combination with an electric field of $10 \frac{\text{V}}{\text{cm}}$, the lifetime of the β states is enormously reduced. The β states undergo a transition to the ground state due to the mixing with the unstable $2P_{1/2}$ state (metastability quenching). As an example, applying this procedure to an ensemble of metastable hydrogen atoms, only atoms in the states α_1 and α_2 survive which are far separated from the unstable $2P_{1/2}$ state. To produce polarized atoms, one of the two α states has to undergo a transition to the ground state. A polarized ensemble of metastable hydrogen atoms in the state α_1 can be produced if in an electric field of $10 \frac{\text{V}}{\text{cm}}$ and in a static longitudinal magnetic field of approximately 538 G, metastable hydrogen atoms pass a cavity with a rf field (FWHM²⁰ \approx 1 MHz) of a certain power and a frequency $f_0 \approx 1609$ MHz producing a radial magnetic rf field and a longitudinal electric rf field relative to the static magnetic field. In this case, many of the atoms stay in oscillation between the states α_1 and β_4 while all other states undergo a transition into the ground

²⁰Full Width at Half Maximum



(a) Concept of producing polarized metastable hydrogen atoms.



(b) Concept of producing polarized metastable deuterium atoms.

Figure 2.19: Sketch (not to scale!) of a portion of the hydrogen (a) and deuterium (b) Breit-Rabi diagrams in the first excited state to illustrate the idea of producing polarized metastable atoms. The $\beta_{3,4}$ and $\beta_{4,5,6}$ states, respectively, are broadened due to the mixing with the $2P_{1/2}$ state. All $2P_{1/2}$ Zeeman components are also broadened because of the short lifetime.

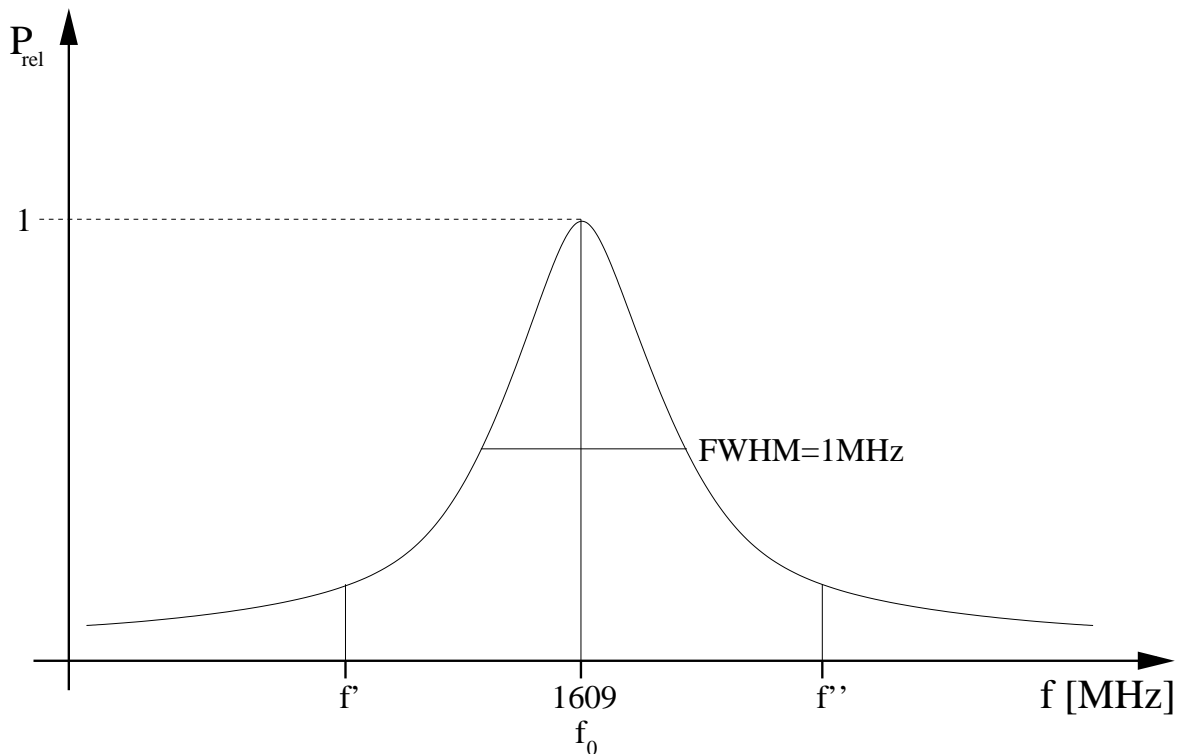


Figure 2.20: Sketch of the cavity output power (expressed in dimensionless relative units) as function of the frequency.

state. Turning off the rf field, atoms in the β_4 state mix with the $2P_{1/2}$ state and return into the ground state, too. The remaining atoms are in the α_1 state and a polarized ensemble of metastable hydrogen atoms is obtained.

A crucial point of this method is to succeed in a strong coupling of the state α_1 with β_4 while the coupling between the state α_2 and β_3 has to be weak. For the weak coupling a lower frequency $f' < f_0$ with a considerable weaker power is needed than for the strong coupling. In this case the oscillation between the states $\alpha_1 \leftrightarrow \beta_4$ is fast compared to the oscillation between the states $\alpha_2 \leftrightarrow \beta_3$. This means, that less atoms in the oscillation $\alpha_1 \leftrightarrow \beta_4$ return to the ground state than in the slower oscillation $\alpha_2 \leftrightarrow \beta_3$ due to the weaker coupling. The mean time in the state β_4 of atoms of the fast oscillation $\alpha_1 \leftrightarrow \beta_4$ is shorter than in the state β_3 of the slower oscillation $\alpha_2 \leftrightarrow \beta_3$. Therefore, more atoms are quenched into the ground state which are in the oscillation $\alpha_2 \leftrightarrow \beta_3$ until the state α_2 is completely emptied. The difference in the coupling strength described above can be achieved as follows. Experimentally (sec. 3.2.7) it can be observed that the frequency f_0 has to have a FWHM of 1 MHz because with this FWHM a lower frequency f' with weak power can be found in the high-frequency field which fits into the difference $\alpha_2 \leftrightarrow \beta_3$ (fig. 2.20).

Analogously, polarized metastable hydrogen atoms in the state α_2 can be produced with the same method as described above by only changing the magnetic field from 538 G to 605 G. In this case the FWHM of 1 MHz allows to find a frequency $f'' > f_0$ with weak power which fits into the difference $\alpha_1 \longleftrightarrow \beta_4$. So, the α_1 state is emptied in this case.

The same holds for the metastable deuterium atom. Choosing magnetic fields of approximately 565 G, 575 G and 585 G, polarized metastable deuterium atoms in the states α_1 , α_2 and α_3 can be produced.

CHAPTER 3

EXPERIMENTAL SETUP

3.1 Principle of the Measurement

For a better understanding of the experimental setup presented in the next section, a rough overview about the principle of the measurement should be presented first.

Chapter 2 introduced the theory of the hydrogen and the deuterium atom, respectively, also delivering insight to recent theoretical research. With the device presented below, spectroscopy experiments with a metastable hydrogen or deuterium beam can be performed in a new way never tried before to the best of the author's knowledge. The experiment prepared for the first time in this thesis provides spectroscopy experiments to measure the $2S_{1/2}$ and $2P_{1/2}$ hfs, the Breit-Rabi diagram of the $2S_{1/2}$ and $2P_{1/2}$ state and the classical Lamb shift. Therefore, a metastable atomic beam in only one Zeeman state of the hfs is produced with a modified Lamb-shift polarimeter (modified LSP) described in sec. 3.2. Dependent on the configuration of the spectroscopy chamber (subsec. 3.2.8) of the modified LSP, electric or magnetic dipole transitions can be induced in the atoms entering the spectroscopy chamber. Due to the well defined quantum state of the atoms, the measured spectrum belongs only to a few and well-known transitions according to the selection rules of quantum mechanics (fig. 2.16 - 2.17). **First tests to show the proof-of-principle of the experiment were performed with a metastable hydrogen beam.**

3.1.1 Electric Dipole Transitions

To determine a value of the classical Lamb shift, electric dipole transitions between the $2S_{1/2}$ state and the $2P_{1/2}$ state have to be induced. Therefore, a special device, a TEM waveguide (Transversal Electro Magnetic waveguide), has to be mounted in the spectroscopy chamber. While metastable atoms pass the TEM waveguide, their electric dipole moment interacts with a dominating electric rf field, therefore, electric dipole transitions are induced. The emitted light of the atoms returning from the $2P_{1/2}$ state

into the ground state can be directly measured with a photomultiplier, sensitive to a discrete wavelength region around the 121 nm line (Lyman- α radiation), i.e. ultraviolet light, on the top of the spectroscopy chamber. A more detailed explanation can be found in subsec. 3.2.8. Furthermore, for the measurement of the $2P_{1/2}$ hfs and the $2S_{1/2}$, $2P_{1/2}$ Breit-Rabi diagrams, the TEM waveguide can also be used.

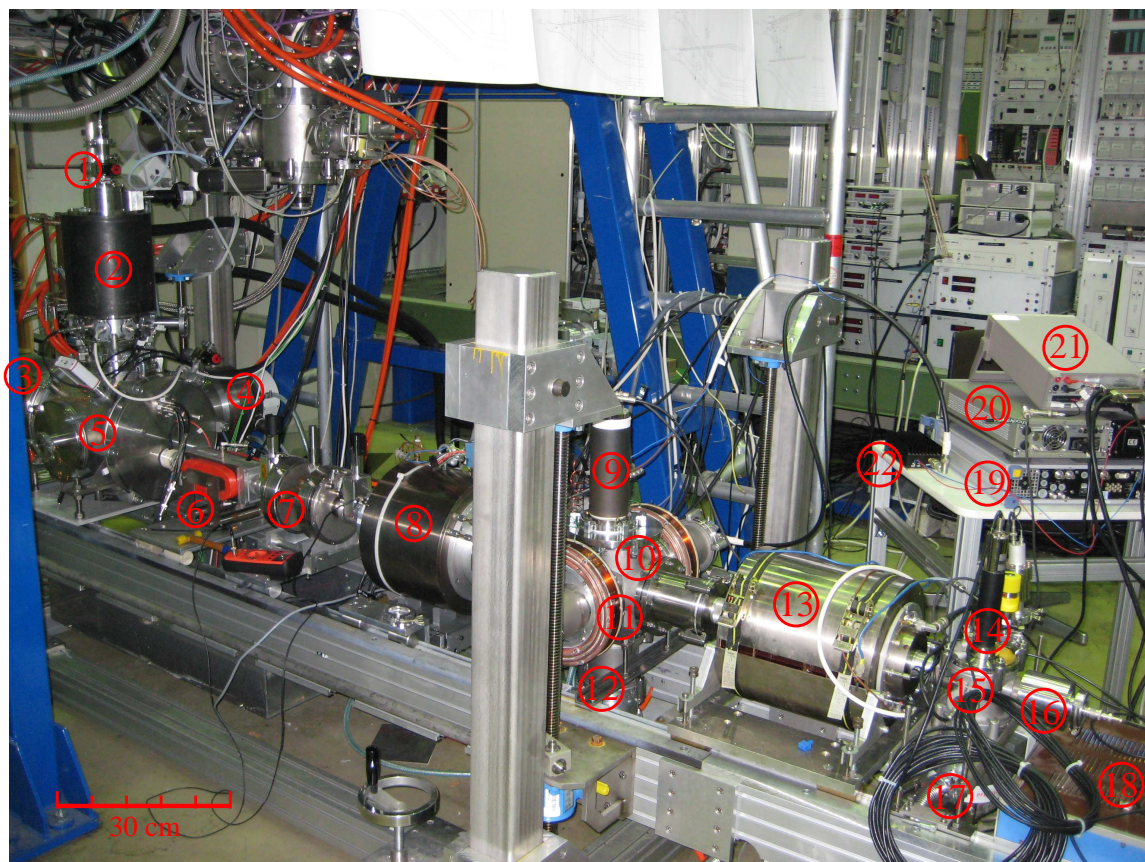
3.1.2 Magnetic Dipole Transitions

Magnetic dipole transitions within the $2S_{1/2}$ state cannot occur in the electric rf field of the TEM waveguide. Instead of the TEM waveguide, a magnetic rf coil has to be installed in the spectroscopy chamber which produces a dominating magnetic rf field. The magnetic dipole moment of the atoms passing this field coil interacts now with a dominating magnetic rf field and, therefore, magnetic dipole transitions are induced. While in the case of electric dipole transitions the emitted light during a transition can be directly measured with a photomultiplier, the incidence of magnetic dipole transitions has to be measured indirectly. Within the limited time-frame of this diploma thesis it was not possible to perform measurements of magnetic dipole transitions, however, the operation mode of the field coil and of the modified LSP for this kind of measurements is explained in subsec. 3.2.8. To obtain the full Breit-Rabi diagrams of the $2S_{1/2}$, $2P_{1/2}$ states, magnetic dipole transitions also have to be measured. Furthermore, to obtain a value for the $2S_{1/2}$ hfs, the magnetic rf coil is also needed.

3.2 The modified Lamb-shift Polarimeter

3.2.1 Overview

In figs. 3.1 and 3.2, respectively, the experimental setup assembled in the course of this thesis is shown. The parts 1 – 9 and 15 – 17 are the Lamb-shift polarimeter (LSP) such as described in [Eng02, Eng03]. In the Forschungszentrum Jülich, at the COoler SYnchrotron (COSY) of the Institute of Nuclear Physics, the LSP is used to measure the beam polarization of a polarized hydrogen (deuterium) beam source to determine the target-gas polarization of the Polarized Internal Target (PIT) of the ANKE (Apparatus for Studies of Nucleon and Kaon Ejectiles) experiment. LSP's, such as operated in Jülich, allow a fast determination of the polarization of hydrogen and deuterium atoms and provide an alternative to Breit-Rabi polarimeters. The knowledge of the atomic polarization allows to deduce the polarization of the atomic nuclei, i.e. the polarization of the target in nuclear scattering experiments which is a crucial parameter for the data analysis. With a LSP, the beam polarization can be



- | | | |
|---------------------|-------------------------|----------------------------|
| ① Valve | ⑧ 1st Spinfilter | ⑮ Quench Chamber |
| ② Ionizer | ⑨ Big Photomultiplier | ⑯ Faraday Cup |
| ③ Cryo Pump | ⑩ Spectroscopy Chamber | ⑰ Turbo Drag Pump |
| ④ Turbo Drag Pump | ⑪ Magnetic Field Coils | ⑱ HV Small Photomultiplier |
| ⑤ Deflector Chamber | ⑫ Turbo Drag Pump | ⑲ RF Power Generator |
| ⑥ Wien Filter | ⑬ 2nd Spinfilter | ⑳ Powermeter |
| ⑦ Cesium Cell | ⑭ Small Photomultiplier | ㉑ Keithley Multimeter |
| | | ㉒ RF Power Amplifier |

Figure 3.1: Experimental setup assembled in this thesis at the Forschungszentrum Jülich. The main parts of the modified LSP are labeled with red numbers.

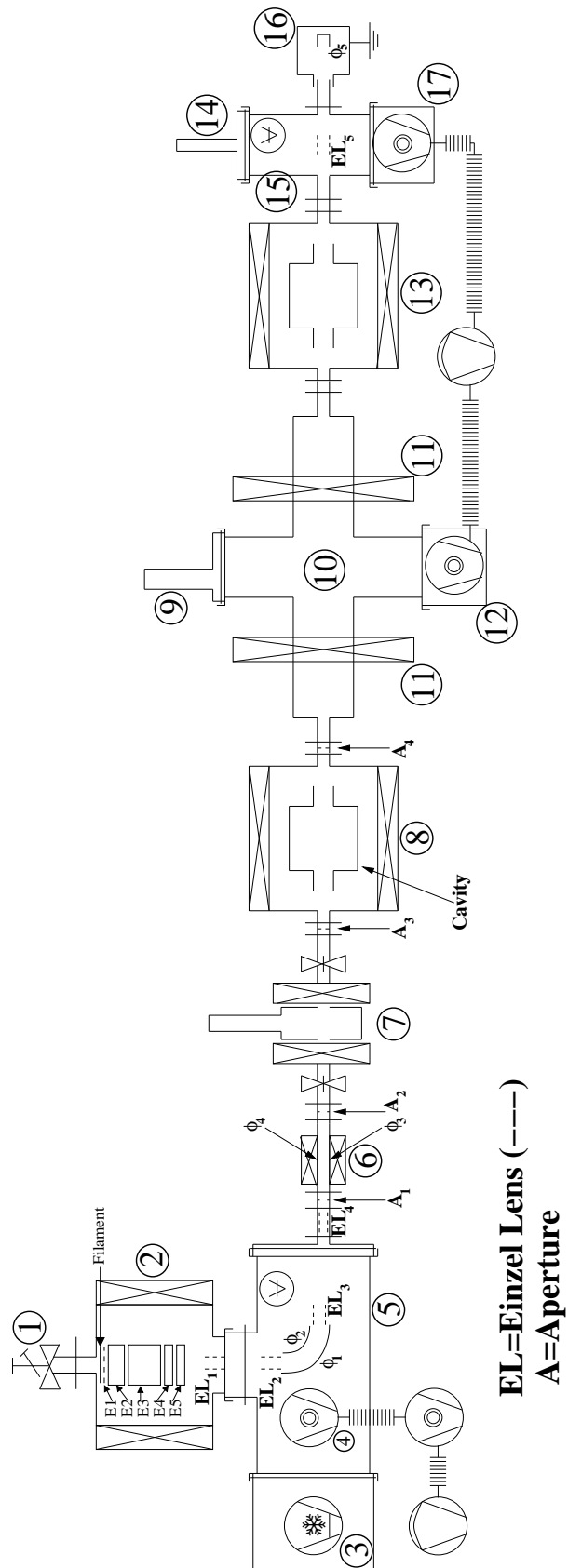


Figure 3.2: Sketch of the modified LSP. The labels have the same meaning as in fig. 3.1. For vacuum parts and pumps, the standard nomenclature was used.



- | | |
|--|---|
| ① Heating Cryo Pump | ⑨ Electric Field 1st Spinfilter&Wien Filter |
| ② Electric Field 2nd Spinfilter | ⑩ Electric Field Ionizer Potentials&EL ₁ |
| ③ Current Magnetic Field Coils | ⑪ Electric Field Deflector&EL ₂ ,EL ₃ |
| ④ Current 2nd Spinfilter Solenoid | ⑫ Heating Cesium Cell |
| ⑤ RF Power Module (~1609MHz) | ⑬ Current 1st Spinfilter Solenoid |
| ⑥ Electric Field
EL ₂ & TEM Waveguide Quench Field | ⑭ HV Big Photomultiplier |
| ⑦ Current Wien Filter | ⑮ RF Power Module (~1609MHz) |
| ⑧ Ionizer Filament | |

Figure 3.3: Power supplies for the devices of the modified LSP shown in fig. 3.1 and in fig. 3.2, respectively.

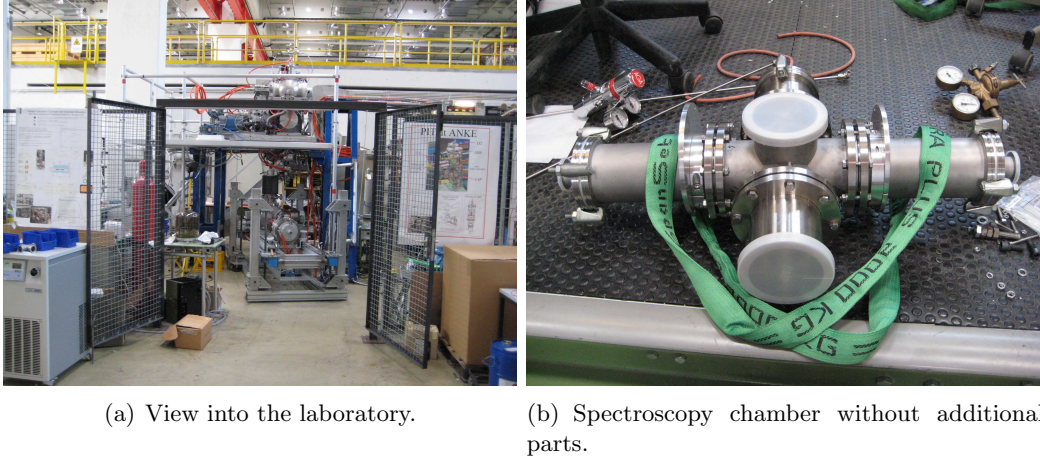


Figure 3.4: Impressions during the assembly of the modified LSP.

determined within a few seconds with an uncertainty of less than 1%. Polarimeters to determine target polarizations or which are used for online tuning of polarized beams are the basis of polarized measurements. Although, in the broader sense, the LSP is used originally for nuclear physics experiments, in this thesis it was modified to perform pure atomic physics experiments.

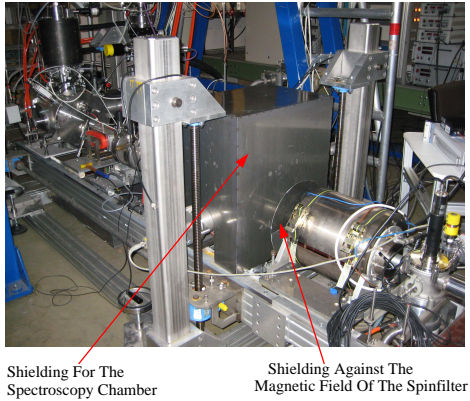


Figure 3.5: Modified LSP with μ -metal shielding (compare with fig. 3.3).

to the setup in fig. 3.1, a shielding was added to the setup shown in fig. 3.5.

The modified LSP was assembled outside of the COSY ring in the LKW-Schleuse of the COSY building in a laboratory which is shown in fig. 3.4(a). In the next subsections a brief overview of the hardware parts will be given.

Therefore, it was supplemented by a spectroscopy chamber (part 10 in figs. 3.1 and 3.2) and a second spinfilter (part 13 in the same figure). With this setup it is possible to perform spectroscopy experiments with metastable hydrogen and deuterium atoms in the first excited state. Atomic physics spectroscopy experiments are sensitive to external sources of electromagnetic fields, so it was necessary during the experimental period of this thesis to prepare a shielding for the spectroscopy chamber of the modified LSP. Compared

3.2.2 Pumping System

As can be seen in fig. 3.2, a pumping system consisting of different pump types was attached to the experiment (see also fig. 3.6 for the meaning of the symbols). Vacuum gauge heads of the type *Pfeiffer Vacuum HPT 100* are installed at the deflector chamber and at the quench chamber (denoted by the reversed “A” in fig. 3.2). Membrane pumps (*Pfeiffer Vacuum MVP 055-3*) with a pumping speed of $S(N_2) = 3.3 \text{ m}^3/\text{h}$ are used as booster pumps. Further on four turbo-molecular drag pumps are used. The biggest turbo-molecular drag pump of the type *Pfeiffer Vacuum TMH 1000P* with a pumping speed of $S(N_2) = 880 \text{ l/s}$ is mounted at the deflector chamber. To guarantee a sufficient backing pressure, this pump is supported by a small turbo-molecular drag pump (*Pfeiffer Vacuum TMH 261*, $S(N_2) = 210 \text{ l/s}$).

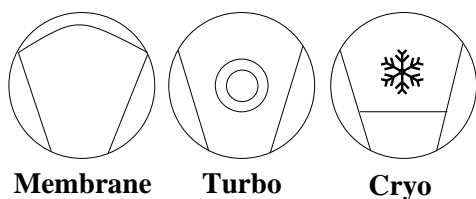


Figure 3.6: Symbols for membrane, turbo and cryo pumps following the standard nomenclature.

Two additional turbo-molecular drag pumps (*Pfeiffer Vacuum TMH 261*) are mounted below the spectroscopy chamber and below the quench chamber. In addition a *Leybold Coolvac 3000-1* cryo pump with a pumping speed of $S(N_2) = 3000 \text{ l/s}$ is used at the deflector chamber. Supplementary there is the possibility to install getter material in the ionizer of the modified LSP. However, such a getter pump was not used during the measurements of this thesis.

The best method to reach high vacua is to use metal seals. In static experiments which do not have to be developed anymore and which have to fulfill the UHV standard, such a sealing is preferable. Because the modified LSP does not have to fulfill the UHV standard, here for a maximum flexibility, viton seals were chosen. Three types of flanges were used, ISO-K, small flanges (KF) and LASKA norm. Especially the LASKA norm which was also used decades before in the Forschungszentrum Karlsruhe, is a very flexible self-centering flange system allowing to unplug vacuum devices within seconds. Pressures which can be reached with the pumping system of this experiment are $8 \cdot 10^{-8} \text{ mbar}$ in the deflector chamber while the pressure in the quench chamber is $2 \cdot 10^{-6} \text{ mbar}$.

3.2.3 The Ionizer

The ionizer used in this thesis can be operated in two different modes, in the electron bombardment mode and in the plasma mode. A more detailed description can be found in [Emm00, Eng02]. Inside the ionizer (fig. 3.2) four cylinder electrodes $E2$ –

$E5$, a grid $E1$ and a filament are arranged. The whole ionizer volume is surrounded by a solenoid producing a strong magnetic field of approximately 1200 G. A typical potential distribution is presented in fig. 3.7. Electrons emitted from the filament are accelerated towards the grid $E1$ into the strong magnetic field of the ionizer. To keep the electrons in the ionizer volume, the filament and the electrode $E4$ are grounded while the electrode $E2$ and $E3$ are kept on a positive potential, so the electrons are trapped.

Inflowing hydrogen (deuterium) gas, where the flux was adjusted with a needle valve ($\approx 10^{-3}$ mbar l/s), is ionized in the cylindrical volume of the electrode $E3$. The ionization process is amplified by the magnetic field of the ionizer solenoid. Electrons which are emitted from the filament and enter the ionizer volume are forced to spiral trajectories. Therefore, collisions of electrons with inflowing hydrogen (deuterium) molecules

are increased. During the ionization process, protons (deuterons), and an additional amount of residual gas and ions are produced. If now the potential of the electrode $E2$ is always more positive than the potential of the electrode $E3$, the protons (deuterons) and the positive ions cannot escape in backward direction of the ionizer. With the two electrodes $E4$ and $E5$ a potential gradient for the protons (deuterons) is produced and they are accelerated only in forward direction. The energy of a proton or a deuteron is defined with the potential of the electrode $E3$, i.e. with the potential where the ionization takes place. As already mentioned, the ionizer can be operated in two different modes. The electron bombardment mode can be activated by setting the potentials $E2$ and $E3$ to values less than 1 kV and the magnetic field of the ionizer should not be too strong (this has to be determined in the experiment itself). Compared to this, the plasma mode can easily be activated by increasing the potentials of the electrodes $E2$ and $E3$ and by increasing the magnetic-field strength of the ionizer solenoid. By measuring the flux of positive ions (e.g. on the deflector electrode ϕ_1 , fig. 3.2), the two modes can easily be distinguished from each other, because the plasma mode is more efficient, i.e. a more intense flux of positive ions can be measured compared to the electron bombardment mode. In this thesis the plasma mode was used to produce an intense ion flux. The difficulty for the experimenter using this mode is to reach a stable 1H_2 (2H_2) partial pressure in the ionizer.

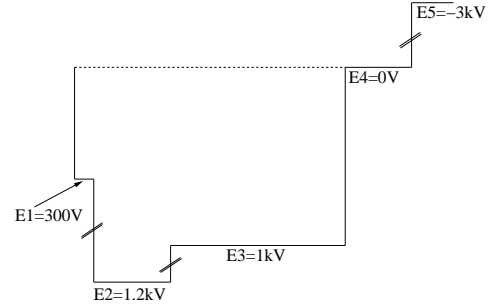


Figure 3.7: Potential distribution inside the ionizer running in the plasma mode.

3.2.4 The Deflector Chamber

For a first measurement, the deflector chamber and the ionizer were used in the same configuration (fig. 3.1) as they are mounted at the ANKE experiment. The extracted ion beam of the ionizer is deflected around 90° by the bended deflector electrodes shown in fig. 3.2. The potentials ϕ_1 and ϕ_2 have to be suitably tuned to allow a maximum ion flux through the deflector chamber. Beam development was done by using the Faraday cup (part 16 in figs. 3.1 and 3.2) and the big photomultiplier (part 9 in the same figures). In the framework of this thesis, developing a beam means that a maximum particle flux leaving the ionizer has to reach the Faraday cup while the cesium cell (subsec. 3.2.6) is switched off. After that the cesium cell is switched on and the metastable hydrogen (deuterium) beam, produced while protons (deuterons) pass through the cesium cell, is optimized with the help of the big photomultiplier and an electric quench field in the spectroscopy chamber. Behind the ionizer electrode $E5$, the ion beam can be focused by electrostatic lenses mounted at the exit of the ionizer, in the deflector chamber and at the exit of the deflector chamber (lenses $EL_1 - EL_4$, fig. 3.2). After passing through the cesium cell (part 7 in figs. 3.1 and 3.2), the metastable beam cannot be focused anymore. This means, during the beam development the lenses have to be tuned as carefully as possible because after the cesium cell the beam will evolve without the possibility to influence the beam shape from outside. Vacuum conditions are another critical point to obtain a maximum convergent beam¹. In particular this is valid for a hydrogen and a deuterium (metastable) atomic beam, because hydrogen and deuterium are the lightest atoms and due to this notably influenced by collisions with other heavier elements. The pumping system described in subsec. 3.2.2 was sufficient to produce convergent atomic beams for first experiments.

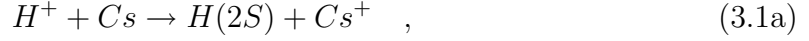
3.2.5 The Wien Filter

In a Wien filter (part 6 in figs. 3.1 and 3.2), an electric and a magnetic field which are perpendicular to each other are used to filter charged particles with different velocities according to the relation $|\mathbf{v}| = |\mathcal{E}| / |\mathbf{B}|$. In the case of the modified LSP, therefore, it was possible to separate protons from other charged particles. The magnetic field was switched off, because the strength of the residual magnetization in the iron core of the Wien filter was sufficient.

¹The number of background particles in a vacuum chamber which has to be passed by a particle beam is reciprocally proportional to the mean free path. Pressure and background particle number are directly proportional to each other according to the ideal gas law. I.e. lowering the gas pressure in the vacuum chamber increases the mean free path. If the particle beam does not collide with gas molecules, it will not be scattered to other directions than the beam direction and the beam stays convergent.

3.2.6 The Cesium Cell

The cesium cell is a gas target consisting of cesium atoms which are used to take advantage of the charge exchange reactions



to produce metastable hydrogen (deuterium) in the first excited state $2S_{1/2}$. Incoming protons (deuterons) pass through the cell (fig. 3.8) and collide with cesium atoms. According to [Pra74, Eng02], the charge exchange reaction has a maximum cross section of $6 \cdot 10^{-15} \text{ cm}^2$ at a proton energy of 550 eV and at a deuteron energy of 1100 eV. The optimal target density in the cell is approximately $10^{14} \text{ atoms/cm}^2$. To produce a target density of this order, a vapor pressure of about $1.5 \cdot 10^{-2} \text{ mbar}$ over the liquid cesium is needed. Therefore, it has to be heated to a temperature of $160 \text{ }^\circ\text{C}$.

The cell can be opened to insert a cesium ampoule. After closing the cell, it can be evacuated so the cesium cannot react with oxygen to form cesium oxide. Once a good vacuum is reached, the ampoule can be cracked from outside with a special mechanism. Liquid cesium flows down and accumulates at the bottom part of the cell. The bottom part, as well as the top part of the cell can be heated. Heating the bottom part to a temperature of $160 \text{ }^\circ\text{C}$, the needed target density can be produced. Gaseous

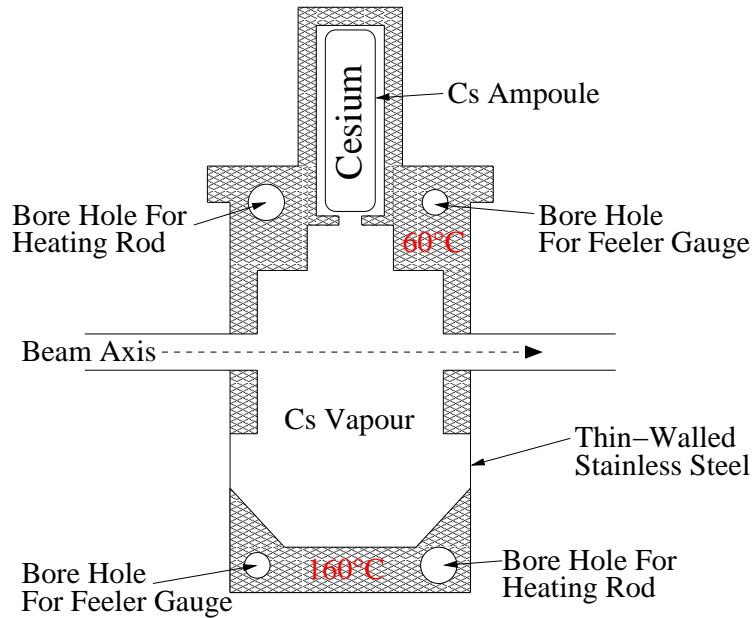


Figure 3.8: Sketch of the cesium cell.

cesium diffuses in the cell volume and hits the top part of the cell which is heated to a temperature of 60 °C where the cesium condenses and drops back to the bottom part. The cesium cell consists of thin-walled stainless steel to keep up the temperature gradient between the top and the bottom part of the cell. First measurements in this thesis were performed with hydrogen atoms. Although for protons the cross section for the charge exchange reaction with cesium has a maximum at a beam energy of 550 eV, a proton energy of approximately 1 keV was chosen due to a better beam convergence at this energy, i.e. the ionizer electrode *E3* was set to a value of 1000 V. At an energy of 1 keV, anyhow, the cross section for the charge exchange reaction is approximately $2.5 \cdot 10^{-15} \text{ cm}^2$. At this energy about 15% of the total hydrogen atoms are in the first excited state after the charge exchange reaction in the cesium cell.

3.2.7 The Spinfilter

In sec. 2.5 the concept of producing polarized metastable hydrogen and deuterium atoms was presented. The spinfilter, which is briefly explained in this subsection, is primary the core of a LSP and works according to the principle described in sec. 2.5. With this device it is possible to allow the transmission of single Zeeman components of the hfs of metastable hydrogen and deuterium. In particular this means, that the states α_1 or α_2 of hydrogen and α_1 , α_2 or α_3 of deuterium, respectively, can be selected to pass the spinfilter while all other components are quenched into the ground state. The polarization of an atomic beam, therefore, can be measured with this device. Otherwise, an unpolarized metastable atomic beam entering the spinfilter is polarized after passing through the spinfilter.

For the first time the spinfilter was proposed in the year 1968 by McKibben and collaborators [McK68]. In [Eng02] a LSP was developed to measure the nuclear polarization of gas targets and of polarized ion sources for nuclear physics experiments. The same spinfilter like used in [Eng02] (part 8 in figs. 3.1 and 3.2) was also used for the measurements in this thesis. In addition a second spinfilter was borrowed from the group of Hans Paetz gen. Schieck of the Institute of Nuclear Physics from the University of Cologne (part 13 in figs. 3.1 and 3.2).

The cavity of the second spinfilter is shown in fig. 3.9, consisting of four electrical separated quadrants. In the other spinfilter a similar cavity is used. Two opposite quadrants maintain an electric quenching field while a rf field is applied to the remaining two quadrants. The two ends of the cavity consist of small quadrants respectively. An electric potential of approximately 150 V between the big quadrants (part 1) and of approximately 80 V between the small quadrants (part 3) turns out to be a perfect adjustment. With these values an electric field of about 10 V/cm is produced on the beam axis in the middle of the spinfilter. At a frequency of approximately $f_0 \approx$

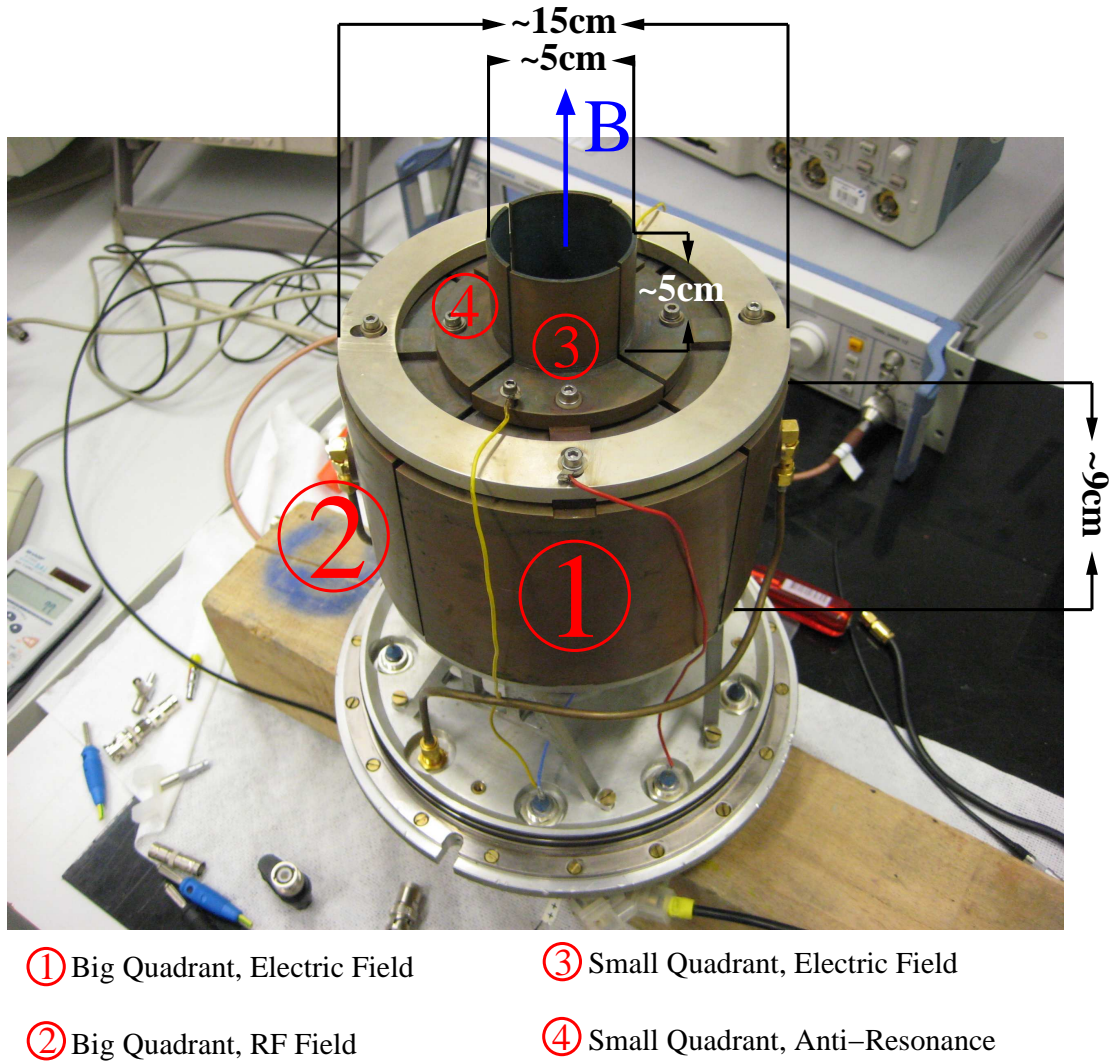


Figure 3.9: Spinfilter cavity during adjustment work. The blue arrow suggests the direction of the magnetic field produced by the solenoid surrounding the cavity (fig. 3.2) which is not shown in this figure.

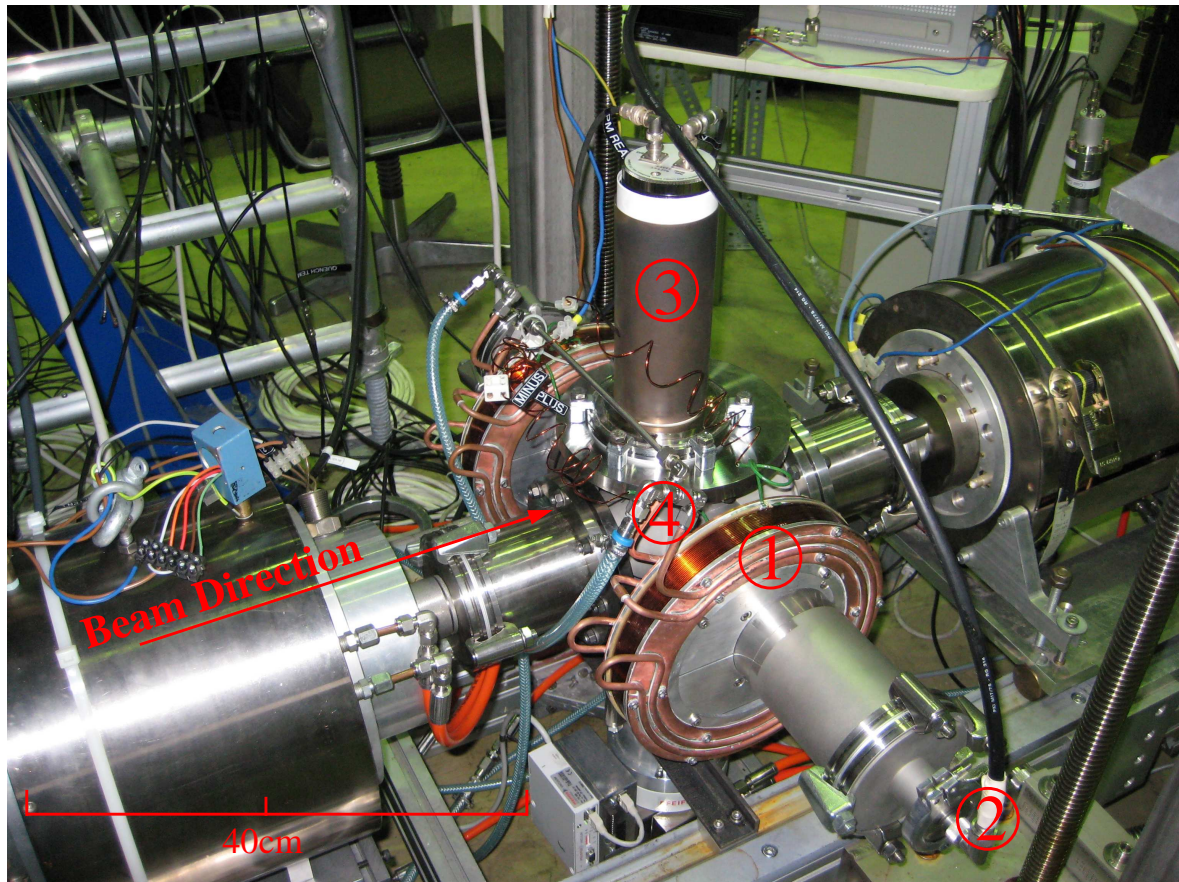
1.60975 GHz with a FWHM of 1 MHz, the cavity is tuned to be resonant according to [Eng02]. Fig. 3.9 shows the cavity during the adjustment work. Compared to the vacuum speed of light c_0 , the speed of light in air c_{air} is 0.29 ‰ slower. Therefore, the cavity has to be tuned to a lower frequency of about $f'_0 \approx 1.60959$ GHz before placing it into the vacuum. The anti-resonant small quadrants (part 4) guarantee to keep the rf in the cavity, because they are a fraction of the wavelength corresponding to f_0 ($f_0 = 1.60975$ GHz $\hat{=}$ 18.6 cm = λ_{hf}). Furthermore, the small quadrant at the entry of the cavity is used to preselect the states α_1 and α_2 in hydrogen and α_1 , α_2 and α_3 in deuterium, respectively, while the metastable atomic beam enters the cavity. The small quadrant at the exit of the cavity is used to quench all remaining atoms in

the states β_3 and β_4 in hydrogen and β_4 , β_5 and β_6 in deuterium, respectively, into the ground state to obtain a beam in a pure quantum state. The diameter of the cavity is a factor 1.31 smaller than the wavelength λ_{hf} . This geometry is required to produce a TM_{010} resonance, i.e. a radial magnetic rf field and a longitudinal electric rf field inside the cavity as requested in sec. 2.5. The power of the irradiated rf field was chosen to be about 80 mW. In fig. 3.2 a sketch of the spinfilter is presented. As can be seen, the cavity is attached into a solenoid which produces a static longitudinal magnetic field also required for the state selection as described in sec. 2.5. For more information on how a homogeneous static magnetic field is produced in the spinfilter, see [Eng02]. In addition to a solenoid, the spinfilters have trim coils, so one has the possibility to correct for field inhomogeneities.

A metastable hydrogen (deuterium) beam entering the spinfilter adjusted to the right parameters as described in sec. 2.5, leaves the spinfilter in one definite Zeeman component of the hfs like already mentioned above.

3.2.8 The Spectroscopy Chamber

For the measurement performed in this thesis, a spectroscopy chamber was used which is shown in fig. 3.10. The chamber itself is a standard ISO-K 100 6-way cross made of stainless steel. It turned out that the remanence of the stainless steel distort the spectra of the atomic transitions, however, for a proof-of-principle the quality of the chamber was sufficient. On top of the chamber, a large volume photomultiplier of the type *Electron Tubes 9424B* (photocathode made from KBr, $\lambda_{lim.} < 160$ nm, with a quantum efficiency of 8 %; viewing window made from MgF, $\lambda_{lim.} > 110$ nm) is installed which is sensitive to a discrete wavelength region around the 121 nm line. Therefore, it is possible to directly observe transitions in the ultraviolet spectrum. For the readout of the photomultiplier, a *Keithley Multimeter 2000* was used, which is connected to a PC via the GPIB port. As an example, transitions of atoms to the $2P_{1/2}$ state should be mentioned which immediately return into the ground state by emitting ultraviolet light which can be measured with the photomultiplier. In front and behind the spectroscopy chamber a spinfilter is installed respectively for two different operation modes of the modified LSP which are described in the next section. On two opposite tubes of the chamber, coils are attached to produce a homogeneous static magnetic field inside the chamber. In the chamber itself, two different devices can be installed. A TEM waveguide produces a homogeneous electric rf field and a magnetic rf coil produces a magnetic rf field with field vectors parallel to the beam axis. As can be seen, the coil configuration shown in fig. 3.10 is excentric with respect to the chamber. This is due to the excentric position of the interaction region in the TEM waveguide to be specified below. The configuration of the magnetic-field coils shown in



- | | |
|------------------------|-------------------|
| ① Magnetic Field Coils | ③ Photomultiplier |
| ② Typ-N RF Cable | ④ Water Cooling |

Figure 3.10: Spectroscopy chamber between the two spinfilters.

fig. 3.10 produces a magnetic field perpendicular to the beam axis and, therefore, also perpendicular to the field vectors of the rf fields inside the chamber. Thus, according to the selection rules of quantum mechanics, selected transitions can be induced (fig. 2.16 - 2.17). It is also possible to remount the magnetic-field coils and rotate them by 90° to produce a magnetic field which is parallel to the beam axis and, therefore, also parallel to the field vectors of the rf fields inside the chamber. First measurements were performed with an external static magnetic field perpendicular to the rf fields. In the limited time-frame of this thesis it was not possible to measure with a longitudinal field configuration.

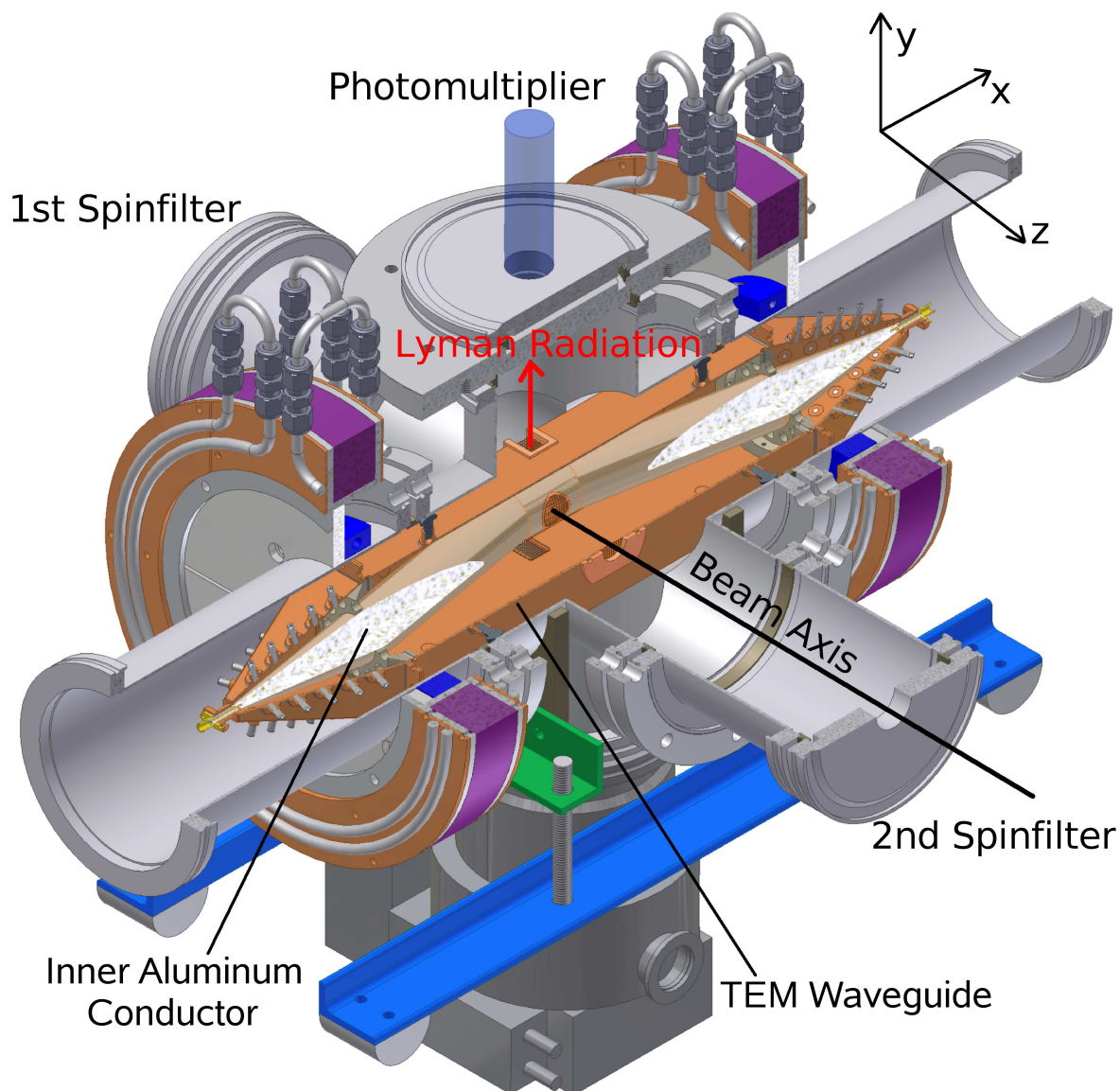


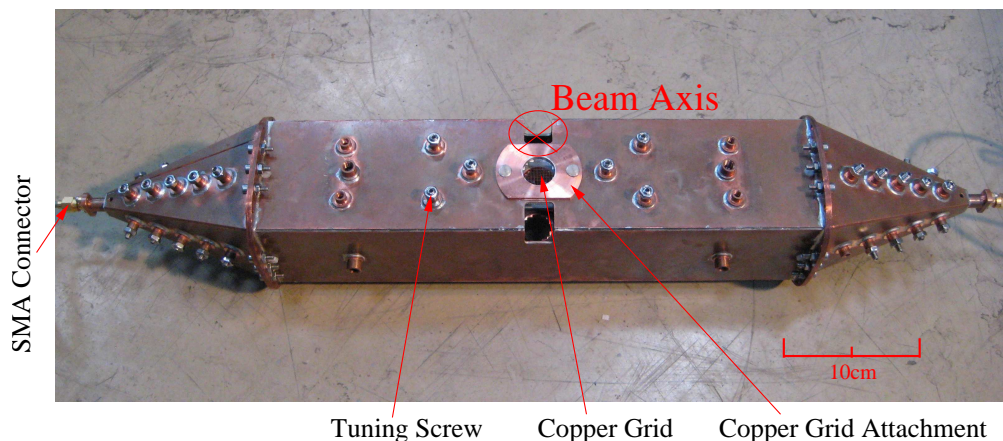
Figure 3.11: CAD design of the spectroscopy chamber with TEM waveguide installed (design by Maxim Mikirtychians (IKP-2), TEM waveguide calculation by Gepard Schug (IKP-4)). A 90° cutout of the drawing allows to show the content of the spectroscopy chamber and the inner conductor of the TEM waveguide. Further elements of the chamber are labeled elsewhere (fig. 3.10). In the figure the backside of the TEM waveguide is shown compared to fig. 3.12(a) which shows the front side. The 1st and the 2nd spinfilter are not shown in the CAD drawing, but the labels imply where they are installed.

The TEM Waveguide

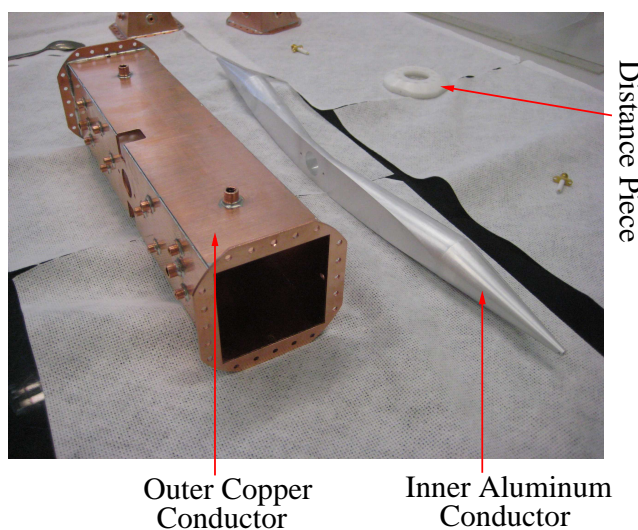
With the TEM waveguide a homogeneous electric rf field can be produced where the amplitude is kept as constant as possible while the frequency can be changed in a range from 700 MHz to 1400 MHz. A constant field amplitude which is proportional to the power of the electromagnetic rf field is required to keep the transition probability for an electric dipole transition constant and, therefore, not to distort the corresponding resonance shape.

As an example, the measurement of the $2S_{1/2}$, $2P_{1/2}$ Breit-Rabi diagrams as a function of an external magnetic field, the $2P_{1/2}$ hfs and the classical Lamb shift can be performed by using the TEM waveguide to find the resonance between the energy levels of the hydrogen (deuterium) atom directly. The latest efforts to directly² measure for example the classical Lamb shift with rf methods were made by Lamb and collaborators in the 1940's and 1950's. Compared to the TEM waveguide, Lamb had to chose another method because of several reasons. For the production of a rf field with a certain power, he used klystrons, i.e. fixed-frequency generators. During the years he was performing his measurements, there were no signal generators available which allowed to produce a rf field with constant power while changing the frequency. Therefore, he used a waveguide inside a dipole magnet and klystrons for several fixed frequencies. The dipole magnet produces a very homogeneous field inside the waveguide volume. While changing the magnetic field he was able to find resonances in the atoms, if, according to the Breit-Rabi diagrams, the fixed frequency corresponds to the difference between the Zeeman components of the $2S_{1/2}$ and $2P_{1/2}$ energy levels. In the experiment presented in this thesis, a method was developed to find resonances in metastable hydrogen (deuterium) atoms in a homogeneous magnetic field, produced by a coil system, by changing the frequency of the applied rf field. This method Lamb was not able to perform due to the problems described above but which is in his opinion the best method to carry out such a measurement (mentioned in Lamb's six-part publication series "Fine Structure of the Hydrogen Atom"). The TEM waveguide consists of an outer copper and an inner aluminum conductor which are electrically separated from each other with the distance pieces shown in figs. 3.12(b) and 3.12(c). Both ends of the outer conductor of the TEM waveguide have a pyramidal shape and on each end an appliance for a SMA connector is soldered. The outer part of the SMA connector is grounded by the outer conductor of the TEM waveguide and the core is connected to the aluminum conductor. The geometry of the TEM waveguide components (i.e. outer and

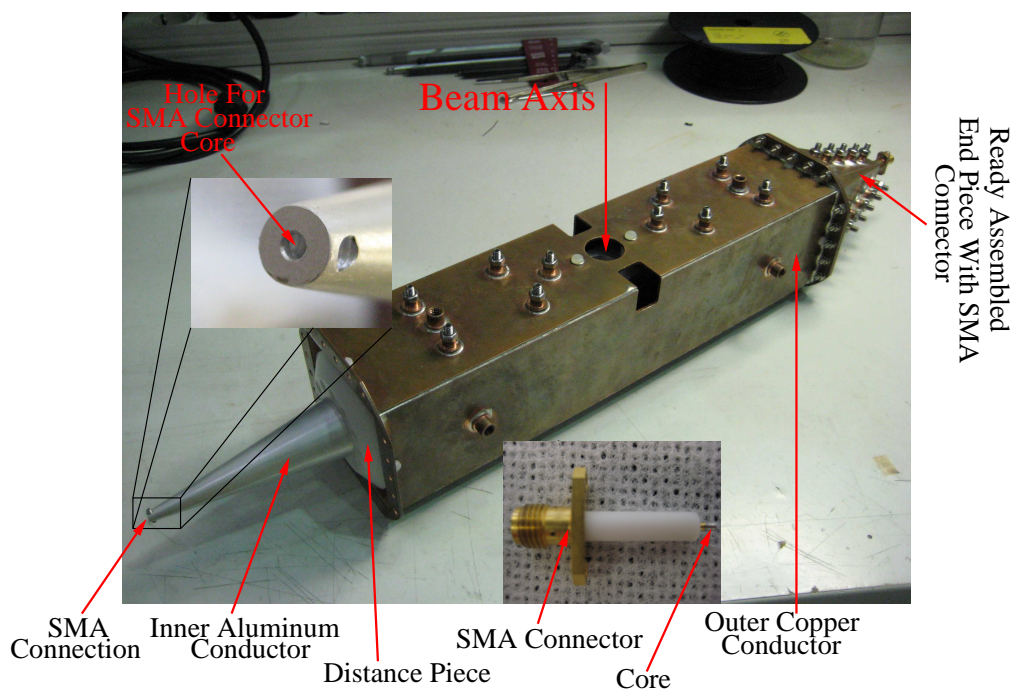
²A direct measurement of the classical Lamb shift or another quantity in an atomic spectrum means to apply an experimental technique to determine a quantity in the atom directly. At this, no additional informations to determine this quantity have to be taken into account because a direct measurement includes all informations which are needed. This means, such an experimental technique is self consistent and does not depend on other experiments. Wherever this is possible, a physical quantity should be determined like this!



(a) Frontside of the fully assembled TEM waveguide. The beam axis goes from the top of the picture to the bottom, indicated by the circled red cross.



(b) Parts of the TEM waveguide without the pyramidal-shaped end pieces.



(c) TEM Waveguide during the assembly.

Figure 3.12: The TEM waveguide.

inner conductor) resulted from the chamber geometry (fig. 3.11) and the requirement of a preferably homogeneous electric rf field in the interaction region (fig. 3.14). To couple the electromagnetic rf field from the signal generator into the TEM waveguide, a good connection from the SMA connector to the inner conductor was needed. Therefore, the inner conductor was designed to have pyramidal end pieces where the SMA connector core can be fixed (fig. 3.12(c)) and equally the electromagnetic rf field can be easily coupled into the TEM waveguide. A signal generator can be connected to one end while the other end of the TEM waveguide has to be terminated with a resistance of 50Ω to avoid reflections which would cause a strong frequency dependence of the electric rf-field amplitude. The value of 50Ω has to be chosen because of the same impedance of the cables and because of the signal generator connected to the TEM waveguide. Stainless-steel screws are distributed over the surface of the outer conductor which can be screwed into the volume of the TEM waveguide to influence the impedance of the TEM waveguide itself and adjust it also to have 50Ω impedance. Because the impedance cannot be measured like an usual resistance, it has to be measured with a network analyzer.

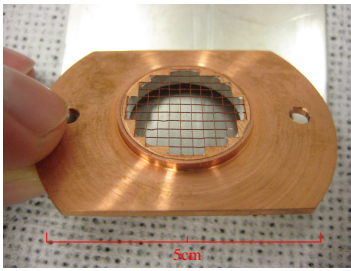


Figure 3.13: Copper grid embedded into an attachment.

An impedance of 50Ω of the TEM waveguide is reached, if the reflections inside are minimized, in the ideal case no reflections can be measured anymore. Both in the outer and in the inner conductor, holes ($\varnothing = 20 \text{ mm}$) are included for the atomic beam to pass the TEM waveguide. Ultra-violet light from an electric dipole transition can escape through the rectangular holes in the outer conductor and reach the photomultiplier on top of the spectroscopy chamber (figs. 3.10 and 3.11).

To avoid electric rf-field inhomogeneities inside the TEM waveguide volume, the holes were closed with copper grids with a luminosity of approximately 96 % (fig. 3.13, compare with fig. 3.12(a)). Systematic measurements with a network analyzer showed that it is sufficient to close only the holes where the atomic beam passes the TEM waveguide. The open rectangular holes have no influence on the electric rf-field homogeneity. However, measuring reflections in the TEM waveguide as function of spatial coordinates with a network analyzer, it can be figured out that small reflections appear close to the distance pieces. An improvement, therefore, would be to produce more transparent, i.e. thinner distance pieces. The distance between the outer and the inner conductor where the atoms enter the TEM waveguide and interact with the electric rf field, the so-called interaction region, is 1 cm broad (figs. 3.14 and 3.15). In this region the outer and the inner conductor are exactly parallel to each other and the

distance of only 1 cm allows to produce a homogeneous electric rf field. As can be seen in fig. 3.15, the interaction region is excentric with respect to the chamber, so an excentric coil system (figs. 3.10 and 3.11) is required to produce an external magnetic field perpendicular to the electric rf-field vector. The required power for a 63 % transition probability of an electric dipole transition from the $2S_{1/2}$ into the $2P_{1/2}$ state can be calculated according to the quantum theory of radiation. In the hydrogen case (i.e. the velocity of a 1 keV proton beam which is used to produce metastable atoms has to be taken into account) and for the geometry of the TEM waveguide a required power density of 186.065 mW/cm^2 can be determined. The signal generator (*Rohde&Schwarz SML02*), used to produce the electromagnetic rf field inside the TEM waveguide, has an upper power limit of approximately 100 mW. When connecting the TEM waveguide with all extension cables needed to the signal generator, at the end of the TEM waveguide approximately only 70 % of the total input power can be measured. The losses are due to the procedure how the electric field inside the TEM waveguide is homogenized in the interaction region by the tuning screws and of course by the length of the device and the extension cables. Therefore, it was necessary to use an additional rf amplifier behind the signal generator. A *Mini Circuits ZHL-4240* 40 dB amplifier with a maximum output power of 28 dBm working in a frequency range of 700 MHz to 4200 MHz was chosen, because of its output flatness of $\pm 1 \text{ dBm}$. However, for the experimental purpose the power had to be controlled online behind the TEM wave-

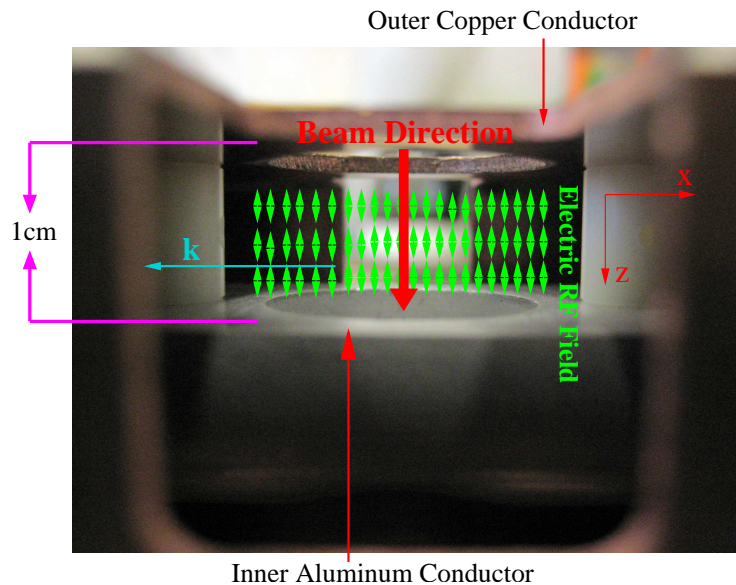


Figure 3.14: Interaction region of the TEM waveguide. At this stage of the construction no copper grids were inserted into the holes of the outer and the inner conductor. \mathbf{k} denotes the wave vector.

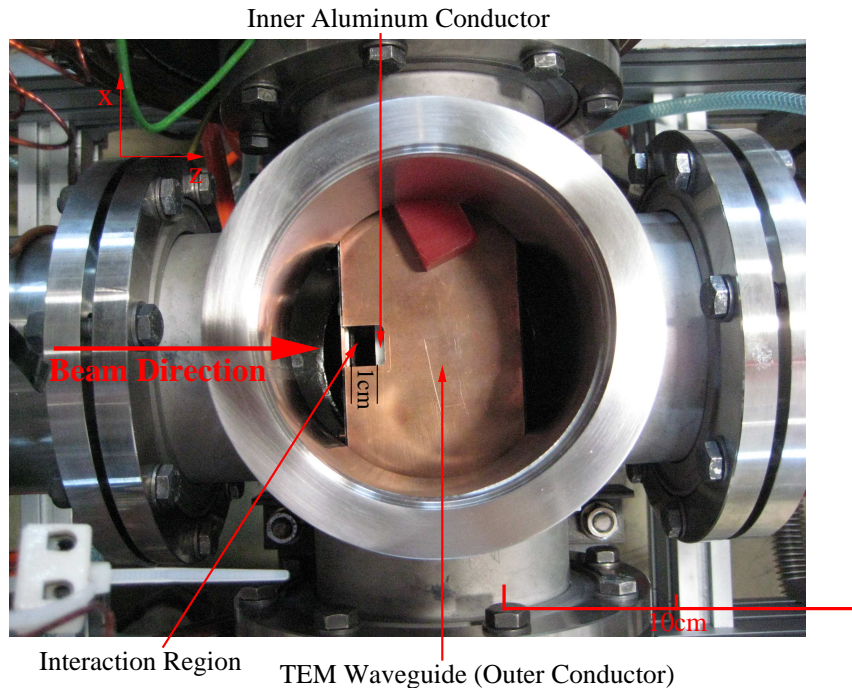


Figure 3.15: Open spectroscopy chamber with inserted TEM waveguide. Lyman- α radiation of an electric dipole transition can escape from the interaction region through the rectangular holes in the outer conductor. The photomultiplier is mounted on the top of the chamber and is only sensitive to the wavelength of such a transition (figs. 3.10 and 3.11).

guide with a *Hewlett-Packard 438 A* powermeter connected to a computer to reach a constant power amplitude in the TEM waveguide while sweeping the frequency. As an example, amplitude variations of the electric rf field of about 4 % cause variations of about 3 % in the transition probability and, therefore, the resonance shape is distorted. The option to tune the TEM waveguide to reach the best possible electric rf-field homogeneity inside the TEM waveguide and the flatness of the amplifier turned out to be good conditions for a fast control process with the powermeter and the computer. Fig. 3.16 shows the power vs. frequency dependence of the signal generator and of the TEM waveguide. As can be seen in fig. 3.16(b), the output power of the signal generator varies about 4 %! As already mentioned, this will also cause a noticeable variation in the transition probability. Furthermore, as can be seen in figs. 3.16(c) and 3.16(d), the TEM waveguide itself shows a non-constant behavior of the power on the frequency, although for the first construction and test this device was working well. In the ideal case a constant line would be measured, i.e. no dependence of the power on the frequency. The result of the power-controlling process is exemplified in figs. 3.17(c) and 3.17(d). Fig. 3.17(a) shows the power vs. frequency dependence of the rf amplifier, while fig. 3.17(b) shows the dependence of the power on the frequency of all

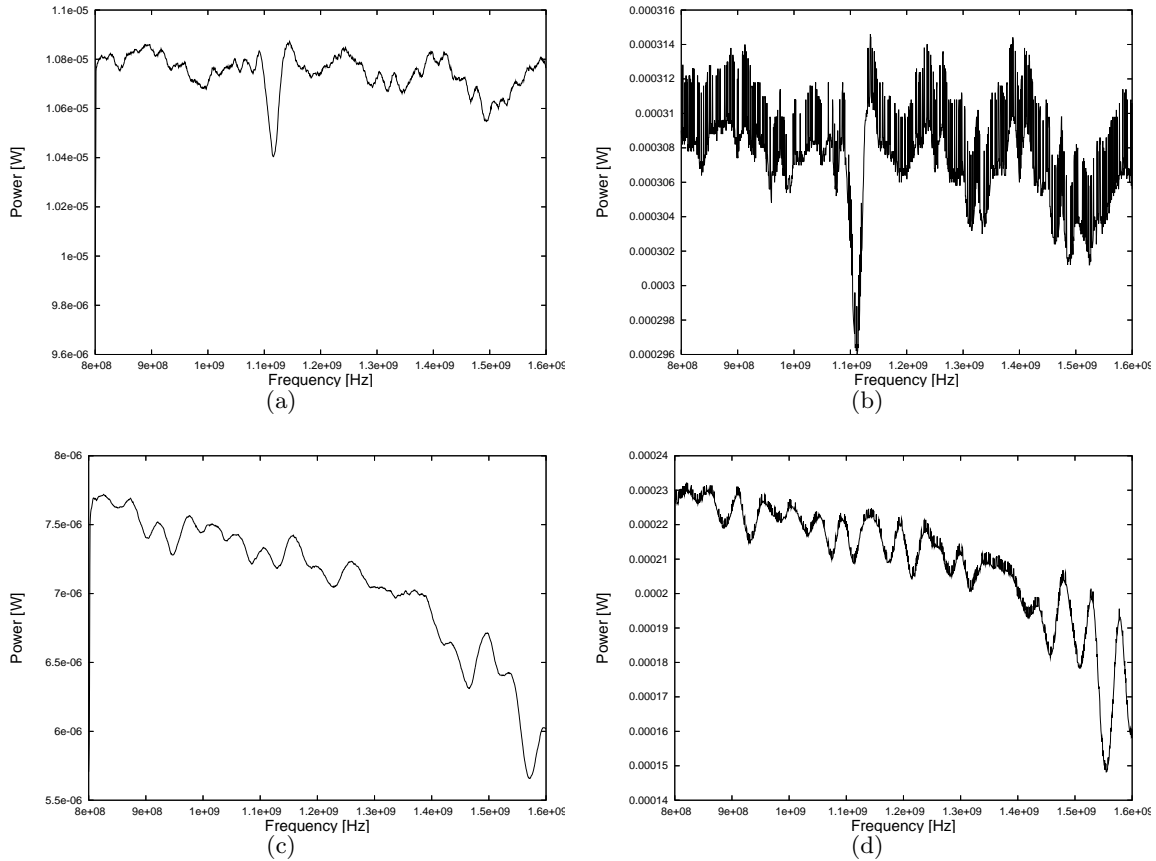


Figure 3.16: Figs. (a) and (b) show the power vs. frequency dependence of the *Rohde & Schwarz SML02* signal generator with -20 dBm and -5 dBm output power. Figs. (c) and (d) show the power vs. frequency dependence of the TEM waveguide connected to the signal generator with -20 dBm and -5 dBm output power, respectively.

devices together, i.e. of the signal generator, cables, amplifier and the TEM waveguide. Fig. 3.17(c) shows the controlled level of the signal generator to reach a constant power shown in fig. 3.17(d). It should be noticed that this result is not the final optimum! The *Hewlett-Packard 438 A* powermeter is an outdated device which showed to have a coarse scale. However, for a first test it was possible to reproducibly control the power on a 3 % level. A schematic of the power control setup is shown in fig. 3.18. The GPIB card of the computer is connected to the GPIB ports of the signal generator, of the powermeter and of the Keithley multimeter which is used for the photomultiplier read-out. Furthermore, the power sensor (resistance 50Ω) of the powermeter is connected to one end of the TEM waveguide. At the other end the electromagnetic rf field is coupled into the TEM waveguide. The input of the rf amplifier is connected to the output of the signal generator while the output of the rf amplifier is connected to the SMA connector of the TEM waveguide where the electromagnetic rf field is coupled

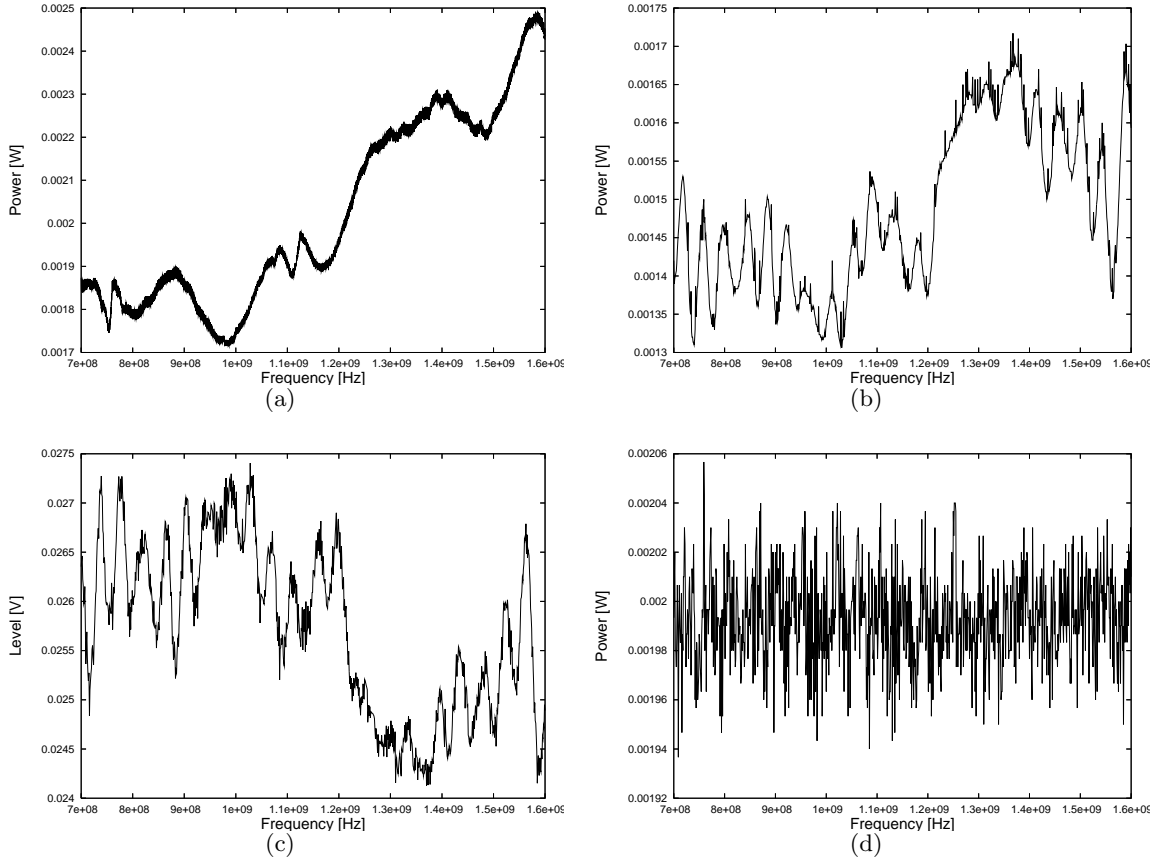


Figure 3.17: Fig. (a) shows the power vs. frequency dependence of the *Mini Circuits ZHL-4240* amplifier connected to the signal generator with -20 dBm output power. Fig. (b) shows the power vs. frequency dependence of all rf components, i.e. signal generator, cables, amplifier and TEM waveguide. Fig. (c) shows the online controlling of the signal generator to reach a constant power of 200 mW shown in fig. (d). The powermeter was protected by a 20 dB attenuator, so the y axis of (a), (b) and (d) has to be multiplied by a factor of 100.

in. Dedicated software³ provides a feedback option between the signal generator, the powermeter and the Keithley multimeter. In the software a power value can be defined which is kept constant behind the TEM waveguide in a given frequency range. For each frequency, the power is measured by the power sensor and compared to the power value defined in the software. Variations from this value are compensated by controlling the level of the signal generator. As already mentioned, the accuracy of the controlled power value is given by the accuracy of the powermeter and has to be improved. The speed of the control process itself also is limited by the speed of the powermeter. If the level of the signal generator is changed by the program, the powermeter has to reach an equilibrium until the measurement can continue. The signal generator can change its values and reach an equilibrium again within 10 ms while the powermeter is about a factor 200 slower.

³Developed by Kirill Grigoryev (IKP-2).

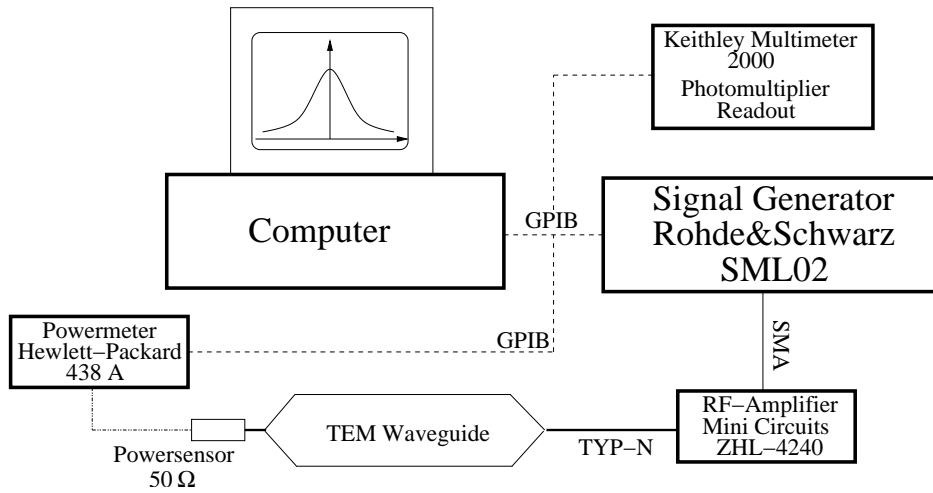


Figure 3.18: Schematic of the power-control setup of the TEM waveguide.

The TEM Waveguide as a Transmission Line

A simplified transmission line consists of two wires such as sketched in fig. 3.19(a) at which both wires are electrically separated from each other, only connected by a resistance (e.g. by a power sensor). I.e. the TEM waveguide can also be treated as a transmission line. At one end of the transmission line an alternating voltage $U_1(t) = U_{10} \exp(i\omega t)$ with frequency $f = \omega/2\pi$ is applied (e.g. generated by a signal generator), so at every point of the two wires an alternating current $I_1(t) = I_{10} \exp(i\omega t)$ is produced. Equally, at every point between the two wires an alternating voltage occurs with the same frequency. In the following treatment, only the amplitudes of the voltage and the current are important, so the time dependence $\exp(i\omega t)$ is omitted from now on. The electric behavior of such a transmission line is fully characterized by four quantities, the line loads L' , C' , R' and G' . These quantities can be explained as follows. An arbitrary segment s of the transmission line can be taken and be shortened in such a way that the current inside this segment of both wires at an arbitrary point of time has the same value I_0 . Let U_0 be the potential between the wires in this segment at an arbitrary point of time. The current I_0 is connected to a magnetic field while the potential U_0 is connected to an electric field. Therefore, according to electrodynamics, an inductance L_s and a capacitance C_s can be assigned to the segment s . The inductance per unit length s is written as $L' = L_s/s$ where the capacitance can be analogously written as $C' = C_s/s$. Furthermore, the resistance per unit length s can be written as $R' = R_s/s$ and finally the shunt conductance (dielectric losses) can be written analogously as $G' = G_s/s$. While L' and C' are only weakly frequency dependent, R' increases slowly for small frequencies while for higher frequencies R' scales with \sqrt{f} due to the skin effect. Compared to the other line-load quantities, the shunt conductance per unit length G' is strongly frequency dependent but has only values which are orders of magnitude smaller.

For a small segment $s = dx$ of the wires, the equivalent circuit shown in fig. 3.19(b) is valid. It can be used to determine two very important quantities to describe the electric behavior of a transmission line, the propagation constant $\gamma = \sqrt{(R' + i\omega L')(G' + i\omega C')}$ and the impedance $Z_w = \sqrt{\frac{R' + i\omega L'}{G' + i\omega C'}}$. Using these two quantities, the amplitude of the voltage and of the current, respectively, can be written

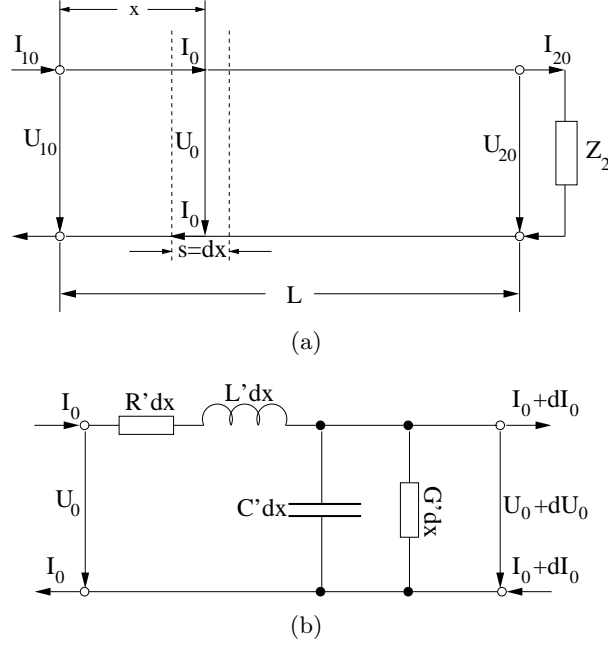


Figure 3.19: Fig. (a) shows a sketch of a transmission line of total length L terminated with a resistance Z_2 . Fig. (b) shows an equivalent circuit for the point x of length $s = dx$ to explain the line loads.

as

$$U_0 = U_{mx} + U_{rx} = U_{m0} \exp(-\gamma x) + U_{r0} \exp(\gamma x) \quad , \quad (3.2a)$$

$$I_0 = I_{mx} + I_{rx} = \frac{U_{m0}}{Z_w} \exp(-\gamma x) - \frac{U_{r0}}{Z_w} \exp(\gamma x) \quad , \quad (3.2b)$$

which can be determined by solving a second order differential equation (i.e. two solutions can be found, one with $\exp(-\gamma x)$ and one with $\exp(\gamma x)$) following from some simple considerations of the voltage and the current in the equivalent circuit. In the transmission line, the main wave which is produced by the signal generator is superimposed with a wave, being reflected at the resistance Z_2 . The amplitude of the main wave is subscripted by “m” while the amplitude of the reflected wave is subscripted by “r”. At the beginning of the transmission line ($x = 0$), the voltage amplitude is U_{m0} for the main wave and U_{r0} for the reflected wave, respectively. As can be seen in eqs. 3.2a and 3.2b, the amplitudes are attenuated with increasing length x . In the preceding text, it was mentioned that the TEM waveguide should be terminated with a 50Ω resistance at one end, in particular this means $Z_2 = 50 \Omega$, to avoid reflections. This can be easily understood by the following consideration. The voltage at the resistance Z_2 is $U_2 = I_2 Z_2$. It is a linear combination of the amplitude of the main wave and the reflected wave at $x = L$, i.e. $U_2 = U_{mL} + U_{rL}$ and $I_2 = U_{mL}/Z_w - U_{rL}/Z_w$, respectively. Substituting the equations into $U_2 = I_2 Z_2$ and solving for U_{rL} , following equation for the amplitude of the reflected wave can be determined

$$U_{rL} = U_{mL} \frac{Z_2 - Z_w}{Z_2 + Z_w} \quad . \quad (3.3)$$

If $Z_2 = Z_w$, the reflected wave vanishes. This method is called wave tuning and was also performed

with the TEM waveguide. The resistance Z_2 was chosen to be 50Ω . However, because of the same reason, inside the TEM waveguide volume also an impedance of the same value has to be reached as already described before.

The Magnetic RF Coil

With the magnetic rf coil, a magnetic rf field can be produced. The field amplitude can also be kept constant with the power-control method described above, although this is not necessary for magnetic dipole transitions which will be explained later. Within the limited time-frame of this thesis, it was not possible to produce and to test the magnetic rf coil. However, the design was completed (fig. 3.20). Two SMA connectors are attached to a copper box. Inside the box the rf coil is installed which consists of a silver-plated copper wire with 4.5 turns ($\varnothing = 1 \text{ mm}$), wrapped around a plastic tube in the copper box. The total height of the coil (outer edge to outer edge) is 10 mm while the diameter of the coil is 29.5 mm measured from the center of the wire. The metastable atomic beam passes the coil as sketched in fig. 3.21 and magnetic dipole transitions are induced. The magnetic rf-field vector oscillates parallel to the beam direction. Therefore, the external magnetic field, produced by the coil system (figs. 3.10 and 3.11), is perpendicular to the field vector of the rf field. As it is possible to induce selected electric dipole transitions with the TEM waveguide, it is similarly possible to induce selected magnetic dipole transitions with the magnetic rf coil because the dominating field is now a magnetic rf field.

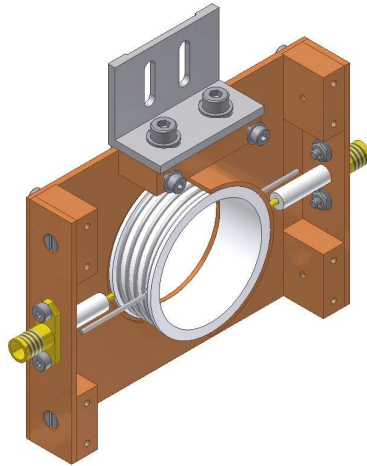


Figure 3.20: Design of the magnetic rf coil.

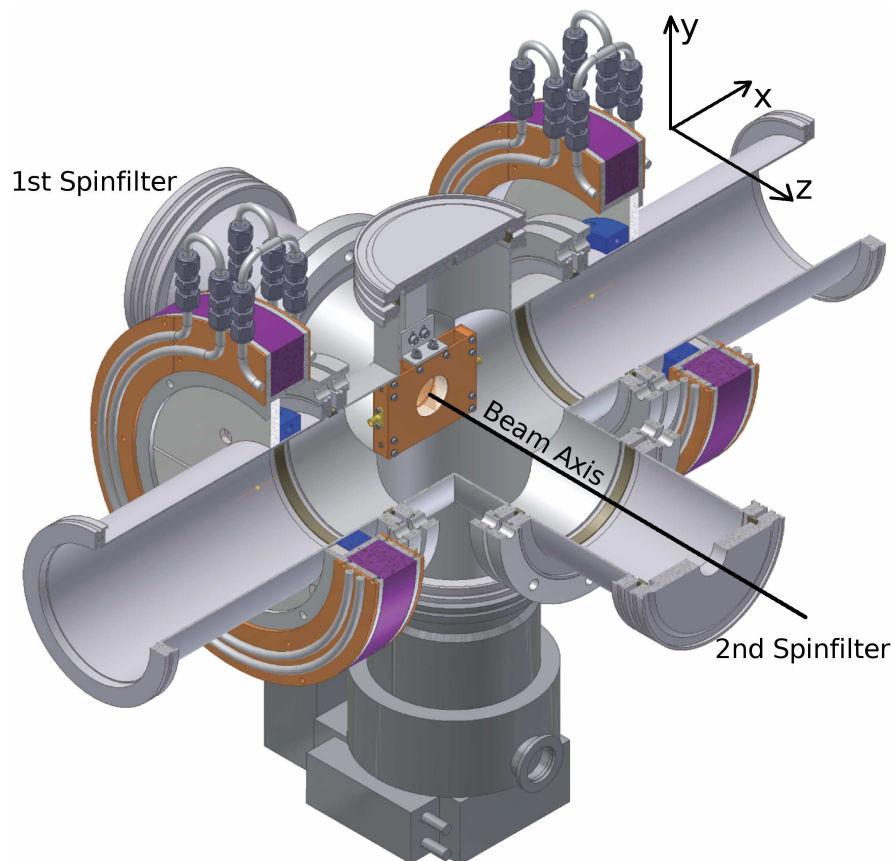


Figure 3.21: CAD design of the spectroscopy chamber with magnetic rf coil inserted (design by Maxim Mikirtychians (IKP-2)).

Calibration of the Coil System

The magnetic-field strength in x direction as function of the coil current was measured with a *Sentron AG C-H3A-xx* 3D Hall probe in the interaction region of the TEM waveguide to obtain a calibration for the coil system. The Hall probe was chosen because of its smallness and the quasi pointlike field sensitive region of only $0.15 \times 0.01 \times 0.15 \text{ mm}^3$ which allows a high spatial resolution of the magnetic-field measurement. Therefore, the shielding (fig. 3.5) was dismantled. At the present status of the experiment, measurements of atomic transitions in an external magnetic field are only possible without shielding against external sources of electromagnetic fields. This is due to the coil setup on the chamber where the shielding would completely distort the magnetic field of the coils. With a new chamber design (chap. 5) this can be changed.

For the calibration an one-dimensional map of the magnetic field was sufficient, so only the $y+$ port of the Hall probe was used (fig. 3.22). The Hall probe is connected to a magnetic-field transducer (*Sentron AG 3R-100-2*) with a sensitivity of 5 V/T and for the readout a *Keithley Multimeter 2000* was used. A special support shown in fig. 3.23(b) where the Hall probe can be inserted and which fits exactly into the hole where the

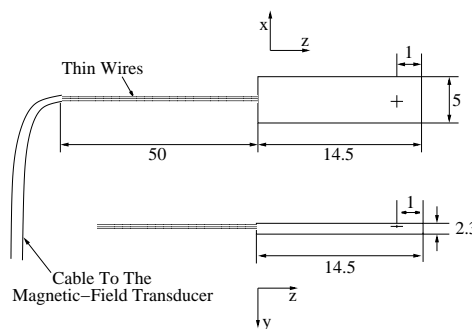


Figure 3.22: Sketch of the Hall probe. The cross denotes the field sensitive region. All measures are in millimeters.

atomic beam passes the TEM waveguide, could be additionally used to measure the magnetic-field strength as a function of the position (z direction) in the interaction region. Therefore, the whole support with the Hall probe at the front was installed in the experiment (fig. 3.23(b)). Furthermore, a computer simulation of the magnetic field was prepared and compared with the measurement. However, the experimental characterization turned out to be more reliable than the simulation as will become clear below. The Hall probe was calibrated inside a dipole magnet (fig. 3.23(a)) because of its large field homogeneity between the pole shoes. As reference, an already calibrated Hall probe and a nmr probe were used. Both the calibrated Hall probe and the nmr probe were used to cross-check the measured value for the magnetic field. For the calibration of the *Sentron AG C-H3A-xx* 3D Hall probe itself the nmr probe was not used, because the calibration was done at fields up to 180 G where the nmr probe does not work. The already calibrated Hall probe has an absolute uncertainty of

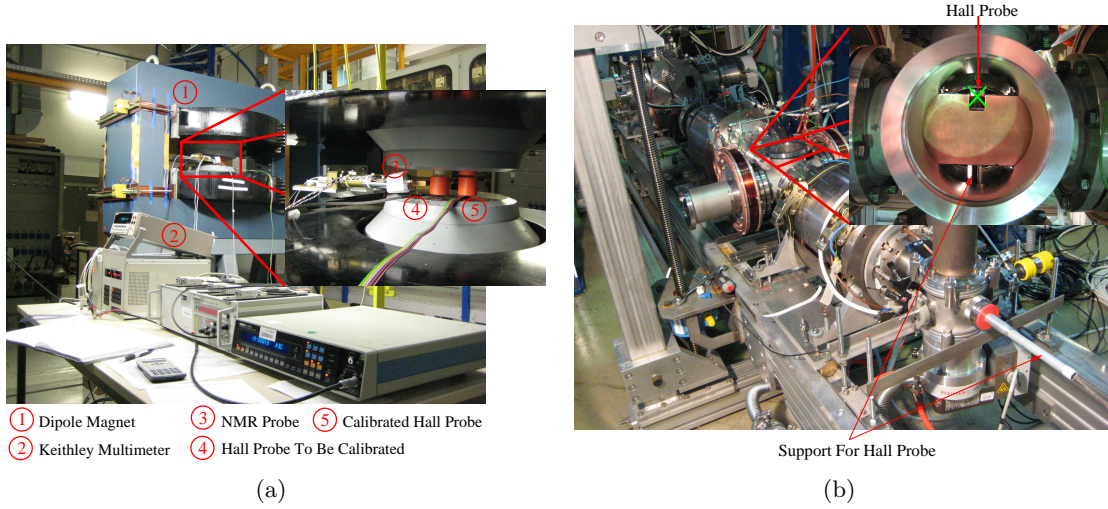


Figure 3.23: Calibration of the Hall probe (a) and the coil system of the modified LSP (b). In the magnified picture in (b), the green cross denotes the center of reference for the magnetic-field measurement in the interaction region to be explained later in the text.

1 G, whereas for small fields (≤ 100 G) the uncertainty seemed to be better (≈ 0.1 G). Fig. 3.24 shows the result of the calibration. Every value was averaged five times in twenty minutes to be aware of temperature fluctuations in the Keithley multimeter and the Hall probe itself. As calibration for the *Sentron AG C-H3A-xx* 3D Hall probe, following linear relation was deduced

$$B(U) = (3988.32 \pm 4.41) \frac{\text{G}}{\text{V}} \cdot U + (0.65 \pm 0.13) \text{ G} \quad . \quad (3.4)$$

The coil system was connected in series. Therefore, the coils produce the same magnetic field, because the current is the same in both coils. A round copper wire with a diameter of 1.6 mm was wrapped around an aluminum support. Every coil consists of 474 turns of the copper wire. Because only the geometry of the turns define the magnetic characteristic of the coil, in table 3.1 the measures of one coil without the support is summarized. The distance of the inner edge of each coil to the center of the interaction region of the TEM waveguide is $d' = 129.8$ mm. To obtain a sufficient magnetic-field homogeneity, a Helmholtz geometry of the coils has to be chosen, i.e. the

Table 3.1: Geometry of one coil without support, measures in millimeters.

Turns	Outer Radius	Inner Radius	Height
474	130	96	30

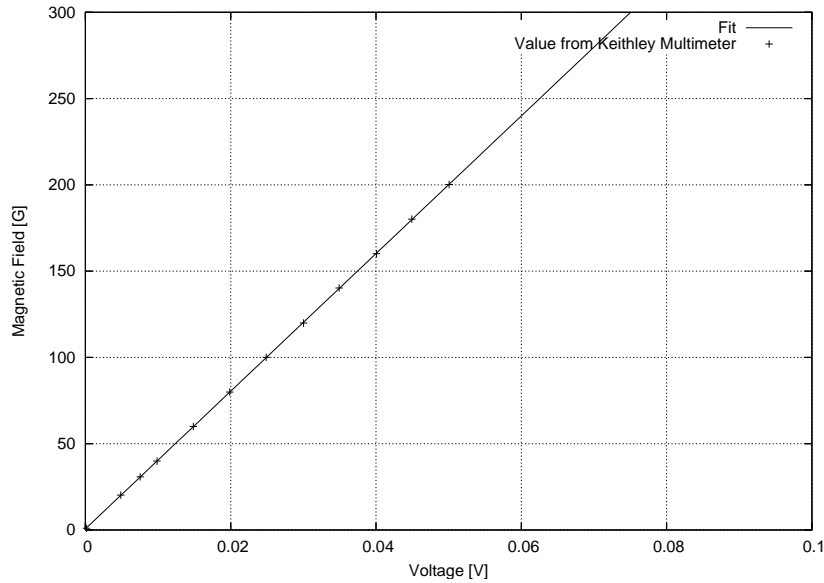


Figure 3.24: Calibration of the Sentron Hall probe.

distance between the coils has to be equal to their radius. The mean value of the coil radius is $\langle r_{Coil} \rangle = 113$ mm in contrast to the distance $d = 259.6$ mm between the coils. Because of the chamber geometry, it was not possible to assemble the coils closer to each other or to build coils with a bigger radius, so first tests had to be performed with a non-exact Helmholtz geometry of the coils. A first approximation of the field homogeneity of the coils was obtained with a computer simulation of the magnetic field which was prepared with the computer algebra system MAPLE (version 11). With this program the coil geometry was modeled (i.e. thickness of the wire, turns, inner radius, outer radius, thickness and pitch of the turn) and the application of the law of Biot-Savart for every point of the wire yielded the simulated magnetic field between the coil setup used in this thesis. On an *AMD Athlon XP 3000+* CPU running at 2 GHz on a *SuSE Linux 10.0* machine, the mean-computation time was approximately 40 min. The center of the coordinate system in the experiment was chosen to be the center of the interaction region of the TEM waveguide. In figs. 3.11, 3.14 and 3.15, respectively, the directions of the axes are defined. As an example, fig. 3.28 illustrates how the computer simulation calculates an one-dimensional map of the magnetic field as function of the coordinate z . Therefore, the intersection between the magnetic-field planes $x = 0$ and $y = 0$ has to be calculated. In figs. 3.25 and 3.26, respectively, the result of the simulation is shown. The metastable atomic beam passes a set of apertures $A_1 - A_4$ shown in fig. 3.2 where the holes inside A_1 and A_2 have a diameter of 15 mm and inside A_3 and A_4 a diameter of 10 mm. Thus the diameter of the atomic

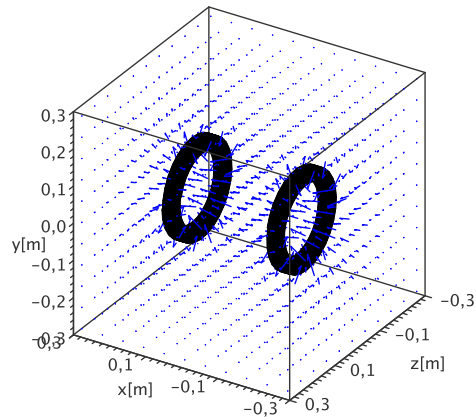


Figure 3.25: Computer simulation of the coil setup (black coils) of the modified LSP and 3D magnetic-field plot (blue arrows) for $I = 9.5$ A.

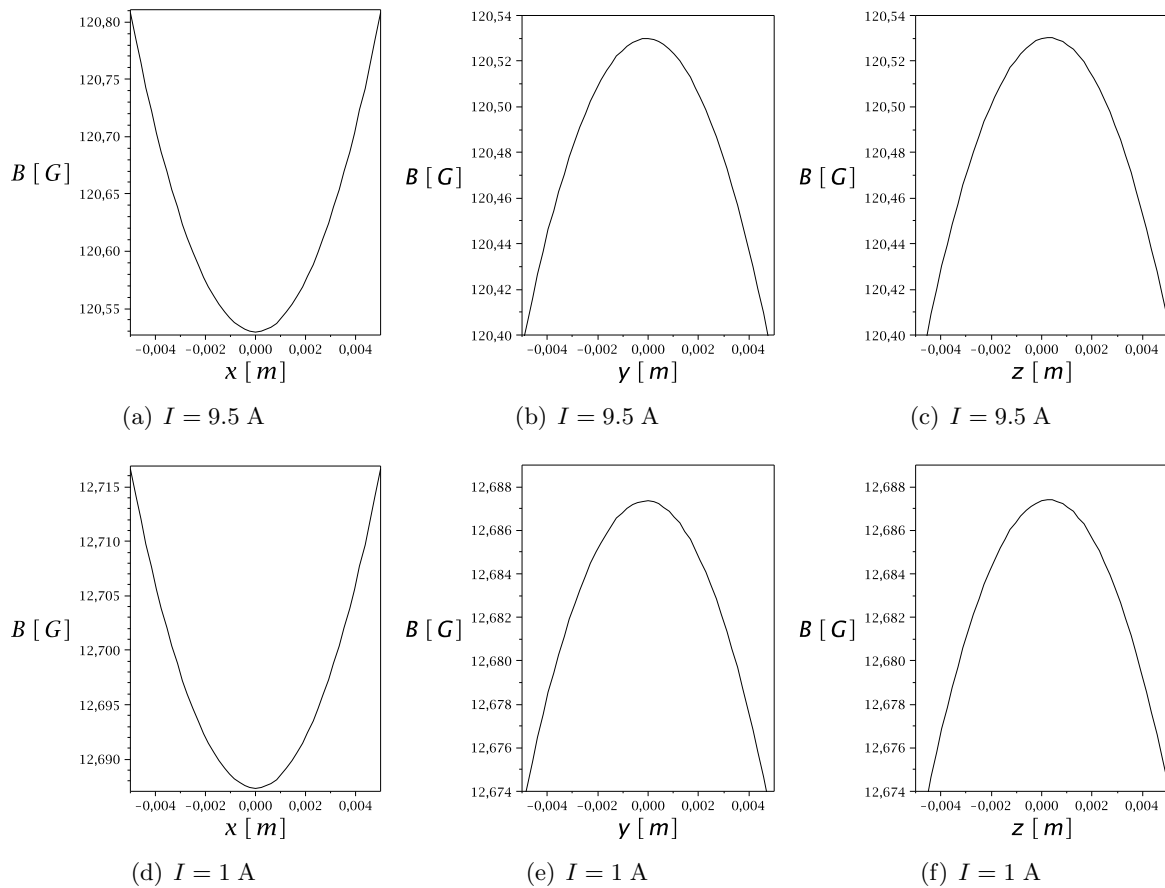


Figure 3.26: Computer simulation of the magnetic fields B_x , B_y and B_z inside the interaction region, I is the coil current.

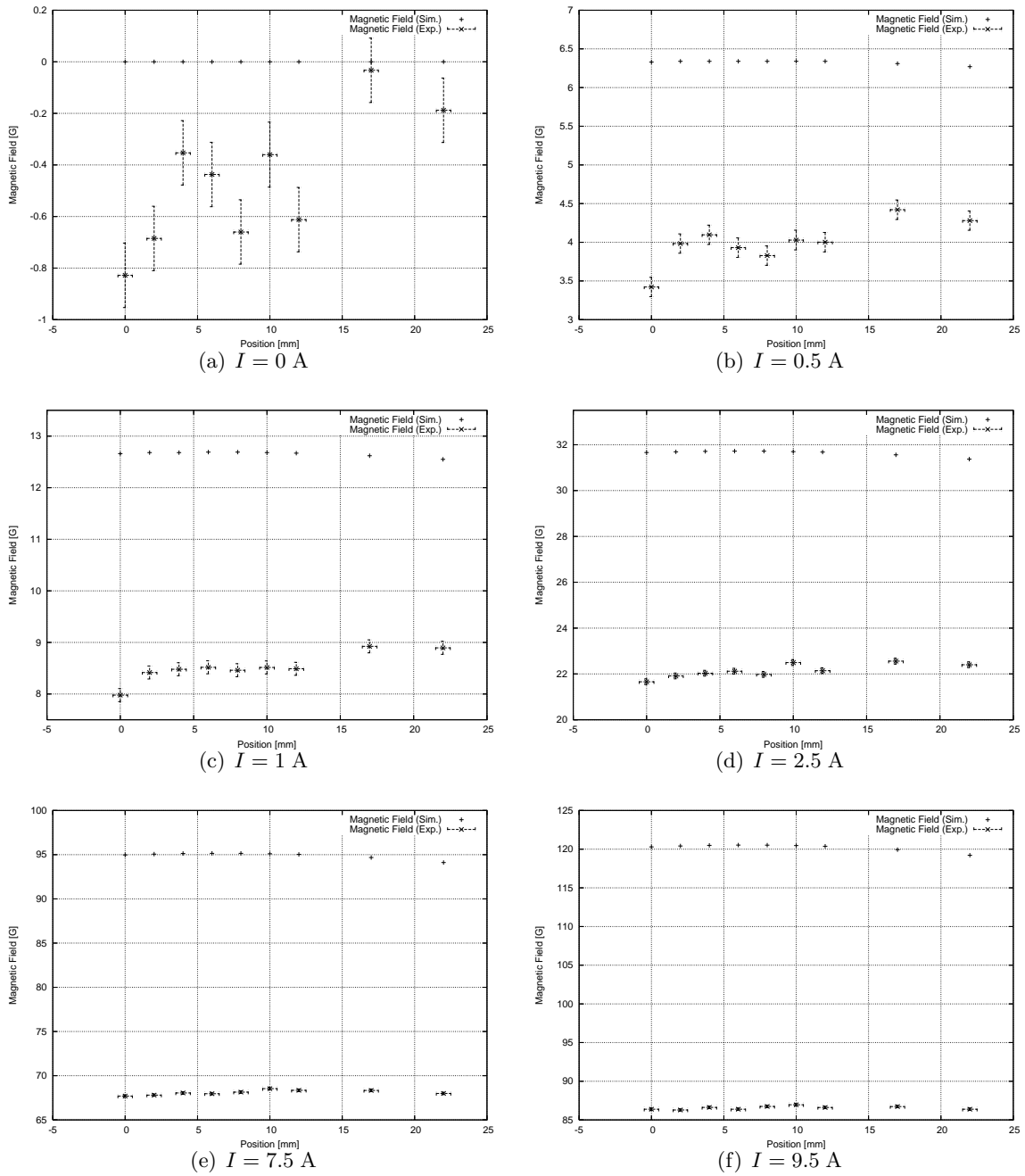


Figure 3.27: Selected experimental results of the magnetic-field measurement on the z axis inside the interaction region (region between 0 mm and 10 mm in the plots), I is the coil current. The magnetic field points along the x direction. For practical reasons, in this measurement only, the position 0 mm was defined as the outer edge of the outer conductor of the TEM waveguide indicated by the green cross in fig. 3.23(b).

beam is not expected to exceed a diameter of 10 mm. From the computer simulation, therefore, a magnetic-field inhomogeneity at a current of $I = 9.5$ A of ± 0.14 G in x direction and of ± 0.07 G in y and z direction can be calculated. For a lower current of $I = 1$ A, a smaller inhomogeneity of ± 0.02 G in x direction and of ± 0.01 G in y and z direction can be obtained. Comparing the simulation with the measurement of the magnetic field inside the interaction region, the influence of the chamber and the TEM waveguide on the magnetic-field homogeneity can be determined which were not included in the simulation (fig. 3.27).

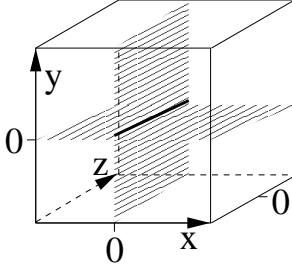


Figure 3.28: Sketch of a volume inside the TEM waveguide. Example of volume cuts to determine the magnetic field B_z like it is calculated in the computer simulation.

As can be seen, the chamber expectedly attenuates the magnetic field produced by the coils, so from the simulation always a higher value of the magnetic-field strength is obtained. Furthermore, the field homogeneity in the interaction region is distorted, especially at small magnetic fields. A non-vanishing magnetic field was measured for $I = 0$, due to the remanence of the stainless steel chamber and other influences (sec. 4.2). For $I > 0$, the magnetic field changes the sign as can be seen in fig. 3.27. Differences in the magnetic-field strength over the length of the interaction region of up to ± 0.5 G were measured. Although the simulation describes the tendency of the magnetic field in the interaction region sufficiently well, outside

the interaction region field inhomogeneities increase. This is another indication for a residual magnetization of the chamber. For the comparison of theory and experiment of the measurements to be presented in the further text, a mean field value for the magnetic field in the interaction region was calculated.

3.2.9 The Quench Chamber

The quench chamber consists of an ISO-K 100 tube with two LASKA flanges in beam direction (fig. 3.1). In the tube, an electrostatic lens can be fixed, consisting of two grounded cylinders $T1$ and $T2$ at the flanges of the chamber and a ring R in-between on the potential ϕ , fixed in a plastic tube, i.e. electrically separated from the grounded cylinders (fig: 3.29). At the bottom part of the tube a turbo drag pump is attached, and on the top a photomultiplier. The electrostatic lens is used to produce a longitudinal electric field on the beam axis in which metastable atoms in the $2S_{1/2}$ state are quenched to the ground state via the $2P_{1/2}$ state by emitting ultraviolet light which is detected by the photomultiplier on top of the chamber. In a distance of 2 cm an electric field of about 100 V/cm between the grounded cylinder $T1$ and the ring R is able to quench

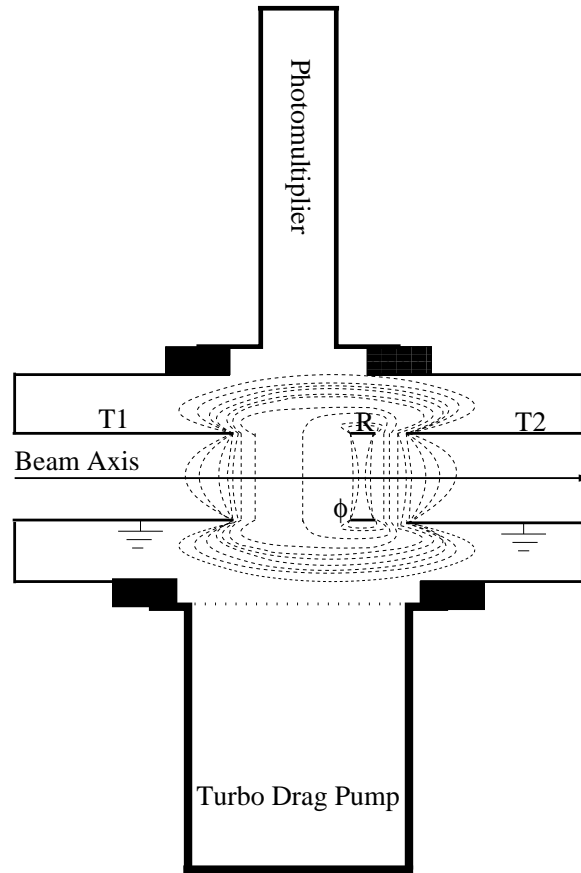


Figure 3.29: Sketch of the cross section through the quench chamber. Dashed lines designate equipotential surfaces. According to the relation $\mathcal{E} = -\mathbf{grad}\phi$, the electric field is always perpendicular to them.

about 48 % of the metastable atoms from the $2S_{1/2}$ state into the ground state. A larger electric field leads to a decrease of the quench signal! Stronger electric fields also penetrate the cylinder $T1$ in a stronger way. Therefore, metastable atoms are quenched into the ground state before they reach the field of view of the photomultiplier.

3.3 Operation Modes of the modified Lamb-shift Polarimeter

3.3.1 Measurement of Electric Dipole Transitions

For the measurement of electric dipole transitions, all devices of the experiment are needed except the second spinfilter and the quench chamber. Furthermore, the TEM waveguide has to be installed into the spectroscopy chamber to induce electric dipole transitions. With this setup the measurement of the classical Lamb shift can be performed to test BSQED. Further on, electric dipole transitions as function of an external

magnetic field can also be measured to test recent calculations of the Breit-Rabi diagrams also connected to BSQED (fig. 2.16(a) - 2.16(b)). A new method to determine for the first time the $2P_{1/2}$ hfs experimentally can also be carried out.

With the modified LSP described in the previous section, a metastable beam of hydrogen atoms in the $2S_{1/2}$ state is produced. A beam flux of up to $7 \cdot 10^{10}$ atoms/s was obtained. The spinfilter is tuned to transmit metastable hydrogen atoms in the state α_1 or α_2 to measure electric dipole transitions with the TEM waveguide in the spectroscopy chamber. As described in subsec. 3.2.8, the external magnetic field is perpendicular to the electric rf-field vector in the TEM waveguide and in order to that, selected transitions can be induced according to the selection rules of quantum mechanics. As already mentioned in sec. 2.3, the external magnetic field influences the line strength of atomic transitions. This can be understood as follows.

First of all, the natural line width of an electric dipole transition from the $2S_{1/2}$ state into the $2P_{1/2}$ state with a subsequent decay into the ground state is of the order of 100 MHz due to the short lifetime of the $2P_{1/2}$ state of only $1.6 \cdot 10^{-9}$ s. Doppler broadening due to different velocity components of the atoms in the beam (Maxwell velocity distribution) does not have to be considered, because the energy of the atomic beam is defined with the potential $E3$ in the ionizer. The velocity is only straggled approximately by an amount of 1 % behind the cesium cell after the charge exchange reaction (scattering effects), nevertheless, it is expected to have vanishing influences on the spectra. However, Doppler broadening as well as Doppler shifting has to be considered because of the possibility of a slightly divergent and misaligned beam. A

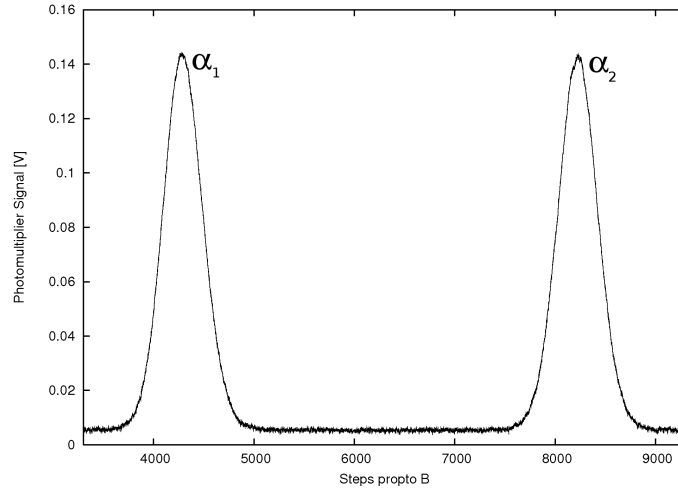


Figure 3.30: Lyman- α spectrum of the metastable hydrogen beam behind the first spinfilter as function of the solenoid magnetic field of the spinfilter. The Zeeman components α_1 and α_2 are separated, i.e. a polarized atomic beam can be produced.

more precise treatment of this topic can be found in chap. 4 where also all other uncertainties of the transition frequency of an electric dipole transition are summarized.

Because of this, a Lorentz shape as line profile can be expected with a FWHM equal to the natural line width. Producing for example a metastable hydrogen beam in the state $\alpha_1 = |1/2, 1/2\rangle$, according to the selection rules of quantum mechanics, transitions into the e_2 and f_4 state can be observed in a magnetic field perpendicular to the electric rf-field vector. The strength of each transition depends on the strength of the external magnetic field. In fig. 2.16(b) is illustrated that in a strong magnetic field the transition into the e_2 state cannot be observed anymore. This is easy to understand by looking back to eq. 2.44. In a strong magnetic field, the critical field parameter $a(B_{0,z})$ converges to zero. Therefore, in the mixed state e_2 , the quantum mechanical state $|-1/2, 1/2\rangle$ vanishes. An electric dipole transition into this state is no longer possible. Compared to this, in the mixed state f_4 the quantum mechanical state $|1/2, -1/2\rangle$ vanishes while the state $|-1/2, 1/2\rangle$ survives, so an electric dipole transition is further possible. Therefore, with increasing external magnetic field, a transition into the state e_2 is getting more improbable. In the case of σ transitions starting from the α_1 state in the metastable hydrogen atom, the peak ratios of the corresponding line shapes can be described by following formulas

$$\frac{1}{2} \left[1 - a_{2P_{1/2}}(B_{0,z}) \right] \quad : \alpha_1 \rightarrow e_2 \quad , \quad (3.5a)$$

$$\frac{1}{2} \left[1 + a_{2P_{1/2}}(B_{0,z}) \right] \quad : \alpha_1 \rightarrow f_4 \quad . \quad (3.5b)$$

Here $a_{2P_{1/2}}(B_{0,z})$ is the critical field parameter of the $2P_{1/2}$ state which has to be chosen because the initial state is pure and metastable while the mixed final states are in the unstable $2P_{1/2}$ state. For σ transitions starting from the α_2 state, transitions into e_1 and f_3 can be observed. The peak ratios can be written as

$$\frac{1}{2} \left[1 - a_{2S_{1/2}}(B_{0,z}) \right] \quad : \alpha_2 \rightarrow e_1 \quad , \quad (3.6a)$$

$$\frac{1}{2} \left[1 + a_{2S_{1/2}}(B_{0,z}) \right] \quad : \alpha_2 \rightarrow f_3 \quad . \quad (3.6b)$$

In this case, the critical field parameter of the $2S_{1/2}$ state has to be chosen, because the initial state is mixed while the final states are pure. Because of the line width of 100 MHz, single transitions cannot be observed separately, only the sum. However, within a first test it was possible to measure different peak shapes which could be assigned to different transitions. For σ transitions starting from the state α_1 and α_2 , respectively, peak shape simulations are shown in figs. 3.31 and 3.32. The transition frequencies were calculated with the Breit-Rabi formula (subsec. 2.2.1) while the peak

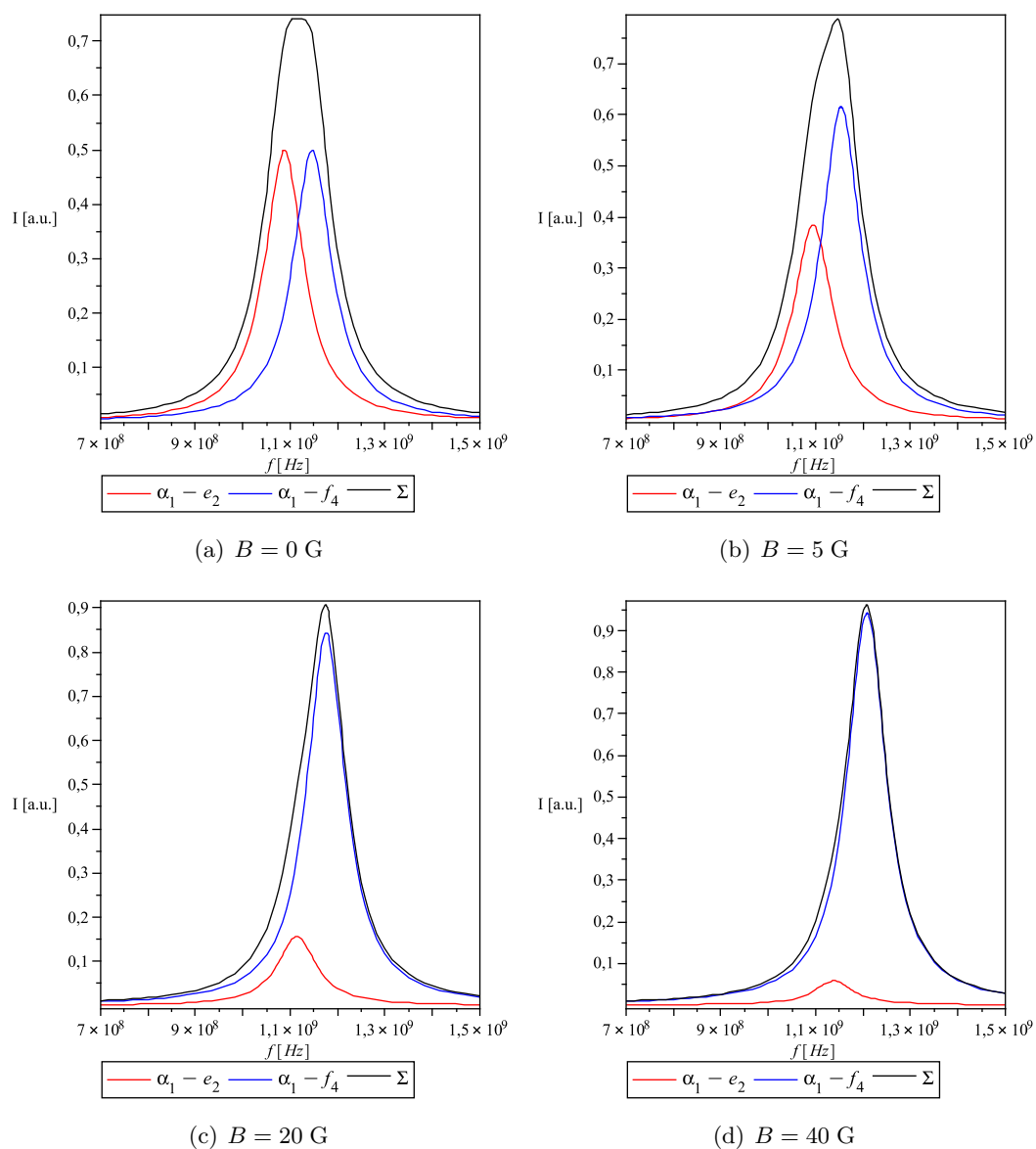


Figure 3.31: Peak shape simulation for electric dipole transitions (σ transitions) starting from the α_1 state in hydrogen for different values of the external magnetic field. The measured (sum)peak is similar to the black colored plot.

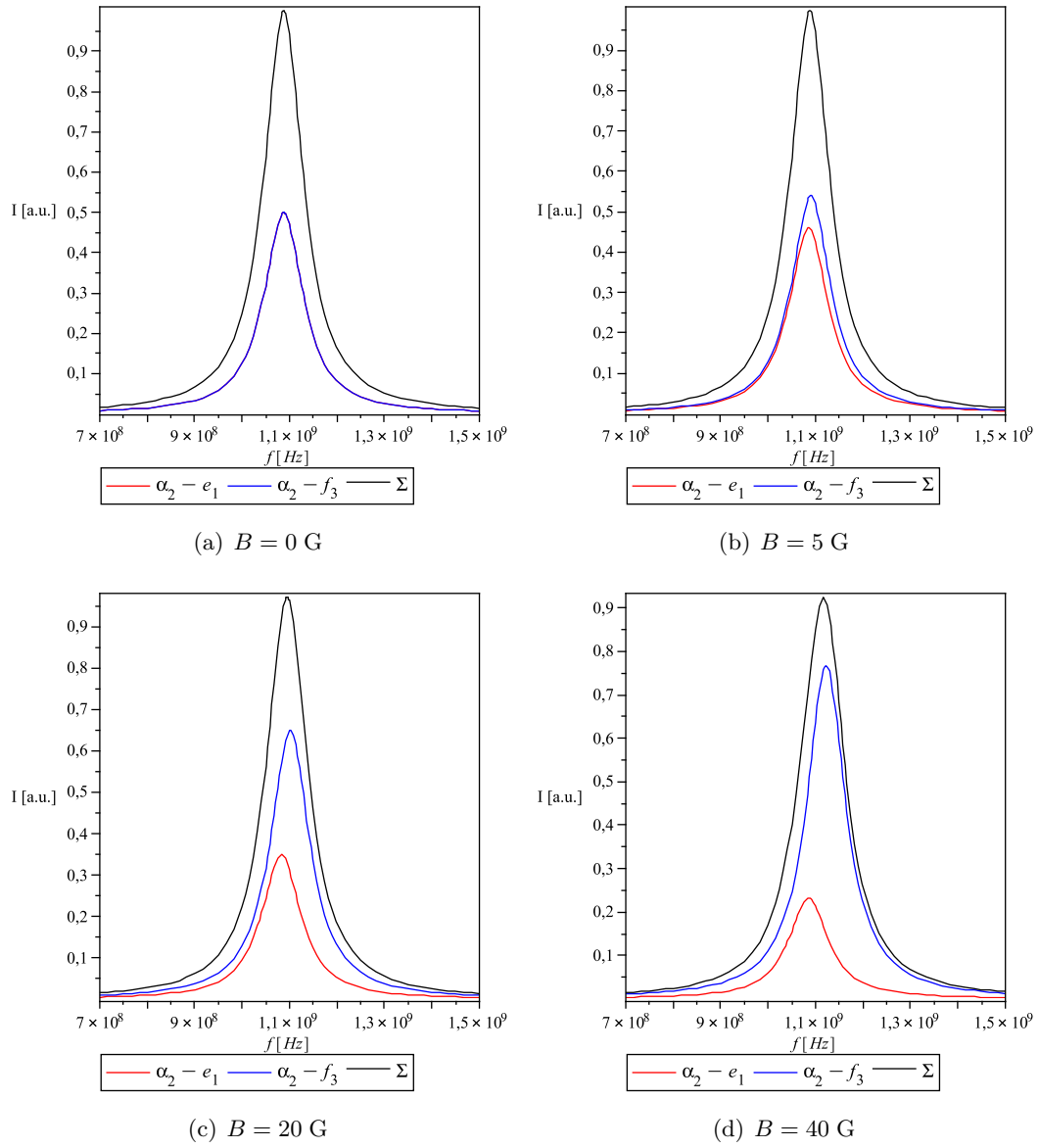


Figure 3.32: Peak shape simulation for electric dipole transitions (σ transitions) starting from the α_2 state in hydrogen for different values of the external magnetic field. The measured (sum)peak is similar to the black colored plot. In (a) the red and the blue colored resonance shape are indistinguishable.

ratios were calculated with eqs. 3.5 and 3.6. As can be seen in fig. 3.31, for increasing magnetic field, transitions from the state α_1 into the e_2 state get more improbable while transitions into the f_4 state can be further observed. An analogous situation can be found in the case of σ transitions starting from the α_2 state (fig. 3.32). Especially in this case it can be noticed, that transitions from the α_2 into the e_1 state decrease slower with increasing magnetic field as transitions from the α_1 into the e_2 state. This is due to the different critical field parameters for the $2S_{1/2}$ and the $2P_{1/2}$ state! The measured resonance is similar to the black colored plot. From first measurements, different peak shapes for different transitions were obtained which agree with the theoretical expectation (chap. 4). Taking into account the theoretical expectation of the evolution of the single transitions as function of the external magnetic field, a fit to the measured resonance was performed.

The frequency difference of the transitions $\alpha_1 \rightarrow e_2$ and $\alpha_1 \rightarrow f_4$ at vanishing external magnetic field allows for the first time to determine an experimental value of the $2P_{1/2}$ hfs.

In the framework of a first test, the transitions shown in fig. 2.16(b) were measured which are proportional to the Breit-Rabi diagrams.

The principle of the measurement of the classical Lamb shift was also verified, but for this kind of measurement, π transitions are more suitable. As can be seen in fig. 2.16(a) there exists only one transition starting from the α_1 state for $\mathbf{B}_0 \parallel \mathbf{E}$. With the knowledge of the $2S_{1/2}$ and the $2P_{1/2}$ hfs, the classical Lamb shift, therefore, can be determined precisely.

3.3.2 Measurement of Magnetic Dipole Transitions

For the measurement of magnetic dipole transitions all devices of the modified LSP are needed, including the second spinfilter and the quench chamber. Furthermore, the TEM waveguide has to be exchanged against the magnetic rf coil (subsec. 3.2.8). In an external magnetic field which is perpendicular to the magnetic rf-field vector, in metastable hydrogen atoms the π transitions $\alpha_1 \rightarrow \alpha_2$, $\alpha_1 \rightarrow \beta_4$ and $\alpha_2 \rightarrow \beta_3$ can be observed. In a longitudinal field only the σ transition $\alpha_2 \rightarrow \beta_4$ can occur. Magnetic dipole transitions cannot be observed with the photomultiplier directly as in the case of electric dipole transitions. The wavelength is too large (i.e. the quantum energy too low) and the photomultiplier is no longer sensitive to this wavelength region. Therefore, the second spinfilter has to be used to check the occurrence of a transition indirectly with the quench chamber behind the second spinfilter as described below. A crucial difference to electric dipole transitions into the $2P_{1/2}$ state is, that transitions within the $2S_{1/2}$ state, i.e. magnetic dipole transitions, have a much narrower resonance shape due to the metastability of the $2S_{1/2}$ state. Each transition is expected to

have a FWHM of the order of kHz with all influences included (natural line width ≈ 1.2 Hz, Doppler broadening < 40 kHz, magnetic-field inhomogeneities (present coil configuration) ≈ 600 kHz). This means, that each transition can be separated and peak shape simulations as shown in the last subsection are not needed to interpret the spectra. Furthermore, because of the sharp linewidth, power controlling is not needed like performed for electric dipole transitions. During a transition, variations in the power amplitude have weaker influences on a spectrum with a sharp linewidth because they are expected to occur on a large frequency interval compared to the linewidth of a magnetic dipole transition.

$\alpha_1 \rightarrow \alpha_2$ Transitions

The occurrence of this sort of transitions is easy to check with the second spinfilter and the quench chamber. Metastable hydrogen atoms in the α_1 state, selected by the first spinfilter, interact with the magnetic rf field produced by the rf coil in the spectroscopy chamber. At frequencies equal to the spacing of the states α_1 and α_2 , transitions from the α_1 state into the α_2 state occur. Allowing only atoms in the α_2 state to pass the second spinfilter, the flux of α_2 atoms behind the second spinfilter has to increase in the resonance case. This can be checked with the quench chamber. Here, as already described above, a static electric field reduces the lifetime of metastable atoms in the $2S_{1/2}$ state. With α_2 atoms in the beam, a quench signal can be detected with the small photomultiplier on top of the quench chamber which increases in the resonance case.

$\alpha_1 \rightarrow \beta_4$ Transitions

To check the occurrence of $\alpha_1 \rightarrow \beta_4$ transitions, the electric-field configuration of the second spinfilter has to be changed. First of all, the second spinfilter is tuned to allow atoms in the α_1 state to pass through the spinfilter. During a transition of atoms in the state α_1 into the β_4 state, a decreasing flux of α_1 atoms can be measured behind the second spinfilter with the quench chamber. To ensure that a transition into the β_4 state occurred, the electric potential of the small quadrant at the entry of the second spinfilter is switched off. E.g. at a frequency where the probability for the transition $\alpha_1 \rightarrow \beta_4$ is large, the flux of atoms in the α_1 state behind the second spinfilter has to increase again. The small quadrant at the entry of the device does not quench atoms in the β_4 state into the ground state anymore. Inside the cavity in a magnetic field of approximately 538 G, the atoms start to oscillate between the states α_1 and β_4 , so the state α_1 is filled again and an increasing flux of atoms in the α_1 state behind the second spinfilter can be measured in the quench chamber.

$\alpha_2 \rightarrow \beta_3$ Transitions

For transitions of this kind, the same concept like described above can be applied to check their occurrence. Metastable atoms in the α_2 state selected by the first spinfilter interact with the magnetic rf field of the rf coil in the spectroscopy chamber. The second spinfilter is tuned to allow atoms in the state α_2 to pass through the spinfilter. During a transition into the β_3 state, the flux of α_2 atoms behind the second spinfilter decreases. To ensure that such a transition occurred, again the electric potential at the small quadrant at the entry of the second spinfilter is switched off. At a frequency where the probability for the transition $\alpha_2 \rightarrow \beta_3$ is large, the flux of atoms in the α_2 state behind the second spinfilter has to increase again. Inside the cavity, this time in a magnetic field of approximately 605 G, the atoms start to oscillate between the states α_2 and β_3 , so the state α_2 is filled again and an increasing flux of atoms in the α_2 state behind the second spinfilter can be measured.

$\alpha_2 \rightarrow \beta_4$ Transitions

The concept to check the occurrence of $\alpha_2 \rightarrow \beta_4$ transitions differs slightly from the concept presented above, although the basic idea is the same. Atoms in the α_2 state, selected by the first spinfilter, enter the magnetic rf coil where transitions into the β_4 state can be induced at a specific frequency. Tuning the second spinfilter to allow atoms in the state α_2 to pass through the second spinfilter, during a transition into the β_4 state, a decreasing flux of α_2 atoms can be measured behind the second spinfilter. To ensure the occurrence of these transitions, the second spinfilter is tuned to allow atoms in the state α_1 to pass through the spinfilter and the small quadrant at the entry of the device is switched off. If a transition into the β_4 state occurred, atoms in the state β_4 enter the second spinfilter without being quenched into the ground state and start to oscillate between the states α_1 and β_4 . The state α_1 is filled and an increasing flux of atoms in the α_1 state can be measured behind the second spinfilter in the spectroscopy chamber.

Important Applications

With the methods described above, the transitions shown in fig. 2.16(c) - 2.16(d) can be measured and recent Breit-Rabi formula calculations can be tested. Besides this already important application, a much more striking measurement can be performed with this method. The measurement of the $\alpha_1 \rightarrow \beta_4$ and the $\alpha_2 \rightarrow \beta_3$ transition in an arbitrary external magnetic field allows to determine the $2S_{1/2}$ hfs. This can be shown in a simple treatment of the Breit-Rabi formula. Subtracting the frequency determined from the transition $\alpha_1 \rightarrow \beta_4$ from the frequency determined from the transition $\alpha_2 \rightarrow \beta_3$

Table 3.2: Summary of the use of the modified LSP to measure magnetic dipole transitions. The symbol \nearrow means, that the photomultiplier signal increases while the symbol \searrow implies that the signal decreases. The columns “1st Spinfilter” and “2nd Spinfilter” contain the states which are selected by the spinfilter and allowed to pass the other spinfilter.

1st Spinfilter	Transition	Small Quadrant (Entry 2nd Spinfilter)	2nd Spinfilter	Signal of Small Photomultiplier
α_1	$\alpha_1 \rightarrow \alpha_2$	ON	α_2	\nearrow
α_1	$\alpha_1 \rightarrow \beta_4$	ON	α_1	\searrow
α_1	$\alpha_1 \rightarrow \beta_4$	OFF	α_1	\nearrow
α_2	$\alpha_2 \rightarrow \beta_3$	ON	α_2	\searrow
α_2	$\alpha_2 \rightarrow \beta_3$	OFF	α_2	\nearrow
α_2	$\alpha_2 \rightarrow \beta_4$	ON	α_2	\searrow
α_2	$\alpha_2 \rightarrow \beta_4$	OFF	α_1	\nearrow

at the same but arbitrary magnetic field, always the same frequency value is obtained, the $2S_{1/2}$ hfs.

In laser spectroscopy the $1S_{1/2} - 2S_{1/2}$ resonance (in particular the $|1S_{1/2}, F = 0, m_F = 0\rangle \rightarrow |2S_{1/2}, F = 1, m_F = 0\rangle$ and the $|1S_{1/2}, F = 1, m_F = 0\rangle \rightarrow |2S_{1/2}, F = 0, m_F = 0\rangle$ resonance) is used to determine a value of the $2S_{1/2}$ hfs. A very small magnetic field has to be applied which defines the quantization axis and which allows the separation of the $m_F = 0$ Zeeman states. To obtain a value for the $2S_{1/2}$ hfs the transition frequencies have to be extrapolated to vanishing magnetic field.

Therefore, the method presented in the previous text could provide the perhaps most precise determination of the $2S_{1/2}$ hfs ever tried in physics!

CHAPTER 4

FIRST MEASUREMENTS

4.1 Uncertainties of Electric Dipole Transition Frequencies

4.1.1 Doppler Shift

As sketched in fig. 4.1, the atomic beam may have a slightly divergent shape. This means that velocity components v_x of atoms in direction of the wave vector $\mathbf{k} = k_x$ (i.e. the propagation direction of the electromagnetic wave in the TEM waveguide) exist, which lead to a Doppler shift of the transition frequency. I.e. the frequency from the signal generator, connected to the TEM waveguide and which is used to find resonances within the atom, is too large or too small compared with the uninfluenced transition frequency, depending on the relative velocity component of the atomic beam with respect to the wave vector. The amount of the frequency shift can be estimated, because the apertures A_3 and A_4 limit the divergence of the atomic beam until it reaches the interaction region of the TEM waveguide. The longitudinal Doppler effect for a source (the atom) moving away from the observer (the TEM waveguide) is given as

$$f'_L = f_0 \left(\frac{1 - \frac{v_x}{c}}{1 + \frac{v_x}{c}} \right) \approx f_0 \left(1 - \frac{v_x}{c} + \frac{1}{2} \frac{v_x^2}{c^2} + \dots \right) , \quad (4.1)$$

if a source is approaching the observer, this changes the frequency according to

$$f''_L = f_0 \left(\frac{1 + \frac{v_x}{c}}{1 - \frac{v_x}{c}} \right) \approx f_0 \left(1 + \frac{v_x}{c} + \frac{1}{2} \frac{v_x^2}{c^2} + \dots \right) . \quad (4.2)$$

The expression after the \approx -sign is an approximation valid for $\frac{v_x}{c} \ll 1$. The term proportional to v_x^2 is the relativistic Doppler effect.

Because of the finiteness and the constancy of the velocity of light and the time dilatation in fast moving inertial frames, the transversal Doppler effect can be observed

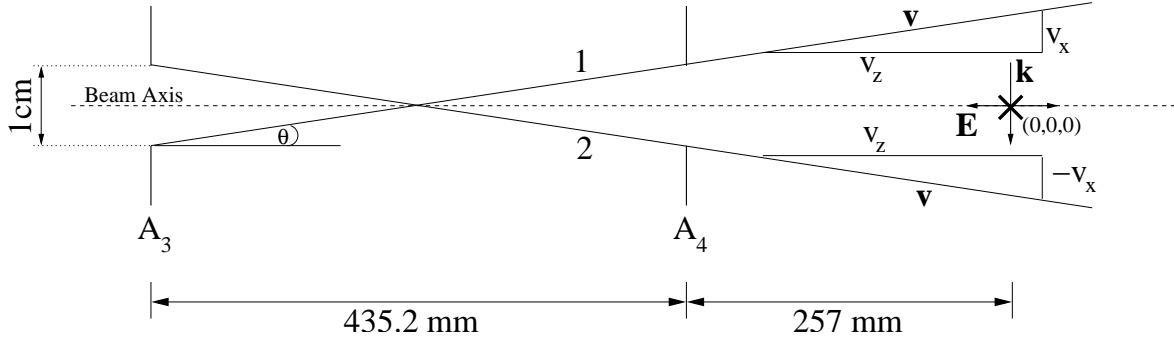


Figure 4.1: Sketch of the apertures in the first spinfilter (fig. 3.2) and the approximate position of the interaction region (bold black cross). The lines “1” and “2” are extremal trajectories of the atomic beam. To illustrate the source of the Doppler shift, the wave vector \mathbf{k} (the electric rf-field vector is perpendicular to the wave vector) is added to the sketch. It is parallel to the velocity component v_x of the slightly divergent atomic beam and leads to the well-known longitudinal Doppler effect. The transversal Doppler effect originates from the velocity component v_z and is a purely relativistic effect which can be observed perpendicular to the propagation of the source.

perpendicular to the propagation of the source. It reads as

$$f'_T = f_0 \left(1 - \frac{v_z^2}{c^2} \right) . \quad (4.3)$$

This is a purely relativistic effect. The velocity of the atomic beam defined by the ionizer potential $E3$ is $v = 4.378 \cdot 10^5$ m/s. A maximum divergence of the atomic beam from truly parallel trajectories due to the geometry of the apertures is $\theta \approx 1.32^\circ$. From this angle, the velocity components v_x and v_z of the atomic beam can be calculated to be $v_x = 1.006 \cdot 10^4$ m/s and $v_z = 4.376 \cdot 10^5$ m/s. As a consequence, an uncertainty of $\pm 0.004\%$ in the transition frequency due to the longitudinal Doppler effect has to be considered. The transversal Doppler effect affects the frequency by -0.0003% ¹.

Doppler shifting, except the relativistic Doppler effect, can be eliminated by reversing the direction of rf irradiation (connect the signal generator to the other side of the TEM waveguide). In this case, the wave vector is also reversed and the frequency of a specific transition can be calculated by averaging the value of the transition frequencies obtained during rf irradiation from both sides of the TEM waveguide. The relativistic and the transversal Doppler effect can be eliminated by measuring transition frequen-

¹Obviously, the transversal Doppler effect lowers the observed transition frequency. This is easy to understand with the basic axioms of special relativity. In a moving frame, time goes by slower than in the rest frame. Therefore, an observer perpendicular to the moving source measures a lower emitted frequency than this is the case in the rest frame (this means that a lower frequency has to be irradiated by the signal generator into the TEM waveguide to induce a transition). In addition a geometrical aspect can also explain the transversal Doppler effect and is due to the constancy of the velocity of light. A very similar effect can be observed in astronomy in the aberration of light.

cies at different beam energies. In this case these effects vary and can be extrapolated to zero beam energy.

Although the transition frequency is not changed by Doppler broadening, this effect should also be mentioned. As already stated, the velocity components of the metastable atomic beam are discrete and defined by the ionizer potential $E3$. However, Doppler broadening can be observed because of two effects. As already mentioned energy straggling behind the cesium cell is expected to lead to a small amount of Doppler broadening. Further on, assuming that the same amount of atoms follow the trajectories “1” and “2” (fig. 4.1), Doppler broadening can be observed and be estimated with the same calculation as performed for the shifting. Another effect which leads to a line broadening is explained in subsec. 4.1.3.

4.1.2 Magnetic Field Inhomogeneities and Residual Magnetic Fields

As already mentioned in subsec. 3.2.8, the maximal absolute uncertainty of the external magnetic field produced by the coil system is ± 0.5 G. This uncertainty has to be translated into a frequency by using the Breit-Rabi formula for a specific transition.

In addition residual magnetic fields in the spectroscopy chamber with arbitrary directions distort the spectra. At the same time σ and π transitions with different strength can be observed leading also to an uncertainty (sec. 4.2.2).

4.1.3 Power Fluctuations

Without controlling the power behind the TEM waveguide, spectra of the kind like shown in fig. 4.2 are obtained. Obviously, the varying power distorts the spectrum because the transition probability of an electric dipole transition is proportional to the power of the electric rf field as already mentioned in subsec. 3.2.8. A precise determination of the transition frequency is not possible. Compared to this, spectra where the power was controlled with a powermeter behind the TEM waveguide (e.g. fig.4.3) are smoother and less variations in the spectrum are visible. With the powermeter used in this thesis, the power was controlled on a 3% level. The uncertainty on the transition frequency due to power variations is difficult to estimate, because of the dependence on the specific transition. However, it is expected to be in the order of 100 kHz up to 1 MHz.

Another source of line shape broadening, in addition to the Doppler broadening, is the power saturation and can be observed if the power of the electromagnetic wave irradiated into the TEM waveguide exceeds a certain limit. Increasing the power, also the transition probability can be increased but the line shape is broadened, too.

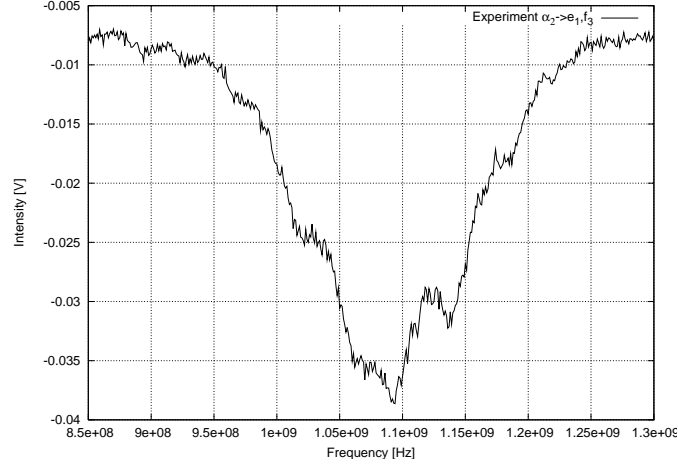


Figure 4.2: Transition spectrum of the $\alpha_2 \rightarrow e_1, f_3$ resonance at $B \approx 0$ G without controlling the power behind the TEM waveguide (power of the electric rf field, approximately 1 W). Clearly visible variations in the spectrum were observed.

4.1.4 Electric Fields

As mentioned in sec. 2.4 external electric fields influence the transition frequencies very similar to the Zeeman effect. In the limited time-frame of this thesis it was not possible to calculate the Stark effect on the single Zeeman components in a fully quantum mechanical treatment although the concept was briefly presented. A very first approximation, anyhow, can be given for the $2S_{1/2}$ state. The frequency which separates the $F = 0$ from the $F = 1$ state changes in an electric field \mathcal{E} approximately like $1000 \mathcal{E}^2 \text{Hz}(\text{cm}/\text{V})^2$. This means, in an electric field of 1 V/cm, the $2S_{1/2}$ hfs is increased by approximately 1 kHz. For a precise and full treatment of every state including the Zeeman components, the complete Stark Hamiltonian has to be calculated.

4.1.5 Motional Stark Effect

The motional Stark effect occurs while atoms with a velocity \mathbf{v} traverse a magnetic field \mathbf{B} which is perpendicular to the propagation axis of the atoms. According to special relativity, in the moving frame of the atom an electric field is produced:

$$\mathcal{E} = \mathbf{v} \times \mathbf{B} \quad . \quad (4.4)$$

In the present coil configuration where $\mathbf{v} \perp \mathbf{B}$, this effect has to be mentioned, while in a longitudinal magnetic-field configuration ($\mathbf{v} \parallel \mathbf{B}$ and, therefore, $\mathbf{v} \times \mathbf{B} = 0$) the motional Stark effect vanishes. The electric field leads to a line shift as described in the previous text. Furthermore, the intensity of metastable atoms is reduced due to

the mixing with P states and decreases according to

$$N_{2S_{1/2}}(t) = N_{2S_{1/2}}(t=0) \cdot \exp(-t/\tau'_{2S_{1/2}}) \quad ,$$

where $N_{2S_{1/2}}(t)$ is the number of atoms in the $2S_{1/2}$ state at time t and $\tau'_{2S_{1/2}}$ is the reduced lifetime of the $2S_{1/2}$ state due to mixing with P states (sec. 2.4). A certain estimate of the frequency uncertainty, like in the case of the Stark effect due to an external electric field, cannot be done without a full calculation of the Stark effect as described previously.

4.1.6 Resume

There are many influences on the transition frequencies which lead to an uncertainty of the resonance centroid of a certain transition. At the present status of the experiment the magnetic field inhomogeneity is the most influencing factor, so the uncertainty of a transition frequency is mainly affected by this error.

4.2 Measurement of the Classical Lamb shift

As already described in sec. 3.2, a shielding can be assembled at the experiment which was designed during this thesis. It consists of a shielding against the magnetic field of the spinfilters and another shielding for the spectroscopy chamber itself (fig. 3.5). Due to the chamber design, the shielding can only be applied during measurements where the magnetic field coils are not needed (subsec. 3.2.8), because the magnetic field is distorted by the μ -metal material of the shielding. For the measurement of the classical Lamb shift the transitions $\alpha_1 \rightarrow e_2$, $\alpha_1 \rightarrow f_4$, $\alpha_2 \rightarrow e_1$ and $\alpha_2 \rightarrow f_3$ were chosen. However, as described below, during the experiment some problems occurred connected to the definition of the quantization axis. Because the spectroscopy chamber consists of stainless steel, it has a certain remanence and the undefined magnetic field inside the chamber affects the quantization axis. Furthermore, the two parts of the shielding (shielding against the magnetic field of the spinfilters and for the spectroscopy chamber) also affect the magnetic field inside the chamber in different ways as described below. Nevertheless, the measurement itself is working and the problems which occurred in this first test were considered for a new chamber design (chap. 5). First the measurements are presented and the results are summarized in subsec. 4.2.3.

4.2.1 Measurements without Shielding

In fig. 4.3 the electric dipole transitions (σ transitions) from the α_1 and α_2 state into the $2P_{1/2}$ state are shown. Comparing the experimental resonance shapes (black lines) with the peak shape simulation of subsec. 3.3.1, it can be noticed that the shape is sufficiently described by the simulation. The model function for the fit in fig. 4.3 is

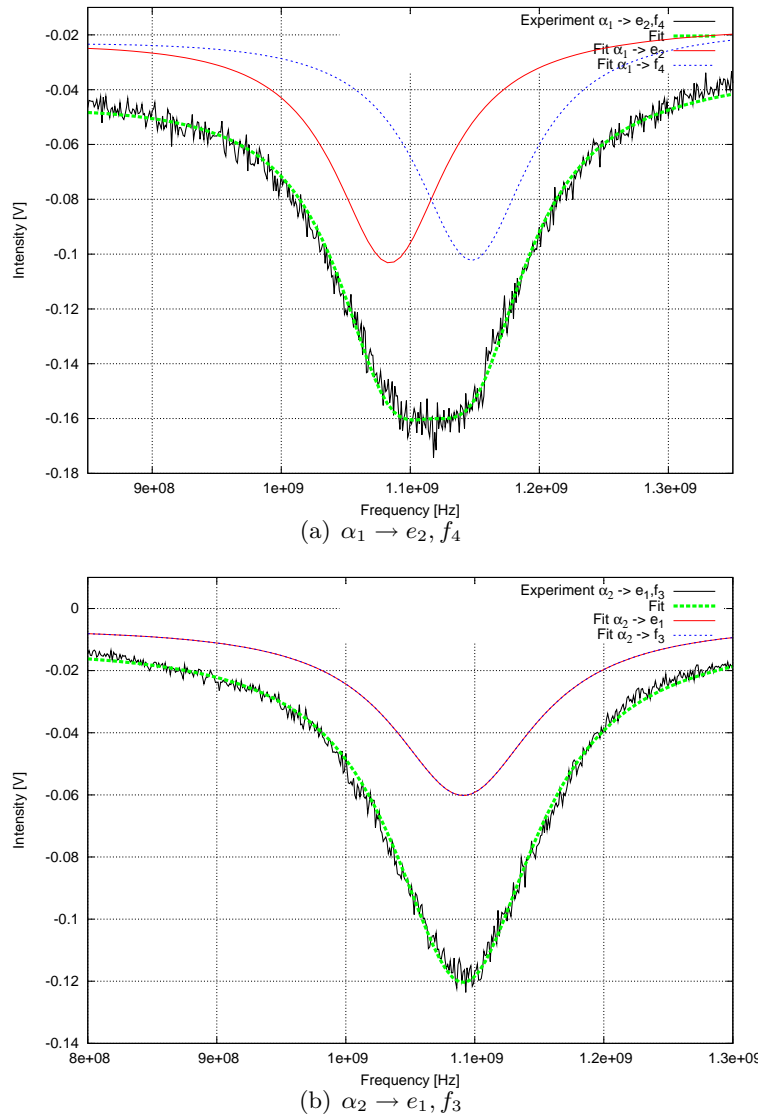


Figure 4.3: Electric dipole transitions in the unshielded experiment. The external magnetic field is switched off. Note the remarkable plateau in (a) and the narrower shape of (b). The spectra are upside down, because the output of the photomultiplier is a negative voltage. In (b) the two fits are indistinguishable.

$$I(f) = \left\{ A1 \cdot \left[\frac{\left(\frac{\Gamma}{2}\right)^2}{(f - f_{01})^2 + \left(\frac{\Gamma}{2}\right)^2} \right] + A2 \cdot \left[\frac{\left(\frac{\Gamma}{2}\right)^2}{(f - f_{02})^2 + \left(\frac{\Gamma}{2}\right)^2} \right] \right\} + \frac{2B1}{\sqrt{B2 \cdot f}} \quad (4.5)$$

It consists of the sum of two Lorentz distributions which belong to single transitions as shown in the figure and as mentioned in subsec. 3.3.1. The first spinfilter transmitted atoms in the states α_1 and α_2 , respectively, that reached the spectroscopy chamber. Without any shielding and without using an external magnetic field, the spectra shown in fig. 4.3 were obtained. Each spectrum was measured by controlling the power behind the TEM waveguide as described above. A power of 0.9 W for each transition was chosen for a first test to gain a sufficient intensity in the spectra. Furthermore, every data point was averaged three times. The whole spectrum was acquired within 10 min. A rough estimate about the collected photons in the photomultiplier can also be given. As can be seen in the graphs, the amplitude varies from about 0.12 V to 0.16 V. During the experiment, the beam and all other devices including the photomultiplier had to be continuously tuned. E.g. an amplitude of 0.16 V means, that the photomultiplier² collected about 10000 photons/s. In 10 min this are 6000000 photons (peak intensity). Therefore, from a statistical point of view it is possible within 10 min to reduce the statistical error of the resonance frequency to only 41 kHz. Nevertheless, according to subsec. 3.2.8 a total residual magnetic field could be measured in the spectroscopy chamber even if the magnetic field coils are not used. The field varies at $I = 0$ A from 0 G to -0.8 G (in the interaction region from -0.3 G to -0.8 G) along the z axis. In the case of the $\alpha_1 \rightarrow e_2, f_4$ transition, therefore, a larger transition frequency is expected with an uncertainty of about 0.5 MHz. A more pessimistic estimate yields an uncertainty of about 0.9 MHz according to the maximal observed inhomogeneity of approximately ± 0.5 G (subsec. 3.2.8) and the limit of precision of the Hall probe which was used to measure the magnetic field as already described. Therefore, at the present status of the experiment magnetic field inhomogeneities cause the largest uncertainty. In contrast to that the longitudinal Doppler effect is not expected to exceed 43 kHz for the $\alpha_1 \rightarrow e_2$ transition. Similar values of the longitudinal Doppler effect can be determined for other electric dipole transitions. Presently the Doppler effect and all other uncertainties (which are smaller) are overlapped by the magnetic field inhomogeneities inside the spectroscopy chamber. However, in the further development of this experiment to the point of a precision experiment, the Doppler effect can be observed and has to be included into the uncertainty of the frequency, although it can be canceled to first order as described in the previous section. From the peak shape simulation it can be concluded, that a dominating total residual magnetic field

²The photomultiplier was operated at -3 kV. At this dynode voltage it has an amplification of 10^7 while the quantum efficiency is 8 %.

in the spectroscopy chamber exists which is mostly perpendicular to the electric rf-field vector. Otherwise, no σ transitions could be observed as shown in fig. 4.3. The total residual magnetic field has several components. For example, a residual longitudinal magnetic field of the first spinfilter could be measured in the chamber which is in the order of 0.5 G. Furthermore, the earth magnetic field (0.6 G at the terrestrial poles) in our experiment has a longitudinal component of approximately 0.3 G and a vertical component of 0.5 G. Residual magnetic fields in the stainless steel of the spectroscopy chamber with arbitrary direction are also components of a total residual magnetic field in the spectroscopy chamber. Peak shape simulations including all transitions with different weighting allow, in principle, to determine the strength and direction of each component of the total residual magnetic field. However, the lack of knowledge of several parameters (e.g. the residual magnetic field of the spectroscopy chamber exclusively and its direction) makes this impossible.

Another possibility to measure the magnetic field components are magnetic dipole transitions in the $2S_{1/2}$ state. Similar to the peak shape simulations in the preceding chapter, also the strength of magnetic dipole transitions are influenced by an external magnetic field. Due to the metastability of the $2S_{1/2}$ state, the peak shape of such a transition is sharp. All magnetic dipole transitions in the $2S_{1/2}$ state, therefore, can be separated. Comparing the height and the frequency of the transitions, the magnetic field components and their strength can be determined.

4.2.2 Measurements with Shielding

Two different kinds of measurements with a shielded experiment were performed. The first measurement was done only with the shielding against the magnetic field of the spinfilters (fig. 3.5) but without the shielding of the spectroscopy chamber. The result is shown in fig. 4.4. Although in the unshielded experiment σ transitions could be observed, with the shielding against the spinfilter stray fields the magnetic field distribution inside the spectroscopy chamber obviously changed. A fit to the data yielded the best result for π transitions as shown in the plots. Compared to fig. 4.3, now only one transition originates from the α_1 state according to the selection rules of quantum mechanics (fig. 2.16(a)). Therefore, the resonance shape of this transition is narrower than the resonance shape of the graph shown in fig. 4.4(b). Two possible π transitions originating from the α_2 state can be observed which are separated from each other by the $2P_{1/2}$ hfs like this is the case for σ transitions starting from the α_1 state. Therefore, the resonance shape is broadened. Because the μ -metal shielding against the magnetic field of the spinfilters is a simple planar plate, longitudinal magnetic field components of the first spinfilter seem to reach the spectroscopy chamber through the beamline while vertical components are attracted by the μ -metal plate. Compared to this, in

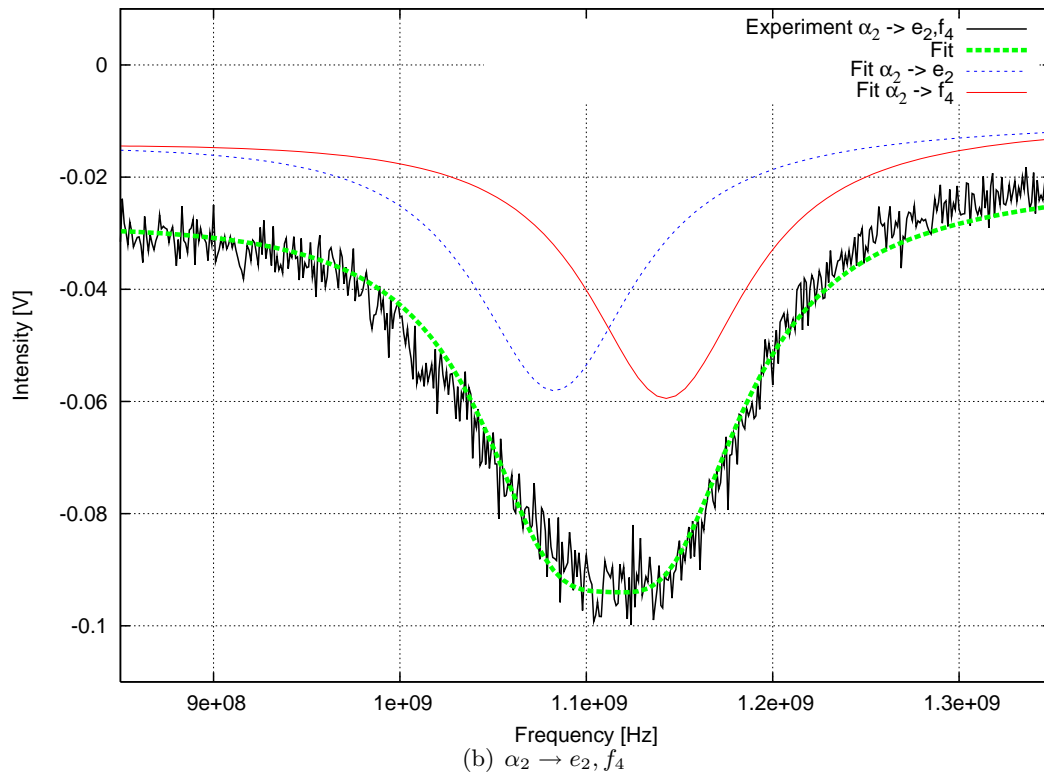
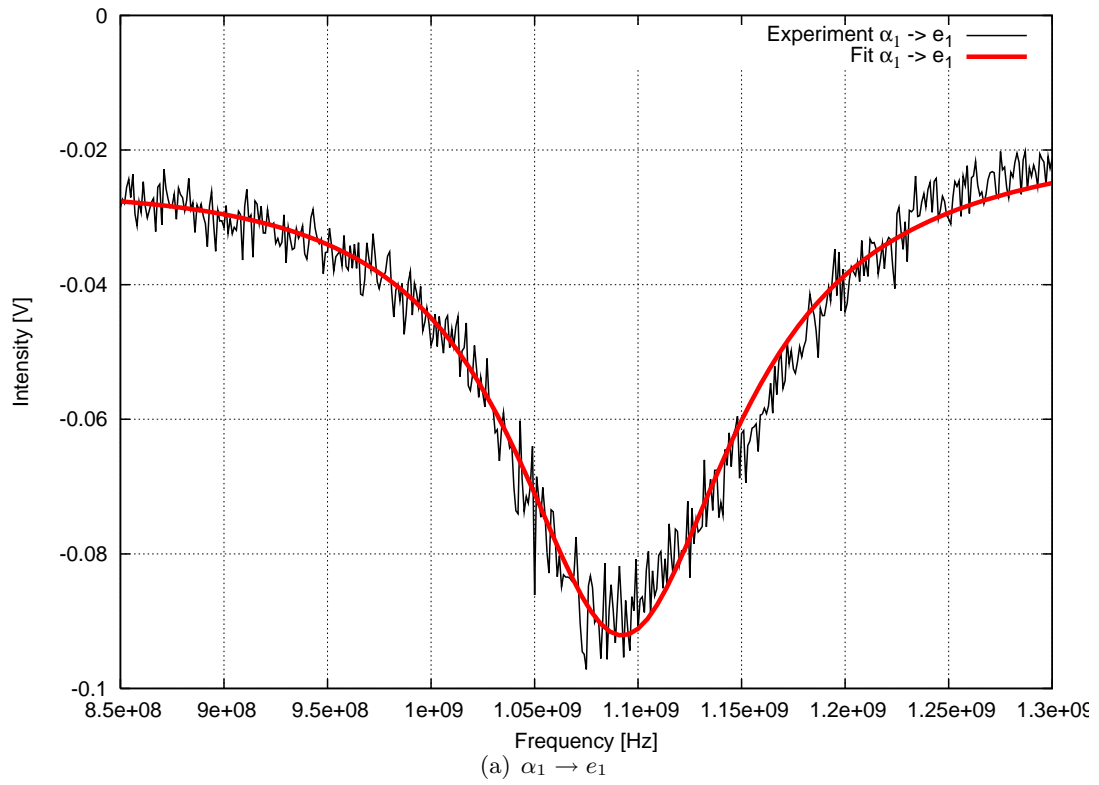


Figure 4.4: Electric dipole transitions with shielded spinfilters. The external magnetic field is switched off.

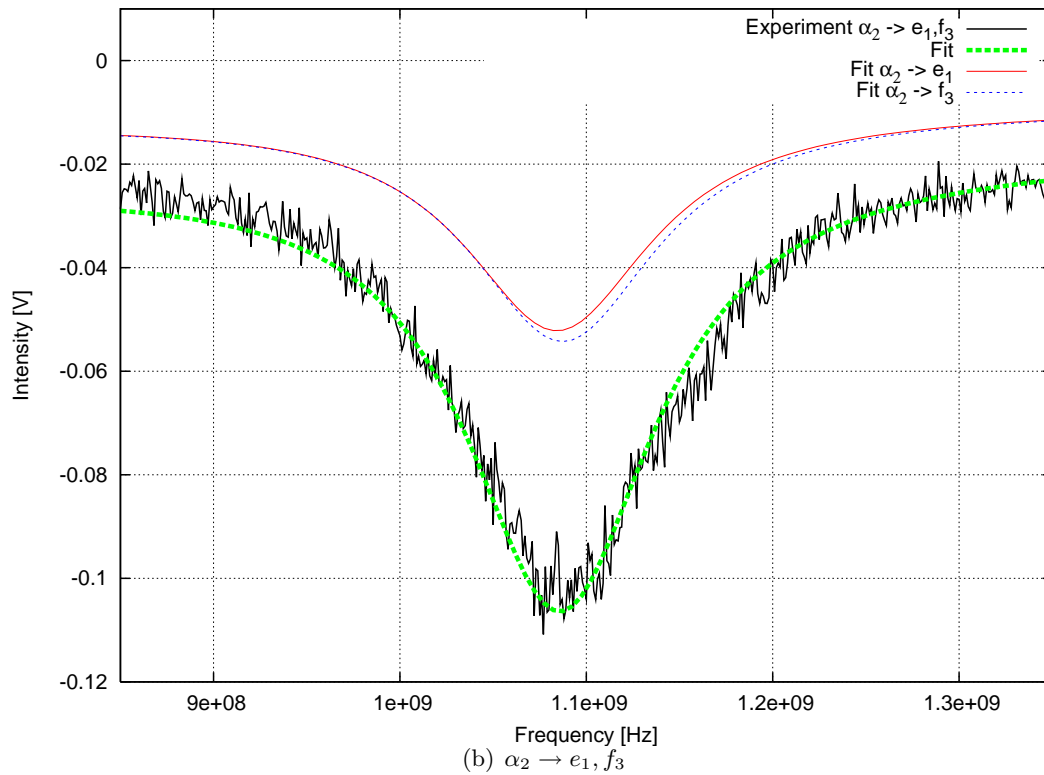
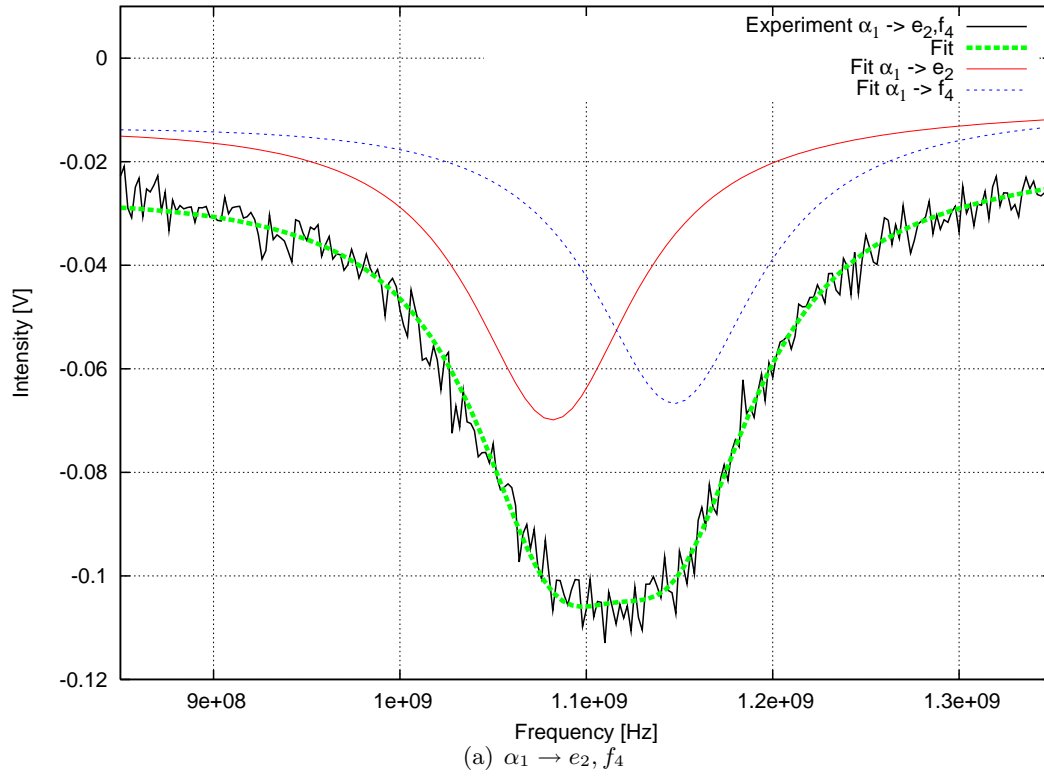


Figure 4.5: Electric dipole transitions in the completely shielded experiment. The external magnetic field is switched off.

a completely shielded experiment, again σ transitions can be observed (fig. 4.5). The fit to the data yielded the best result for σ transitions. It is expected that the main influence now originates from the chamber itself producing again a dominant vertical magnetic field. Especially from fig. 4.5(b) a rough estimate of the magnetic field produced by the chamber can be given. As can be seen, the best fit yields two distinguishable Lorentz distributions to describe the total resonance corresponding to the two possible σ transitions starting from the α_2 state. The shifting and the height of the distributions is proportional to a magnetic field according to the Breit-Rabi formula and eq. 3.6. A residual magnetic field in the spectroscopy chamber, therefore, can be calculated and as a result 2 G is obtained. This field has to be mostly vertical, because σ transitions were observed! Compared to fig. 4.3(b), such a difference of these two distributions could not be obtained as result of the fit. The measurement shown in fig. 4.3 was performed without shielding and it is, nevertheless, expected that a residual magnetic field of the same order as determined above influenced the measurement. Looking back to fig. 4.3(a), the two distributions have different heights, although the smaller blue colored Lorentz distribution has to be bigger than the red one according to the peak shape simulations. However, also in this figure, the best fit was obtained with two different peak heights, which allows to say that a magnetic field influenced the measurement. The same is valid for the result shown in fig. 4.4(b).

The deviation from an ideal Lorentzian distribution in fig. 4.4(a) and 4.5(b), especially in the frequency region about 1150 MHz - 1200 MHz, is because the magnetic field in the spectroscopy chamber is not exclusively pointing in one direction. Therefore, a mixture of σ and π transitions is observed although just one kind of these transitions had a dominating intensity.

4.2.3 Results

The results of the fits of the preceding subsections are summarized in table 4.1. They are the basis for the determination of the classical Lamb shift and the $2P_{1/2}$ hfs (subsec. 4.2.4 and 4.2.5). At $B \approx 0$ G (i.e. in a defined magnetic field which is close to zero), the transitions $\alpha_1 \rightarrow e_2$, $\alpha_2 \rightarrow e_1$, $\alpha_2 \rightarrow f_3$, $\alpha_1 \rightarrow e_1$ and $\alpha_2 \rightarrow e_2$ are separated by approximately the same frequency. The same is valid for the transitions $\alpha_1 \rightarrow f_4$ and $\alpha_2 \rightarrow f_4$. As can be seen, this is not the case with the measured values. The reason for this deviation is very simple. To select the states α_1 or α_2 , different magnetic fields in the spinfilter are needed which influence the spectroscopy chamber in different ways. To select the state α_1 a magnetic field of approximately 538 G and for the state α_2 a larger field of approximately 605 G are needed. Comparing the values in table 4.1, a tendency can be noticed which is connected with the magnetic field of the spinfilter. The values which were obtained from fig. 4.3 (unshielded experiment) are

Table 4.1: Results for the resonance frequencies obtained from the fits of subsec. 4.2.1 and 4.2.2. The uncertainty is the statistical error from the fit. As reference, the theoretical expectation is added ([Mos06, Mos07a]). Its error is dominated by the recent experimental uncertainty of the classical Lamb shift.

(a)

	σ transitions			
	$\alpha_1 \rightarrow e_2$ [kHz]	$\alpha_1 \rightarrow f_4$ [kHz]	$\alpha_2 \rightarrow e_1$ [kHz]	$\alpha_2 \rightarrow f_3$ [kHz]
Fig. 4.3	1084 180(727)	1147 810(725)	1091 080(824)	1091 080(824)
Fig. 4.4	—	—	—	—
Fig. 4.5	1082 010(1249)	1147 390(1287)	1084 430(873)	1087 430(831)
Theory	1087 429(3)	1146 650(3)	1087 429(3)	1087 429(3)

(b)

	π transitions		
	$\alpha_1 \rightarrow e_1$ [kHz]	$\alpha_2 \rightarrow e_2$ [kHz]	$\alpha_2 \rightarrow f_4$ [kHz]
Fig. 4.3	—	—	—
Fig. 4.4	1092 540(462)	1083 060(1454)	1143 040(1408)
Fig. 4.5	—	—	—
Theory	1087 429(3)	1087 429(3)	1146 650(3)

larger than the values obtained from fig. 4.5 (completely shielded experiment) which is due to the shielding of the experiment. But in addition to this it can be noticed that σ transitions originating from the α_2 state are always larger than transitions originating from the α_1 state although some of them should be equal (e.g. $\alpha_1 \rightarrow e_2$ compared with $\alpha_2 \rightarrow f_3$ in table 4.1(a)). Values of the resonance frequency in experiments where only the spinfilters were shielded (especially the first spinfilter) show another result. Low magnetic fields seem to have a stronger influence on the transitions than stronger fields. Additionally, longitudinal fields are not shielded as good as vertical fields (see above). In table 4.1 also values were obtained from the fits which are smaller than the theoretical expectation. This is due to the determination with the help of a fit itself and this procedure has to be improved. E.g. with a more intense metastable atomic beam, larger spectrum intensities can be reached and the fit will be better.

4.2.4 First Determination of the $2P_{1/2}$ HFS

The $2P_{1/2}$ hfs can be determined by the frequency difference of the $\alpha_1 \rightarrow f_4$ and the $\alpha_1 \rightarrow e_2$ transition or by the frequency difference of the $\alpha_2 \rightarrow f_4$ and $\alpha_2 \rightarrow e_2$ transition at $B \approx 0$ G. In table 4.2 the very first results of measurements with the modified LSP are presented, determined from the values of table 4.1. Compared with the theoretical expectation, except for the value determined from fig. 4.4, the values are too large due to the already mentioned problems caused by residual magnetic fields in the spectroscopy chamber and the influence of the spinfilter.

Another possibility to determine the $2P_{1/2}$ hfs, as already mentioned for the $2S_{1/2}$ hfs in subsec. 3.3.2, is the combination of several transitions. With the measurement of the $\alpha_1 \rightarrow f_4$, $\alpha_2 \rightarrow f_3$, $\alpha_1 \rightarrow e_1$ and the $\alpha_2 \rightarrow e_2$ transitions in an arbitrary magnetic field, the $2P_{1/2}$ hfs can be determined according to the following equation

$$f_{hfs}(2P_{1/2}) = [(\alpha_1 \rightarrow f_4) - (\alpha_2 \rightarrow f_3)] - [(\alpha_1 \rightarrow e_1) - (\alpha_2 \rightarrow e_2)] \quad , \quad (4.6)$$

where $f_{hfs}(2P_{1/2})$ is the $2P_{1/2}$ hfs. Presently this method is not possible due to the already mentioned problems with residual magnetic. Additionally, longitudinal and transversal magnetic fields with the same strength are needed.

Table 4.2: Determination of the $2P_{1/2}$ hfs. For the calculation of the theoretical value see chap. 2.

	Fig. 4.3 [kHz]	Fig. 4.4 [kHz]	Fig. 4.5 [kHz]
	63 630(1027)	59 980(2025)	65 380(1794)
Theory	59 221.2	59 221.2	59 221.2

4.2.5 Determination of the Classical Lamb shift

For the determination of the classical Lamb shift the value of the $2S_{1/2}$ and the $2P_{1/2}$ hfs is needed. Until the production of the magnetic rf coil is not finalized, the $2S_{1/2}$ hfs cannot be measured with the modified LSP. When finalized, the modified LSP is an experiment which allows to measure all parameters to determine fundamental quantities like, besides others, the $2S_{1/2}$ hfs. With the knowledge of the $2S_{1/2}$ and the $2P_{1/2}$ hfs, the spacing between the $2S_{1/2}$ and the $2P_{1/2}$ fine structure terms can be calculated to obtain the classical Lamb shift (fig. 2.10). Until the first measurement of the $2S_{1/2}$ hfs with the modified LSP, the value of [Kol04b] is taken for a first calculation.

Furthermore, the value for the $2P_{1/2}$ hfs, determined from fig. 4.4, was used. The classical Lamb shift can be determined by using, in principle, every transition from the $2S_{1/2}$ into the $2P_{1/2}$ state in very small magnetic fields close to zero. Very first results are presented in table 4.3. As can be seen, results have already been obtained which show that the experimental principle is working. Nevertheless, the precision is not sufficient for a precision experiment and has to be further improved.

In a naive approach it can be estimated that the systematic errors due to the misaligned magnetic fields in the spectroscopy chamber will cancel each other. The averaged value of all preliminary values for the classical Lamb shift is 1057340(1110) kHz! It fits perfectly to the theory (table 2.2).

Table 4.3: Determination of the classical Lamb shift. As reference the measurement of [Sch99] was chosen. The statistical error of the fit was used for the determination of the uncertainty of the classical Lamb shift.

(a)

	σ transitions			
	$\alpha_1 \rightarrow e_2$ [kHz]	$\alpha_1 \rightarrow f_4$ [kHz]	$\alpha_2 \rightarrow e_1$ [kHz]	$\alpha_2 \rightarrow f_3$ [kHz]
Fig. 4.3	1054 786(886)	1058 436(1683)	1061 686(968)	1061 686(968)
Fig. 4.4	—	—	—	—
Fig. 4.5	1052 616(1348)	1058 016(1991)	1055 036(1010)	1058 036(974)
Reference	1057 845(3)	1057 845(3)	1057 845(3)	1057 845(3)

(b)

	π transitions		
	$\alpha_1 \rightarrow e_1$ [kHz]	$\alpha_2 \rightarrow e_2$ [kHz]	$\alpha_2 \rightarrow f_4$ [kHz]
Fig. 4.3	—	—	—
Fig. 4.4	1063 146(686)	1053 666(1540)	1053 666(2072)
Fig. 4.5	—	—	—
Reference	1057 845(3)	1057 845(3)	1057 845(3)

4.3 Electric Dipole Transitions in an External Magnetic Field

Electric dipole transitions were observed in an external magnetic field to show the working principle of the experiment for this kind of measurement. Metastable atoms in the state α_2 are transmitted by the first spinfilter. The atoms enter the spectroscopy chamber (unshielded) in which a magnetic field is produced by the field coils. Fig. 4.6 shows the result of the measurement and the analysis of the data. In a magnetic field of 26.77 G (fig. 4.6(a)) and 54.29 G (fig. 4.6(b)) the presented spectra were acquired and analyzed according to subsec. 3.3.1. The best fit was obtained, according to the peak shape simulation, in considering a decreasing transition probability for transitions into the e_1 state with increasing magnetic field as shown in the plots. The figs. 4.7 and 4.8 show the comparison with the recent theory and for a first test of the experiment a very good result was obtained. However, the uncertainty due to the magnetic field inhomogeneity prevents a more precise measurement. This has to be improved. The uncertainty of the transition frequency is of the order of 500 kHz and has to be lowered by two orders of magnitude to perform a precision experiment.

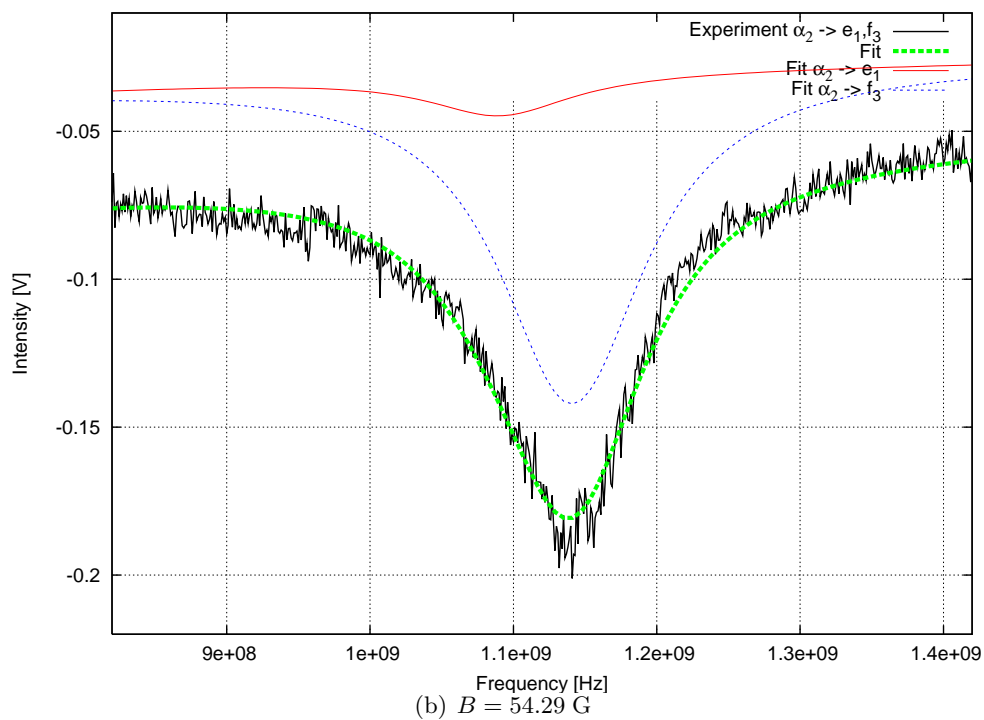
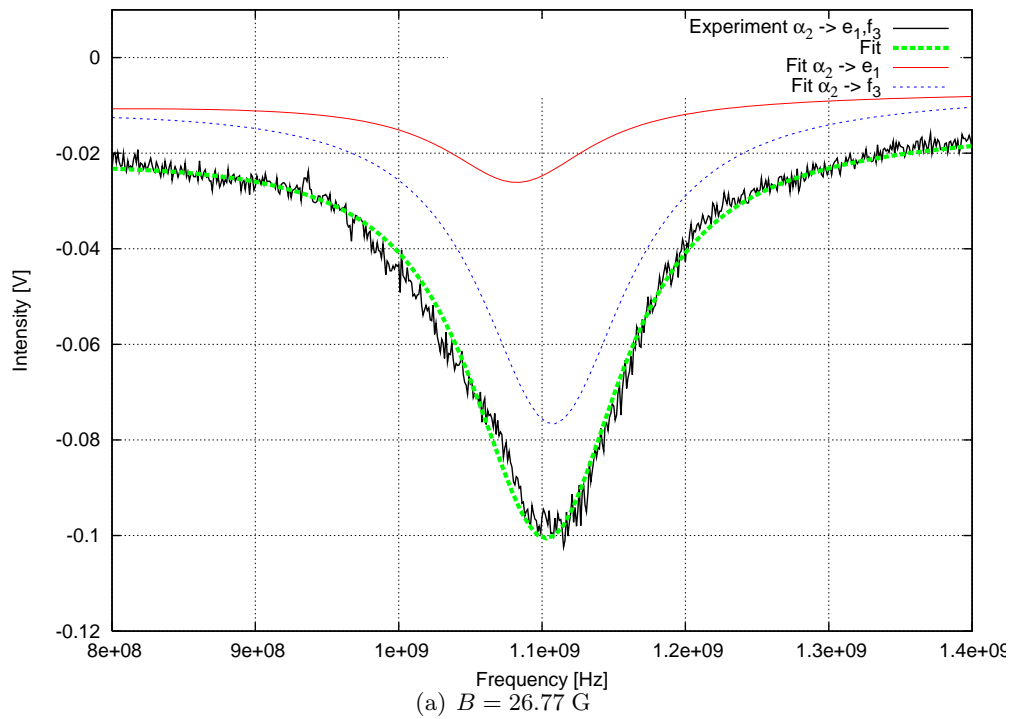


Figure 4.6: Electric dipole transitions in a magnetic field originating from the state α_2 .

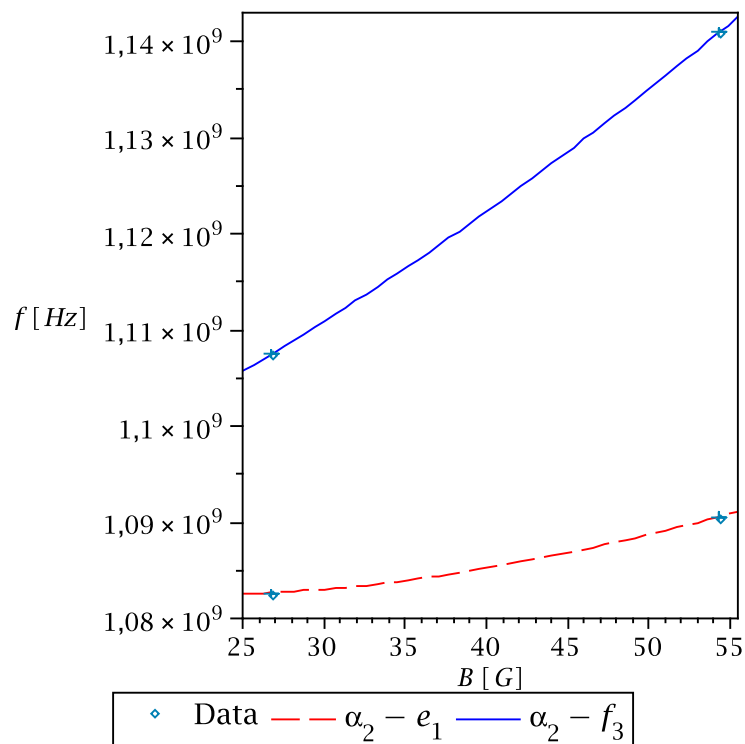
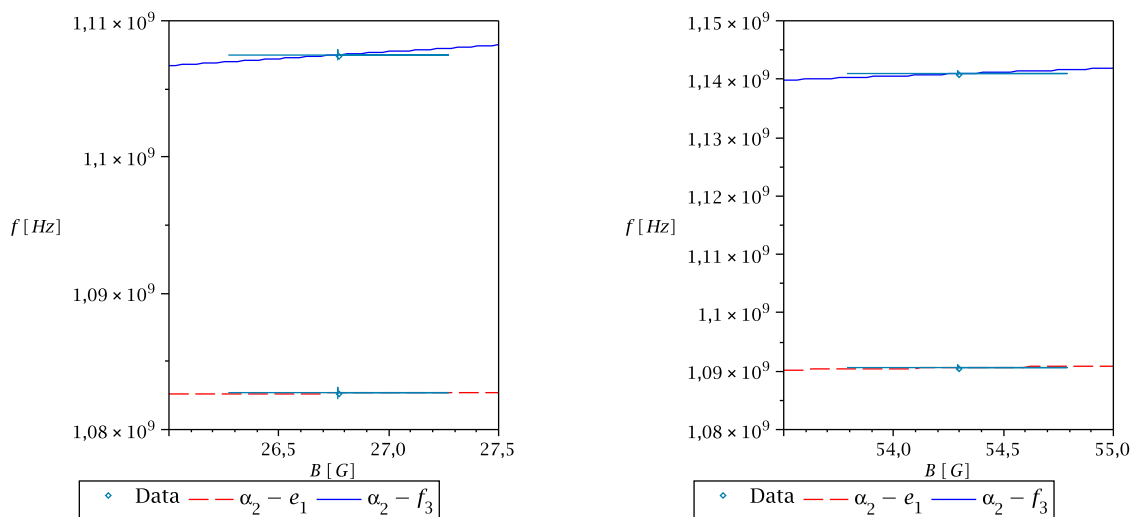


Figure 4.7: Portion of fig. 2.16(b). Comparison between the experimental data determined from fig. 4.6 and theory.



(a) Comparison for experimental data taken at $B = 26.77$ G.

(b) Comparison for experimental data taken at $B = 54.29$ G.

Figure 4.8: Magnification of fig. 4.7 for the specific value of the magnetic field.

CHAPTER 5

CONCLUSION & OUTLOOK

With the experiment assembled and commissioned in this thesis, first highly promising results were obtained as presented in the preceding text. A further development and improvement of the experiment, not only from the experimental point of view, but also because of the requests from theorists, is absolutely necessary as already described in previous chapters. The present status of the experiment and of the modified LSP can be seen as proof-of-principle of the measurement and the functionality of the hardware.

Unlike the experiments of Lamb and Retherford, in this thesis electric dipole transitions were measured as a function of frequency while the power was controlled up to the limit of the present hardware. The acquired spectra show a big photon count rate of about 10000 photons/s which is a very promising basis to obtain a small statistical uncertainty in future experiments. In addition, a method was found which allows to determine the $2S_{1/2}$ and the $2P_{1/2}$ hfs in a constant but arbitrary magnetic field. The combination of several observable transitions without the need to extrapolate to vanishing magnetic field provides a precise method to determine these hyperfine structures.

Furthermore, first results of the $2P_{1/2}$ hfs, of the classical Lamb shift and of electric dipole transitions in an external magnetic field were obtained. The results are consistent with the theoretical prediction, although still afflicted with a large uncertainty.

Some hardware parts like e.g. the powermeter or the hall probe limit the precision of the present experiment. Furthermore, the spectroscopy chamber is insufficient to reach a higher degree of precision. Therefore, at the end of this thesis, a rough plan on how to continue in the further development of this experiment is presented.

1. The spectroscopy chamber has to be completely exchanged against a new block-shaped chamber made from aluminum which has a vanishing remanence. On the outer and on the inner part of the chamber μ -metal shieldings can be glued onto the surface. Although the chamber itself is already a Faraday cage, an additional cage should be inserted to be able to control the influence of external electric

fields in the spectroscopy region.

2. For the TEM waveguide and the magnetic rf coil an easily accessible support should be designed in order to simplify the insertion of these devices.
3. Magnetic field coils to produce a well defined external magnetic field should be inserted into the vacuum, i.e. in the chamber itself. A preferable coil system in the chamber would be a 3D coil assembly consisting of six Helmholtz coils on the three axes. Such an assembly would allow to compensate actively possible inhomogeneities. For further measurements, first of all low field measurements of the Breit-Rabi diagrams of up to 10 G should be finished until continuing with measurements in higher fields. Coils producing magnetic fields in this range can be cooled passively in the vacuum, so no water cooling has to be inserted into the spectroscopy chamber. For large magnetic fields up to 1.5 T the dipole magnet shown in fig. 3.23(a) may be useful. Measurements of the classical Lamb shift and the $2P_{1/2}$ hfs need a well defined but also very small external magnetic field which defines the quantization axis. A new coil setup should provide these measurements, too.

In contrast to the 3D coil system, another approach would be the design of a rotatable coil pair to produce longitudinal and transversal magnetic fields.

4. A new Hall probe is needed with a precision of the order of mG or better which can be mounted directly into the spectroscopy chamber. In this case no calibration of the field coils is necessary anymore. Of course, the external magnetic field homogeneity also has to be of this order. In this case, the uncertainty of the transition frequencies reach a value of approximately 4 kHz for transitions into the $2P_{1/2}$ state and a value of approximately 2 kHz for transitions within the $2S_{1/2}$ state. A homogeneity level of the magnetic field of about 10 μ G would allow to perform a high-precision experiment. In this case the transitions within the $2S_{1/2}$ state would have an uncertainty of only 50 Hz. At this level of the magnetic field inhomogeneity, transitions into the $2P_{1/2}$ state can be determined with a precision of about 3 kHz. Because of physical reasons due to the instability of the $2P_{1/2}$ state it is not clear if a more precise determination is possible. This question is subject of recent research in atomic physics ([Kar05]).
5. Furthermore, a new powermeter is also necessary to control the power more precisely and faster. As already described in the preceding text, it was possible to control the power on a 3 % level. However, for a precision experiment fluctuations of the same order in the transition spectra are too large. Recent powermeters can control the power on a 0.002 % level and such a device is highly recommended for

a future experiment. Another reason of peak distortion which was not checked in the framework of this thesis is the possibility of an unstable metastable atomic beam. To be aware of beam intensity fluctuations, the ion current on the Faraday cup should be measured during the whole experiment.

6. The ionizer which was used in this thesis in the same setup like at the ANKE experiment at COSY should be dismantled and vertically remounted on the bench of the modified LSP in order to increase the intensity of metastable atoms. A vertical assembly of the ionizer does not need the deflector chamber where a significant amount of intensity gets lost. Another method would be to use the atomic beam source of our institute to produce a high flux of ground state hydrogen (deuterium) atoms in one Zeeman component of the hfs. In this thesis, H_2 gas was used to produce protons and unavoidable H_2^+ ions up to the space charge limit. But in this case a huge amount (90 %) of the ion current are H_2^+ ions which cannot be used to produce metastable atoms by the charge exchange reaction in the cesium cell. Using an atomic beam source, this relation is reversed and a huge amount of protons can be produced in the ionizer volume [Eng05]. Due to the high flux production of ground state atoms in one certain Zeeman state by the atomic beam source, also a high flux of metastable atoms in one Zeeman component can be produced. The intensity behind the first spinfilter does not decrease as much as with the conventional method used in this thesis where single Zeeman components were selected by the first spinfilter. An increase in the flux by a factor of 2 is expected according to this effect. In total the number of photons which can be measured with the photomultiplier can be increased by a factor of 20 also due to the higher flux of the atomic beam source compared to the present method.
7. In combination with a new spectroscopy chamber, longitudinal magnetic field coils should be installed between the first spinfilter and the new spectroscopy chamber to induce Sona transitions. For this kind of non-adiabatic transitions field coils are needed which produce a static magnetic field with opposite direction with respect to the first spinfilter. Atoms in the state α_1 leaving the magnetic field of the first spinfilter and entering the opposed magnetic field are transformed into the β_3 state. With atoms in the β_3 state a new Zeeman component of the metastable $2S_{1/2}$ state can be used to induce other transitions within the $2S_{1/2}$ state or into the $2P_{1/2}$ state.

The next measurement with the modified LSP should be the determination of the $2S_{1/2}$ hfs like described in this thesis (subsec. 3.3.2). As already mentioned, with the modified LSP a completely new method to access this fundamental quantity is

provided. Compared to the measurements in this thesis, the measurement of magnetic dipole transitions is easier and, therefore, these measurements were not performed at first, but electric dipole transitions. Furthermore, a more precise determination of the $2P_{1/2}$ hfs is of great interest. This is also valid for the experimental determination of the Breit-Rabi diagrams in the first excited state. The classical Lamb shift is of course of great importance, too, because the modified LSP is a completely independent experiment compared to recent precision experiments.

Although first experiments were performed with a metastable hydrogen beam, the same experiments with a metastable deuterium beam can also be performed. Experiments of this kind with deuterium are highly interesting and fundamental.

In the far future, anti-hydrogen spectroscopy experiments could provide the perhaps most fundamental symmetry test in physics. The preparation of such an experiment presently focuses on ground-state atoms although in the anti-hydrogen production lots of metastable anti-atoms are produced. Therefore, the experiment presented in this thesis could provide an alternative for anti-hydrogen spectroscopy to use these few metastable anti-atoms. The measurement of e.g. the $2S_{1/2}$ hfs in anti-hydrogen like described in this thesis for the hydrogen atom would also provide a symmetry test because the influences of the anti-proton are directly visible in the transition spectrum.

Within the framework of a PhD thesis (approximately three years) a precision measurement with the modified LSP is possible. A precision measurement of the $2S_{1/2}$ hfs for example can be performed within only one year with the present setup and the magnetic rf coil. The total amount of new devices like suggested above will not exceed a price of 20000 euro estimated over three years.

APPENDIX A

BREIT-RABI FORMULA COEFFICIENTS

Table A.1: Numerical values of the Breit-Rabi formula coefficients of hydrogen and deuterium for the $2S_{1/2}$ and $2P_{1/2}$ state calculated by [Mos07a] for this thesis.

Atom	$H_1^1(2S_{1/2})$	$H_1^1(2P_{1/2})$	$H_1^2(2S_{1/2})$	$H_1^2(2P_{1/2})$
g_j	2.002310441392(22)	0.6651585(46)	2.002310437776(22)	0.6655214(46)
$\langle r^2 \rangle^{1/2}$	0.879(9) fm	0.879(9) fm	2.140(9) fm	2.140(9) fm
I	$\frac{1}{2}$	$\frac{1}{2}$	1	1
a_1	—	—	-0.000466975445(5)	-0.000466975445(5)
ϵ_1	—	—	-0.00000443765	-0.145960(11)
$a_1(1 + \epsilon_1)$	—	—	-0.000466973372(5)	-0.000398816(5)
$\epsilon_2 (= \eta_2)$	$2.62894 \cdot 10^5$	$-2.50741(2) \cdot 10^9$	$2.62894 \cdot 10^5$	$-2.50739(2) \cdot 10^9$
c_1	—	—	2.00277741322(2)	0.665988(5)
δ_1	—	—	-0.00000001035	-0.00009825(3)
$c_1(1 + \delta_1)$	—	—	2.00277741115(2)	0.665923(5)
c_2	4.02143867224(16)	0.446492(6)	4.01111736691(9)	0.443541(6)
δ_2	-0.00000001346	-0.001348954(10)	-0.000000002069	-0.000210320(14)
δ_3	—	—	0.0	0.00000614(3)
$c_2(1 + \delta_2)$	4.02143861810(16)	0.445890(6)	4.01111735861(9)	0.443447(6)
$c_2\delta_3$	—	—	0.0	0.000002725(14)
d_1	0.99963418853(2)	0.331058(2)	1.000688243443(12)	0.332294(2)
η_1	0.000000006752	0.000680675(5)	0.000000002071	0.000209224(6)
$d_1(1 + \eta_1)$	0.99963419528(2)	0.331284(2)	1.000688245516(12)	0.332363(2)

Bibliography

- [Bei00] Beier, T., Lindgren, I., Persson, H., Salomonson, S., Sunnergren, P., Häffner, H., Hermanspahn, N. g_j factor of an electron bound in a hydrogenlike ion. *Physical Review A*, 62:032510, 2000.
- [Ber82] Berestetskii, V. B., Lifshitz, E. M., Pitaevskii, L. P. *Quantum Electrodynamics*. Pergamon Press, second edition, 1982.
- [Bjo90] Bjorken, J. D., Drell, S. D. *Relativistische Quantenmechanik*. BI Wissenschaftsverlag, 1990.
- [Boh50] Bohr, A., Weisskopf, V. F. The Influence of Nuclear Structure on the Hyperfine Structure of Heavy Elements. *Physical Review*, 77(1):94–98, 1950.
- [Bou96] Bourzeix, S. et al. High Resolution Spectroscopy of the Hydrogen Atom: Determination of the 1S Lamb Shift. *Physical Review Letters*, 76(3):384–387, 1996.
- [Bre28] Breit, G. The Magnetic Moment of the Electron. *Nature*, 122:649–649, 1928.
- [Bre31] Breit, G., Rabi, I. I. Measurement of Nuclear Spin. *Physical Review*, 38:2082–2083, 1931.
- [Bro66] Brodsky, S. J., Erickson, G. W. Radiative Level Shifts. III. Hyperfine Structure in Hydrogenic Atoms. *Physical Review*, 148(1):26–46, 1966.
- [Coh77a] Cohen-Tannoudij, C., Diu, B., Laloe, F. *Quantum Mechanics*, volume 1. Wiley & Sons, second revised and enlarged edition, 1977.
- [Coh77b] Cohen-Tannoudij, C., Diu, B., Laloe, F. *Quantum Mechanics*, volume 2. Wiley & Sons, second revised and enlarged edition, 1977.
- [Emm00] Emmerich, R. Aufbau und Test eines Ionisierers für das Lambshiftpolarimeter, 2000. Diplomarbeit, Universität zu Köln.

- [Eng02] Engels, R. Entwicklung eines universellen Lambshift-Polarimeters für polarisierte Atomstrahl-Targets wie an ANKE/COSY, 2002. Dissertation, Universität zu Köln.
- [Eng03] Engels, R. et al. Precision Lamb-shift polarimeter for polarized atomic and ion beams. *Review of Scientific Instruments*, 74(11):4607–4615, 2003.
- [Eng05] Engels, R. et al. Background reduction by a getter pump around the ionization volume of a Lamb-shift polarimeter and possible improvements of polarized ion sources. *Review of Scientific Instruments*, 76:053305, 2005.
- [Fey49a] Feynman, R. P. Space-Time Approach to Quantum Electrodynamics. *Physical Review*, 76(6):769–789, 1949.
- [Fey49b] Feynman, R. P. The Theory of Positrons. *Physical Review*, 76(6):749–759, 1949.
- [Fri99] Friar, J. L., Martorell, J., Sprung, D. W. L. Hadronic vacuum polarization and the Lamb shift. *Physical Review A*, 59(5):4061–4063, 1999.
- [Gel51] Gell-Mann, M., Low, F. Bound States in Quantum Field Theory. *Physical Review*, 84(2):350–354, 1951.
- [Gla02] Glazov, D. A., Shabaev, V. M. Finite nuclear size correction to the bound-electron g factor in a hydrogenlike atom. *Physics Letters A*, 297:408–411, 2002.
- [Hag94] Hagley, E. W., Pipkin, F. M. Separated Oscillatory Field Measurement of Hydrogen $2S_{1/2} - 2P_{3/2}$ Fine Structure Interval. *Physical Review Letters*, 72(8):1172–1175, 1994.
- [Heb56] Heberle, J. W. et al. Hyperfine Structure of the Metastable Hydrogen Atom. *Physical Review*, 101(2):612–620, 1956.
- [Jen03] Jentschura, U. Theorie der Lamb-Verschiebung in wasserstoffartigen Systemen. arXiv:hep-ph/0305065v1, 2. Auflage, 2003. Diplomarbeit.
- [Jen04] Jentschura, U. Quantum Electrodynamic Bound-State Calculations and Large-Order Perturbation Theory. arXiv:hep-ph/0306153v2, 3rd edition, 2004. Habilitation Thesis, Dresden University of Technology.
- [Kar95] Karshenboim, S. G. Muonic vacuum polarization contribution to the energy levels of atomic hydrogen. *Journal of Physics B*, 28:77–79, 1995.

- [Kar97] Karshenboim, S. G. The Lamb shift of excited S-levels in hydrogen and deuterium atoms. *Zeitschrift für Physik D*, 39:109–113, 1997.
- [Kar99] Karshenboim, S. G. What do we actually know on the proton radius? *Canadian Journal of Physics*, 77:241–266, 1999.
- [Kar01] Karshenboim, S. G., Pavone, F. S., Bassani, F., Inguscio, M., Hänsch, T. W. *The Hydrogen Atom, Precision Physics of Simple Atomic Systems*. Lecture Notes in Physics. Springer, 2001.
- [Kar02a] Karshenboim, S. G., Ivanov, V. G. Hyperfine structure in hydrogen and helium ion. *Physics Letters B*, 524:259–264, 2002.
- [Kar02b] Karshenboim, S. G., Ivanov, V. G. Hyperfine structure of the ground and first excited states in light hydrogen-like atoms and high-precision tests of QED. *The European Physical Journal D*, 19(1):13–23, 2002.
- [Kar03] Karshenboim, S. G. *Precision Physics of Simple Atomic Systems*, volume 627 of *Lecture Notes in Physics*, Part IV Testing Quantum Electrodynamics, Simple Atoms, Quantum Electrodynamics and Fundamental Constants, pages 141–162. Springer Berlin/Heidelberg, 2003.
- [Kar05] Karshenboim, S. G. Precision physics of simple atoms: QED tests, nuclear structure and fundamental constants. *Physics Reports*, 422:1–63, 2005.
- [Kin90] Kinoshita, T. *Quantum Electrodynamics*. World Scientific, Singapore, 1990.
- [Kol04a] Kolachevsky, N. et al. 2S hyperfine structure of atomic deuterium. *Physical Review A*, 70:062503, 2004.
- [Kol04b] Kolachevsky, N. et al. High-Precision Optical Measurement of the 2S Hyperfine Interval in Atomic Hydrogen. *Physical Review Letters*, 92(3):033003, 2004.
- [Kus40] Kusch, P., Millman, S., Rabi, I. I. The Radiofrequency Spectra of Atoms, Hyperfine Structure and Zeeman Effect in the Ground State of Li^6 , Li^7 , K^{39} and K^{41} . *Physical Review*, 57:765–780, 1940.
- [Lam47] Lamb, W. E., Retherford, R. C. Fine Structure of the Hydrogen Atom by a Microwave Method. *Physical Review*, 72(3):241–243, 1947.
- [Lam51] Lamb, W. E., Retherford, R. C. Fine Structure of the Hydrogen Atom. Part II. *Physical Review*, 81(2):222–232, 1951.

- [Lee05] Lee, R. N., Milstein, A. I., Terekhov, I. S. Virtual light-by-light scattering and the g factor of a bound electron. *Physical Review A*, 71:052501, 2005.
- [Lun81] Lundeen, S. R., Pipkin, F. M. Measurement of the Lamb Shift in Hydrogen, $n = 2$. *Physical Review Letters*, 46(4):232–235, 1981.
- [McK68] McKibben, J. L., Lawrence, G. P., Ohlsen, G. G. Nuclear Spin Filter. *Physical Review Letters*, 20(21):1180–1182, 1968.
- [Mel00] Melnikov, K., van Ritbergen, T. Three-Loop Slope of the Dirac Form Factor and the 1S Lamb Shift in Hydrogen. *Physical Review Letters*, 84:1673–1676, 2000.
- [Mil04] Milstein, A. I. et al. Finite-nuclear-size effect on the Lamb shift of $s_{1/2}$, $p_{1/2}$ and $p_{3/2}$ atomic states. *Physical Review A*, 69:022114, 2004.
- [Mos04] Moskovkin, D. L., Oreshkina, N. S., Shabaev, V. M., Beier, T., Plunien, G., Quint, W., Soff, G. g factor of hydrogenlike ions with nonzero nuclear spin. *Physical Review A*, 70:032105, 2004.
- [Mos06] Moskovkin, D. L., Shabaev, V. M. Zeeman effect of the hyperfine-structure levels in hydrogenlike ions. *Physical Review A*, 73:052506, 2006.
- [Mos07a] Moskovkin, D. L., Glazov, D. Private communication 1, 2007.
- [Mos07b] Moskovkin, D. L., Glazov, D. Private communication 2, 2007.
- [Nef02] Nefiodov, A. V., Plunien, G., Soff, G. Nuclear-Polarization Correction to the Bound-Electron g Factor in Heavy Hydrogenlike Ions. *Physical Review Letters*, 89(8):081802, 2002.
- [Pac96] Pachucki, K. Theory of the energy levels and precise two-photon spectroscopy of atomic hydrogen and deuterium. *Journal of Physics B*, 29:177–195, 1996.
- [Pac01] Pachucki, K. Logarithmic two-loop corrections to the Lamb shift in hydrogen. *Physical Review A*, 63:042503, 2001.
- [Pac05] Pachucki, K., Czarnecki, A., Jentschura, U. D., Yerokhin, V. A. Complete two-loop correction to the bound-electron g factor. *Physical Review A*, 72:022108, 2005.
- [Pal85] Palchikov, V. G., Sokolov, Y. L., Yakovlev, V. P. Measurement of the Lamb Shift in H, $n = 2$. *Metrologia*, 21:99–105, 1985.

- [Poh01] Pohl, R. et al. Towards a Measurement of the Lamb Shift in Muonic Hydrogen, 2001. Published in [Kar01].
- [Pra74] Pradel, P. et al. Formation of $H(n = 2)$ atoms by the nearly resonant process H^+ in Cs . Multiple collision processes. *Physical Review A*, 10(3):797–812, 1974.
- [Qui01] Quint, W. et al. HITRAP: A Facility for Experiments with Trapped Highly Charged Ions. *Hyperfine Interactions*, 132:457–461, 2001.
- [Rab52] Rabi, I. I. Atomic Beam Resonance Method for Excited States. *Physical Review*, 87:379, 1952.
- [Ram93] Ramsey, N. Experiments with trapped hydrogen atoms and neutrons. *Hyperfine Interactions*, 81(1-4):97–103, 1993.
- [Rei56] Reich, H. A. et al. Hyperfine Structure of the Metastable Deuterium Atom. *Physical Review*, 104(6):1585–1592, 1956.
- [Rot00] Rothery, N. E., Hessels, E. A. Measurement of the 2S atomic hydrogen hyperfine interval. *Physical Review A*, 61:044501, 2000.
- [Sap90] Sapirstein, J. R., Yenni, D. R., 1990. Published in [Kin90] on p.560.
- [Sch99] Schwob, L. et al. Optical Frequency Measurement of the 2S-12D Transitions in Hydrogen and Deuterium: Rydberg Constant and Lamb Shift Determinations. *Physical Review Letters*, 82(25):4960–4963, 1999.
- [Sha91] Shabaev, V. M. Generalizations of the virial relations for the Dirac equation in a central field and their applications to the Coulomb field. *Journal of Physics B*, 24:4479–4488, 1991.
- [Sha94] Shabaev, V. M. Hyperfine structure of hydrogen-like ions. *Journal of Physics B*, 27:5825–5832, 1994.
- [Sha01] Shabaev, V. M. QED theory of the nuclear recoil effect on the atomic g factor. *Physical Review A*, 64:052104, 2001.
- [Sha02] Shabaev, V. M., Yerokhin, V. A. Recoil Correction to the Bound-Electron g Factor in H-Like Atoms to All Orders in αZ . *Physical Review Letters*, 88(9):091801, 2002.
- [Sim80] Simon, G. G., Schmitt, C., Borkowski, F., Walther, V. H. Absolute electron-proton cross sections at low momentum transfer measured with a high pressure gas target system. *Nuclear Physics A*, 333(3):381–391, 1980.

- [Van87] Van Dyck, Jr., R. S., Schwinger, P. B., Dehmelt, H. G. New high-precision comparison of electron and positron g factors. *Physical Review Letters*, 59(1):26–29, 1987.
- [Wer01] Werth, G., Häffner, H., Hermanspahn, N., Kluge, H. -J., Quint, W., Verdú, J. The g Factor of Hydrogenic Ions: A Test of Bound State QED, 2001. Published in [Kar01].
- [Win72] Wineland, D. J., Ramsey, N. F. Atomic Deuterium Maser. *Physical Review A*, 5(2):821–837, 1972.
- [Yer02] Yerokhin, V. A., Indelicato, P., Shabaev, V. M. Self-Energy Correction to the Bound-electron g Factor in H-like Ions. *Physical Review Letters*, 89(14):143001, 2002.

Acknowledgment

At the end of my thesis I would like to address a few words of thank in my native language German.

Abschließend möchte ich meiner gesamten Arbeitsgruppe und allen anderen Beteiligten an dieser Diplomarbeit danken, ohne deren geschlossene Hilfe diese Arbeit nicht möglich gewesen wäre. Es erübrigt sich zu erwähnen, dass besonders in der Experimentalphysik keinerlei Erfolge möglich sind, ohne auf die Hilfe einer funktionierenden Arbeitsgruppe zurückgreifen zu können, so dass die folgende Danksagung keinesfalls nur eine Floskel ist, sondern meinen aufrichtigen Dank ausdrücken soll. Rückblickend war meine Diplomarbeit ein Jahr gefüllt mit neuen Erfahrungen, dem Knüpfen von neuen Kontakten und der Mitarbeit in einem wissenschaftlich hochmotivierten und professionellen Umfeld.

Mein spezieller Dank gilt ganz besonders folgenden Personen:

Ihnen, *Herr Professor Ströher*, gilt mein ganz besonderer Dank. Zum einen dafür, dass Sie mich mit einem hochinteressanten und ebenso hochaktuellen Diplomarbeitsthema betraut haben. Zum anderen, dass Sie mich in meiner gesamten Zeit in Jülich stets in meiner Arbeit unterstützt haben und mit Ihrem stetigen Interesse am Fortschritt des Experiments immer wieder aufs neue motivieren konnten. Aber auch für das mir entgegengebrachte Vertrauen, welches mir die wissenschaftliche Freiheit gegeben hat, um diese Arbeit erst durchzuführen. Dabei habe ich besonders Ihre Toleranz gegenüber interdisziplinärer Arbeit zu schätzen gelernt. Diese hat mir ermöglicht an atomphysikalischen Fragestellungen zu arbeiten, sowohl theoretisch als auch experimentell, in einem Institut für Kernphysik dessen Hauptforschungsgebiete in der Hadronenphysik liegen und das auch noch an einem in dieser Diplomarbeit modifizierten Gerät, welches eigentlich für Polarisationsmessungen des polarisierten Gas-Targets an ANKE eingesetzt wird. Wenn dies keine interdisziplinäre Arbeit gewesen ist, dann weiß ich es wirklich nicht! Vielen Dank!

Mein nächster Dank gilt *Dr. Ralf Engels*, meinem direkten Betreuer dieser Diplomarbeit. Dir, Ralf, möchte ich in erster Linie dafür danken, dass Du dich wirklich jeden Tag für meine Arbeit eingesetzt hast. Sei es durch die tägliche Beantwortung meiner vielen Fragen oder aber durch Deinen direkten Einsatz am und um unser Experiment. Ohne Dich hätte ich das Lambshift-Polarimeter niemals so gut beherrschen können, wie es für die Messungen nötig gewesen ist. Die Zusammenarbeit mit Dir hat mir sehr großen Spaß gemacht. Vielen Dank für alles!

Dr. Kirill Grigoryev möchte ich für seine konstante Hilfsbereitschaft und das stetige

Interesse, das gesamte Experiment betreffend, danken. Sowohl in der Aufbauphase, als auch während der Messung und bei allen weiteren Hürden, die ich über die gesamte Dauer meiner Diplomarbeit am Experiment zu meistern hatte. Ein neues Experiment bringt so einige „Kinderkrankheiten“ mit sich und die daraus resultierende Arbeit ist nur in den seltensten Fällen alleine zu bewältigen. Bedanken möchte ich mich auch für die Datenauslese, ohne die meine Messung nicht möglich gewesen wäre und für das stetige Interesse die Software auf meine Wünsche anzupassen.

Ebenso möchte ich *Dr. Maxim Mikirtychiants* danken, der mir in allen technischen Problemen während des Aufbaus des Experiments mit Rat und Tat zur Seite gestanden hat und für die erstklassigen CAD-Zeichnungen, mit denen die Werkstätten die benötigten Bauteile schnellstmöglich für uns fertigen konnten. Ganz besonders bedanken möchte ich mich für das Design der TEM-Hochfrequenzzelle, die sich im Experiment bei ihrem erstmaligen Einsatz schon bewährt hat.

Dipl.-Ing. Gephard Schug möchte ich für die Einführung in die Mysterien der Hochfrequenztechnik danken, insbesondere für die Berechnung der 1.4 GHz TEM-Zelle. Besonderer Dank gilt Dir aber als ständiger Ansprechpartner, selbst nachts, wenn die Hochfrequenz während der Messungen wieder eine neue Überraschung aus dem Hut zauberte.

Dipl.-Ing. Janos Sarkadi danke ich, auch stellvertretend für die gesamte Elektronikwerkstatt des Instituts für Kernphysik, für die schnelle Hilfe bei diversen Reparaturen von Netzgeräten, Steckern, Kabeln und bei allen weiteren kleineren Anliegen, die für das weitere Vorankommen am Experiment sehr wichtig waren.

Dipl.-Ing. Franz Klehr und dem ZAT möchte ich ebenfalls für eine erstklassige Zusammenarbeit danken. Zum einen bei der Fertigung der TEM-Hochfrequenzzelle, aber auch bei der Fertigung der Spulenkörper, der Spulenhalterungen und schließlich für die lasergeschnittenen hochpräzisen Kupfergitter.

Der *Feinmechanikwerkstatt* sei an dieser Stelle ebenfalls herzlichst gedankt. Insbesondere für die Fertigung der Kupferrahmen für die TEM-Hochfrequenzzelle kurz vor Weihnachten, in die wir dann noch vor den Feiertagen die Kupfergitter einlassen konnten, um so bessere Hochfrequenzbedingungen zu schaffen.

Dann möchte ich natürlich noch dem harten Kern unserer täglichen Mittagessen-Runde, gebildet von *Ralf Engels, Detlev Gotta, Alexander Nass, Hellmut Seyfarth, Joachim Stein* und meiner Wenigkeit für die immer gute Atmosphäre danken. Ebenso für die immer freundliche Atmosphäre in der PIT-Gruppe und für eine nette „Büronachbarschaft“.

Ich danke *Prof. Dr. Paetz gen. Schieck*, *Ralf Engels*, *Kirill Grigoryev*, *Maxim Mikirtychiants*, *Alexander Nass* und *Hellmut Seyfarth* für die kritische Durchsicht meiner Diplomarbeit sowie *Prof. Dr. Stutzki* von der Universität zu Köln für die Übernahme des Zweitgutachtens.

Des Weiteren danke ich *Prof. Dr. Paetz gen. Schieck* für die einmalige Möglichkeit, dass ich schon in einer frühen Phase meines Studiums erste Eindrücke des echten Forschungsalltags sammeln durfte. Im Rahmen der „Miniforschung“ im Institut für Kernphysik der Universität zu Köln hatte ich dadurch die Möglichkeit innerhalb einer Doktorarbeit (*Reinhard Emmerich*) zum ersten Mal ein Lambshift-Polarimeter zu benutzen. Weiterhin hatte ich die Möglichkeit wichtige Anwendungen der Atom- und Spinphysik mitzuerleben. Ich danke *Herrn Schieck* und *Herrn Emmerich* für die tägliche und geduldige Betreuung in dieser Zeit.

Weiterhin möchte ich mich bei folgenden auswärtigen Personen bedanken:

Besonders in der Anfangsphase meiner Diplomarbeit stellte sich die Frage nach den aktuellsten Breit-Rabi-Formeln für Wasserstoff und Deuterium. Die in Büchern allseits bekannte Formel erweist sich bei näherer Betrachtung zwar als eine gute Näherung, jedoch kennt die theoretische Physik heutzutage Methoden, um genaue Berechnungen im Rahmen der Quantenelektrodynamik anzustellen.

Ich möchte mich bei der Gruppe von *Prof. Dr. Vladimir M. Shabaev* vom Institut für Quantenmechanik der staatlichen Universität St. Petersburg bedanken, insbesondere bei *Dmitriy L. Moskovkin* und bei *Dmitry A. Glazov*. Innerhalb weniger Monate wurden von dieser Gruppe für uns die momentan aktuellsten Breit-Rabi-Diagramme für den $2S_{1/2}$ und $2P_{1/2}$ Zustand in Wasserstoff und Deuterium berechnet.

Ebenso möchte ich mich bei *PD. Dr. Ulrich Jentschura* vom Institut für theoretische Physik des Max-Planck-Instituts für Kernphysik in Heidelberg für die Bereitschaft bedanken, sich zwischen einem ganzen Haufen von Arbeit, auch für mich über eine neue Berechnung der klassischen Lambshift Gedanken zu machen.

Zum Schluss möchte ich meinen Eltern dafür danken, dass sie mir das Physikstudium und somit auch diese Arbeit ermöglicht haben.

Erklärung

Ich versichere, dass ich die von mir vorgelegte Diplomarbeit selbständig verfasst und keine anderen als die angegebenen Quellen und Hilfsmittel benutzt, sowie die Stellen der Arbeit, die anderen Werken im Wortlaut oder Sinn nach entnommen sind, in jedem Einzelfall als Entlehnung kenntlich gemacht habe.

Jülich, im Juni 2008

Marc Peter Westig